

**Structure Determination of Membrane Proteins
with Diverse Sizes in Close-to-Native Environments
by Cryo-electron Tomography**

Dissertation

zur Erlangung des Doktorgrades der Naturwissenschaften vorgelegt dem
Fachbereich Biochemie, Chemie und Pharmazie der Johann Wolfgang Goethe-
Universität in Frankfurt am Main

von

Shih-Ying Chang

aus Tainan, Taiwan

Frankfurt am Main (2023)

(D30)

vom Fachbereich 14 Biochemie, Chemie und Pharmazie der Goethe-Universität als
Dissertation angenommen.

Dekan: Prof. Dr. Clemens Glaubitz

Gutachter: Prof. Dr. Alexander Gottschalk

Gutachter: Prof. Dr. Misha Kudryashev

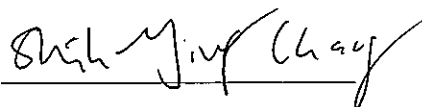
A handwritten signature in blue ink, appearing to be 'Kudryashev', is written over the name of the second reviewer.

Datum der Disputation: 07.03.2024

Diese Dissertation wurde von August 2017 bis Juli 2023 unter Leitung von Prof. Dr. Werner Kühlbrandt und Prof. Dr. Misha Kudryashev in der Abteilung Strukturbiologie am Max-Planck-Institut für Biophysik in Frankfurt am Main durchgeführt.

Eidesstattliche Erklärung

Hiermit versichere ich, dass ich die vorliegende Arbeit selbstständig angefertigt habe und keine anderen, als die angegebenen Hilfsmittel und Quellen verwendet habe.



(Shih-Ying Chang)

Frankfurt am Main, den

Except where stated otherwise by reference or acknowledgment, the work presented in this thesis was generated by myself under the supervision of my advisors during my doctoral studies.

Whenever a figure, table or text is identical to a previous publication, it is stated explicitly in the thesis that copyright permission and/or co-author agreement has been obtained.

The following parts of the thesis are generated by myself and have been previously published:

Chapter 2, Figure 2.3, 2.7, 2.14, 2.15, 2.16, and 2.18;

Chapter 3, Figure 3.6;

Appendix, Figure B.1; Table B.1 and Table C.1;

the above-mentioned contents have been published in

1. Chang, S. S.; Dijkman, P. M.; Wiessing, S. A.; Kudryashev, M., Determining the structure of the bacterial voltage-gated sodium channel NaChBac embedded in liposomes by cryo electron tomography and subtomogram averaging. *Sci Rep* 2023, 13 (1), 11523.
2. Sanchez, C. P.; Patra, P.; Chang, S. S.; Karathanasis, C.; Hanebutte, L.; Kilian, N.; Cyrklaff, M.; Heilemann, M.; Schwarz, U. S.; Kudryashev, M.; Lanzer, M., KAHRP dynamically relocates to remodeled actin junctions and associates with knob spirals in *Plasmodium falciparum*-infected erythrocytes. *Mol Microbiol* 2022, 117 (2), 274-292.

Declaration of collaborative work

Chapter 2, the construct - full-length NaChBac cDNA into pET21a with an N-terminal His₆-GFP^{A206K} fusion protein was cloned by Simon A. Wiessing under the supervision of Dr. Patricia M. Dijkman.

Chapter 3, erythrocyte ghost membrane samples were provided by Dr. Cecilia Sanchez from the group of Prof. Dr. rer. nat. Michael Lanzer at Universitätsklinikum Heidelberg.

Appendix Figure C.1 images were provided by Dr. Cecilia Sanchez from the group of Prof. Dr. rer. nat. Michael Lanzer at Universitätsklinikum Heidelberg.

Summary

Biological membranes serve as physical barriers in cells and organelles, enabling the maintenance of chemical or ionic gradients that are essential for triggering various integral, peripheral, or lipid-anchored membrane proteins, necessary for their life-essential functions. Due to the crucial roles of membrane proteins, they represent potential targets for over 50% of currently available drugs. Understanding the structural characteristics of membrane proteins is essential for elucidating their functional mechanisms and their applications in new drug discovery.

The study of membrane proteins has unique challenges due to their hydrophobic nature, limited expression levels, and inherent flexibility. These characteristics make it difficult to obtain their structure information for comprehensive understanding their functions and mechanisms. Traditional high-resolution techniques like X-ray crystallography and nuclear magnetic resonance (NMR) are less effective in determining the atomic resolution structures of membrane proteins compared to soluble proteins. Currently, cryo-electron microscopy (cryo-EM) have revolutionized the field by providing unprecedented opportunities for studying the structures of membrane proteins and other biological macromolecules. Single-particle analysis (SPA) enables the determination of high-resolution three-dimensional structures using minimal amounts of specimen without the need for crystallization. Additionally, cryogenic electron tomography (cryo-ET) and subtomogram averaging (StA) offer the ability to study membrane protein complexes, cellular architecture, and molecular interactions (or so-called molecular sociology) while preserving close-to-life conditions. With more improvements of cryo-EM technologies, high-resolution structures of membrane proteins *in vitro* can allow people to understand their mechanisms and functions, and to facilitate the design and optimization of new therapeutic agents. Furthermore, there has been significant growth in the structural characterization of membrane proteins *in situ*, as studying biomolecules within their physiological context is an ultimate goal in structural biology for a comprehensive understanding of molecular networks in cells.

Due to the amphipathic nature of membrane proteins, their production, purification, and isolation pose significant challenges compared to soluble proteins. To maintain the membrane protein fold in an aqueous buffer after disrupting lipid membranes, the use of detergents,

amphipols, lipid nanodiscs, saposin-lipoprotein (salipro), styrene-maleic acid co-polymer lipid particles (SMALPS) is common and often essential. For the cryo-EM study of membrane proteins *in vitro*, a drawback of the membrane-mimetic systems is the absence of an actual lipid bilayer environment. Such an environment is essential for the structure, function and stability of membrane proteins. To address this issue, membrane proteins can be reconstituted into liposomes, and this closed membrane environment closely mimics the physiological conditions of the proteins. This approach involves membrane proteins, which can be produced recombinantly or extracted from native membranes. These proteins are then purified using detergent carriers and subsequently reconstituted into liposomes in preparation for cryo-EM studies. The use of liposomes for structure determination is expected to significantly expand in the *in vitro* study of membrane proteins and membrane-associated proteins, particularly for capturing transient complexes in specific functional states. This advancement promises to provide more detailed insights into molecular mechanisms and enhance our understanding of these proteins.

Resolving the structures of membrane proteins in their native cellular context is considered the ideal approach for understanding their functions and associated molecular networks. While single-particle cryo-EM can achieve higher resolution than subtomogram averaging, it often requires at least partial purification of the target molecules from their native environment inside cells and tissues. By combining averaging tools on subvolumes obtained through cryo-ET, structures can currently be determined at resolutions of 10-30 Å. These maps can then be fitted with high-resolution structures obtained using other techniques, such as SPA, to create detailed models of structures and complexes as they occur in cells. In spite of remaining some challenges in the current cryo-ET workflow, like low throughput in sample preparation, slow data acquisition speeds, difficulties in target identification, and limited usability of image processing software, several proof-of-concept strategies have emerged to address these issues. With ongoing advancements and refinements in cryo-ET methodologies, routine high-resolution structure determination *in situ* is poised to become a valuable tool for both structural and cell biologists in the long run, and the field holds great promise for further expanding our understanding of cellular structures and processes at the molecular level.

The main aim of this thesis is to further our knowledge about the structure and function of membrane protein in lipid bilayer vesicles and membrane-associated protein complexes in their native environment. The research focuses on two specific targets: a small prokaryotic voltage-

gated sodium ion channel, NaChBac, and a large knob complex found on the surface of *Plasmodium falciparum*-infected human erythrocyte.

In neuronal signaling and muscular contraction, Na⁺ influx through voltage-gated sodium channels (VGSCs) corresponds to the rapid rising phase of the action potential in the membranes of neurons and other electrically excitable cells. VGSCs undergo a series of conformational changes between open, closed, and inactivated states during a cycle of an action potential. Each action potential is followed by a refractory period, during which the VGSCs enter an inactivated state while the Na⁺ and K⁺ ions return to their resting state distributions across the membrane, yielding a resting membrane potential of approximately -70 mV in most neurons. Under the resting potential, VGSCs transition back to their resting state in which they remain until the next action potential. To date, structures of VGSCs have been determined in crystals, detergent micelles, or nanodiscs. Various approaches, such as chemical cross-linking, mutations, and toxins have been employed to stabilize voltage sensors in conformations that mimic the resting state of VGSCs in cells. The concern remains that the changes observed may not accurately represent the behavior of the channels in their native membrane, as they lack a voltage difference across membranes. Studying NaChBac gating mechanisms in a membrane environment is therefore of great interest. Chapter 2 aims to obtain structural and dynamic information on NaChBac in liposomes, and on how the channel is influenced by a physiological resting membrane potential. However, NaChBac is a small (~120 kDa) membrane protein without a significantly large soluble domain, making it challenging to accurately identify fully transmembrane proteins in electron micrographs for alignment and averaging. With recent advancements in cryo-ET and StA, the techniques might be able to target smaller membrane proteins in proteoliposomes, as tomograms contain the third dimension compared to 2D imaging in single particle cryo-EM. To this end, the experimental process involves the purification of NaChBac, reconstitution of the protein into liposomes, establishment of a transmembrane potential in the proteoliposomes, optimization of cryo-grid preparation, processing of cryo-ET data, and structural analysis by StA.

The results of this study demonstrate the feasibility of identifying and aligning small, mostly transmembrane proteins like NaChBac embedded in liposomes using StA and obtaining a correct structure, albeit at a modest resolution compared to the limits of single-particle analysis processing. Here, fused GFP was used to locate the proteins of interest in tomograms and perform a rough alignment. However, for the final steps of the alignment, GFP was not useful

due to the flexibility of the linker region. The tetrameric NaChBac with a molecular weight of ~120 kDa and mostly transmembrane residues is on the smaller side of the molecular weight range that could be approached using current technology. For the structure determination, the channels were imaged in thin ice, a large number of particles were picked, and a combination of classification algorithms (Dynamo and RELION-4.0) was used. Even with such optimizations, the achieved resolution was only ~16 Å. At this domain-level resolution, the pore and voltage-sensing domains of the channel could be reliably observed. It was estimated that the structure of the channel in proteoliposomes is ~10% wider than the structure reported in nanodiscs (EMD-21425) filtered to the same resolution, while the increased size of the channel may not be solely due to the applied potential but rather a consequence of imaging the channel in a lipid bilayer without physical restraints. The approach presented in this study, which can be widely applied to cryo-EM analysis of membrane proteins, with a specific focus on membrane proteins with small soluble domains, lays the foundation for cryo-ET and StA of integral or peripheral membrane proteins whose functions are affected by transmembrane electrochemical gradients and/or membrane curvatures.

Malaria remains a major and growing threat to public health and economic development of countries in the tropical and subtropical regions of the world to date. *Plasmodium falciparum*, the human malaria parasite, infects red blood cells (RBCs) and induces the formation of numerous small membrane protrusions that render their initially smooth surface bumpy. These changes on the surface of RBCs result in sequestration of parasitized erythrocytes in the microvasculature and lead to severe disease. For each protrusion, termed as a knob, is a major pathophysiological determinant in *P. falciparum* infections. While a previous study provided an overall architectural view of knobs using negative stain tomography, there is a need for a higher-resolution cryo-EM structure *in situ* to investigate the structure of the knob complex at different stages of parasite development and to explore its association with the erythrocyte membrane skeleton. Chapter 3 attempts to bridge this gap by imaging knob complex in *P. falciparum*-infected human erythrocytes, and the structure determination of the knob complex by StA can offer structural insights, guiding future work to uncover the molecular composition and the role of these native knobs in *Plasmodium* infection and immunity.

This research has, for the first time, revealed the structure of the knob complex at 31.3 Å resolution in parasitized erythrocyte membrane ghosts using cryo-ET and StA. It showed the presence of stick-like densities that seem to anchor the knob spiral to the lipid bilayer.

Moreover, this study has uncovered additional features, including the intra-spiral densities between the second and third turn, which might stabilize the spiral. Crown-like extra densities were observed at the periphery of the spiral base, which might be involved in connecting the spiral with filamentous structures. The results further showed a high degree of variability between spirals with regard to the number of turns and the number of peripheral proteins, possibly reflecting different stages and/or functions of knob configuration. The structure of the knob complex obtained in this research provides a model to understand the organization of the core knob components and may reveal novel proteins as knob components in future studies, and possibly, it might reflect the processes involved in the parasite-induced reorganization and disassembly of the spectrin/actin network in human RBCs at the molecular level. The knowledge gained in this study can be used in the development of improved vaccine design strategies or drug design approaches to destabilize the knob complex, which is a major virulence determinant in *P. falciparum* infections.

This work presents the first StA map of the 120-kDa NaChBac embedded in liposomes under a resting membrane potential, and the first cryo-EM structure of the supramolecular knob complex in *P. falciparum*-infected human erythrocyte. This thesis opens up several promising lines for future studies of membrane proteins *in vitro* and *in situ*, where other membrane proteins can be studied in physiologically relevant environments. Already with the present generation of cryo-EM hardware and software, this thesis represents pioneering research in the field of membrane protein structural biology.

Ausführliche deutschsprachige Zusammenfassung

Biologische Membranen dienen als physische Barrieren in Zellen und Organellen und ermöglichen die Aufrechterhaltung chemischer oder ionischer Gradienten, die für das Auslösen verschiedener integraler, peripherer oder lipidverankerter Membranproteine notwendig sind, die für ihre lebenswichtigen Funktionen erforderlich sind. Aufgrund der wichtigen Rollen von Membranproteinen stellen sie potenzielle Angriffspunkte für über 50% der derzeit verfügbaren Medikamente dar. Das Verständnis der strukturellen Merkmale von Membranproteinen ist entscheidend, um ihre funktionellen Mechanismen zu klären und ihre Anwendungen in der Entdeckung neuer Arzneimittel zu nutzen.

Die Untersuchung von Membranproteinen steht aufgrund ihrer hydrophoben Natur, begrenzter Expressionsebenen und inhärenten Flexibilität vor einzigartigen Herausforderungen. Diese Merkmale machen es schwierig, ihre Strukturinformationen zur umfassenden Verständnis ihrer Funktionen und Mechanismen zu erhalten. Traditionelle hochauflösende Techniken wie Röntgenkristallographie und Kernresonanz (NMR) sind weniger effektiv bei der Bestimmung der atomaren Auflösungsstrukturen von Membranproteinen im Vergleich zu löslichen Proteinen. Derzeit haben Kryo-Elektronenmikroskopie (Kryo-EM) das Feld revolutioniert, indem sie beispiellose Möglichkeiten zur Untersuchung von Membranproteinen und anderen biologischen Makromolekülen bieten. Die Einzelpartikelanalyse (SPA) ermöglicht die Bestimmung hochauflösender dreidimensionaler Strukturen unter Verwendung minimaler Probenmengen, ohne dass eine Kristallisation erforderlich ist. Darüber hinaus bieten kryogene Elektronentomographie (Cryo-ET) und Subtomogramm-Durchschnitt (StA) die Möglichkeit, Membranprotein-Komplexe, zelluläre Architektur und molekulare Interaktionen (oder sogenannte molekulare Soziologie) zu untersuchen, während lebensnahe Bedingungen erhalten bleiben. Mit weiteren Verbesserungen der Kryo-EM-Technologien können hochauflösende Strukturen von Membranproteinen *in vitro* ermöglichen, dass Menschen ihre Mechanismen und Funktionen verstehen und die Gestaltung und Optimierung neuer therapeutischer Wirkstoffe erleichtern. Darüber hinaus hat es signifikantes Wachstum in der strukturellen Charakterisierung von Membranproteinen *in situ* gegeben, da die Untersuchung von Biomolekülen in ihrem physiologischen Kontext ein ultimatives Ziel in der Strukturbiologie für ein umfassendes Verständnis molekularer Netzwerke in Zellen ist.

Aufgrund der amphiphatischen Natur von Membranproteinen stellen ihre Herstellung, Reinigung und Isolierung im Vergleich zu löslichen Proteinen erhebliche Herausforderungen dar. Um die Membranproteinfaltung in einem wässrigen Puffer nach der Unterbrechung von Lipidmembranen aufrechtzuerhalten, ist die Verwendung von Detergenzien, Amphipolen, Lipidnanoscheiben, Saposin-Lipoprotein (Salipro) und Styrol-Maleinsäure-Copolymer-Lipidpartikeln (SMALPS) üblich und oft unerlässlich. Für die Kryo-EM-Untersuchung von Membranproteinen *in vitro* ist ein Nachteil der membrandominierten Systeme das Fehlen einer tatsächlichen Lipiddoppelschichtumgebung. Eine solche Umgebung ist für die Struktur, Funktion und Stabilität von Membranproteinen wesentlich. Um dieses Problem zu lösen, können Membranproteine in Liposomen rekonstituiert werden, und diese geschlossene Membranumgebung ahmt eng die physiologischen Bedingungen der Proteine nach. Dieser Ansatz beinhaltet Membranproteine, die rekombinant hergestellt oder aus nativen Membranen extrahiert werden können. Diese Proteine werden dann mit Hilfe von Detergens-Trägern gereinigt und anschließend in Liposomen rekonstituiert, um sie für Kryo-EM-Studien vorzubereiten. Die Verwendung von Liposomen zur Strukturbestimmung wird voraussichtlich die *in vitro*-Untersuchung von Membranproteinen und membrangebundenen Proteinen erheblich erweitern, insbesondere um transiente Komplexe in spezifischen funktionellen Zuständen einzufangen. Dieser Fortschritt verspricht detailliertere Einblicke in molekulare Mechanismen und verbessert unser Verständnis dieser Proteine.

Die Auflösung der Strukturen von Membranproteinen in ihrem nativen zellulären Kontext gilt als der ideale Ansatz, um ihre Funktionen und die zugehörigen molekularen Netzwerke zu verstehen. Obwohl die Einzelpartikel-Kryo-EM eine höhere Auflösung als die Subtomogramm-Durchschnitt erreichen kann, erfordert sie oft zumindest eine teilweise Reinigung der Zielmoleküle aus ihrer nativen Umgebung innerhalb von Zellen und Geweben. Durch die Kombination von Durchschnittswerkzeugen auf Untervolumina, die durch Cryo-ET erhalten wurden, können Strukturen derzeit mit Auflösungen von 10-30 Å bestimmt werden. Diese Karten können dann mit hochauflösenden Strukturen, die mit anderen Techniken wie SPA erhalten wurden, angepasst werden, um detaillierte Modelle von Strukturen und Komplexen zu erstellen, wie sie in Zellen auftreten. Trotz einiger Herausforderungen im aktuellen Cryo-ET-Arbeitsablauf, wie niedrige Durchsatzraten bei der Probenvorbereitung, langsame Datenakquisitionsgeschwindigkeiten, Schwierigkeiten bei der Zielerkennung und begrenzte Verwendbarkeit von Bildverarbeitungssoftware, sind mehrere Konzeptnachweise entwickelt worden, um diese Probleme anzugehen. Mit laufenden Fortschritten und

Verfeinerungen in den Cryo-ET-Methoden wird die routinemäßige hochauflösende Strukturbestimmung *in situ* langfristig ein wertvolles Werkzeug für Struktur- und Zellbiologen werden, und das Feld birgt großes Potenzial, unser Verständnis zellulärer Strukturen und Prozesse auf molekularer Ebene weiter auszudehnen.

Das Hauptziel dieser Arbeit ist es, unser Wissen über die Struktur und Funktion von Membranproteinen in Liposomen und membrangebundenen Protein-Komplexen in ihrer nativen Umgebung weiter auszubauen. Die Forschung konzentriert sich auf zwei spezifische Ziele: einen kleinen prokaryotischen spannungsgesteuerten Natriumionenkanal, NaChBac, und einen großen Knopfkomplex, der auf der Oberfläche von mit *Plasmodium falciparum*-infizierten menschlichen Erythrozyten gefunden wird.

Bei der neuronalen Signalgebung und der muskulären Kontraktion entspricht der Na^+ -Einfluss durch spannungsgesteuerte Natriumkanäle (VGSCs) der schnellen Aufwärtsphase des Aktionspotentials in den Membranen von Neuronen und anderen elektrisch erregbaren Zellen. VGSCs durchlaufen eine Serie von Konformationsänderungen zwischen offenen, geschlossenen und inaktivierten Zuständen während eines Zyklus eines Aktionspotentials. Auf jedes Aktionspotential folgt eine refraktäre Periode, während der die VGSCs in einen inaktivierten Zustand eintreten, während die Na^+ - und K^+ -Ionen in ihre Ruheverteilungen über die Membran zurückkehren und ein Ruhepotential von etwa -70 mV in den meisten Neuronen erzeugen. Unter dem Ruhepotential wechseln VGSCs in ihren Ruhezustand zurück, in dem sie bis zum nächsten Aktionspotential verbleiben. Bis heute wurden Strukturen von VGSCs in Kristallen, Detergenzmizellen oder Nanoscheiben bestimmt. Verschiedene Ansätze wie chemische Quervernetzung, Mutationen und Toxine wurden eingesetzt, um Spannungssensoren in Konformationen zu stabilisieren, die den Ruhezustand von VGSCs in Zellen nachahmen. Die Bedenken bleiben, dass die beobachteten Veränderungen das Verhalten der Kanäle in ihrer nativen Membran möglicherweise nicht genau widerspiegeln, da ihnen ein Spannungsunterschied über die Membran fehlt. Die Untersuchung der Mechanismen der NaChBac-Gating in einer Membrenumgebung ist daher von großem Interesse. Kapitel 2 zielt darauf ab, strukturelle und dynamische Informationen über NaChBac in Liposomen zu erhalten und wie der Kanal durch ein physiologisches Ruhepotential beeinflusst wird. Allerdings ist NaChBac ein kleines (~120 kDa) Membranprotein ohne einen signifikant großen löslichen Bereich, was es schwierig macht, vollständig transmembrane Proteine in Elektronenmikroskopaufnahmen für die Ausrichtung und den Durchschnitt genau zu

identifizieren. Mit den jüngsten Fortschritten in Cryo-ET und StA könnten die Techniken in der Lage sein, kleinere Membranproteine in Proteoliposomen anzuzielen, da Tomogramme die dritte Dimension im Vergleich zur 2D-Bildgebung in der Einzelpartikel-Kryo-EM enthalten. Zu diesem Zweck umfasst der experimentelle Prozess die Reinigung von NaChBac, die Rekonstitution des Proteins in Liposomen, die Herstellung eines transmembranen Potentials in den Proteoliposomen, die Optimierung der Kryo-Gittervorbereitung, die Verarbeitung der Cryo-ET-Daten und die strukturelle Analyse durch StA.

Die Ergebnisse dieser Studie zeigen die Machbarkeit, kleine, hauptsächlich transmembrane Proteine wie NaChBac, die in Liposomen eingebettet sind, mittels StA zu identifizieren und auszurichten und eine korrekte Struktur zu erhalten, wenn auch in bescheidener Auflösung im Vergleich zu den Grenzen der Einzelpartikelanalyse-Verarbeitung. Hier wurde das fusionierte GFP verwendet, um die Proteine von Interesse in den Tomogrammen zu lokalisieren und eine grobe Ausrichtung durchzuführen. Für die letzten Schritte der Ausrichtung war GFP jedoch aufgrund der Flexibilität des Verbindungsstücks nicht nützlich. Das tetramere NaChBac mit einem Molekulargewicht von ~120 kDa und hauptsächlich transmembranen Aminosäureresten liegt auf der kleineren Seite des Bereichs des Molekulargewichts, das mit derzeitiger Technologie erreicht werden kann. Für die Strukturbestimmung wurden die Kanäle im dünnen Eis abgebildet, eine große Anzahl von Partikeln wurde ausgewählt und eine Kombination von Klassifikationsalgorithmen (Dynamo und RELION-4.0) wurde verwendet. Selbst mit solchen Optimierungen betrug die erzielte Auflösung nur ~16 Å. Bei dieser domänenniveau-Auflösung konnten die Poren- und Spannungssensordomänen des Kanals zuverlässig beobachtet werden. Es wurde geschätzt, dass die Struktur des Kanals in Proteoliposomen ~10% breiter ist als die Struktur, die in Nanoscheiben (EMD-21425) mit derselben Auflösung gefiltert wurde, während die erhöhte Größe des Kanals nicht ausschließlich auf das angelegte Potential zurückzuführen ist, sondern vielmehr eine Folge davon ist, dass der Kanal in einer Lipiddoppelschicht ohne physische Einschränkungen abgebildet wird. Der in dieser Studie vorgestellte Ansatz, der auf die Kryo-EM-Analyse von Membranproteinen angewendet werden kann, mit einem speziellen Fokus auf Membranproteinen mit kleinen löslichen Domänen, legt den Grundstein für Cryo-ET und StA von integralen oder peripheren Membranproteinen, deren Funktionen von transmembranen elektrochemischen Gradienten und/oder Membrankrümmungen beeinflusst werden.

Malaria bleibt bis heute eine große und wachsende Bedrohung für die öffentliche Gesundheit und wirtschaftliche Entwicklung von Ländern in den tropischen und subtropischen Regionen der Welt. *Plasmodium falciparum*, der menschliche Malariaerreger, infiziert rote Blutkörperchen (RBCs) und führt zur Bildung zahlreicher kleiner Membranvorsprünge, die ihre ursprünglich glatte Oberfläche uneben machen. Diese Veränderungen an der Oberfläche der RBCs führen zur Sequestrierung parasitierter Erythrozyten im Mikrovaskulatur und führen zu schweren Erkrankungen. Für jede Vorsprung, die als Knopf bezeichnet wird, handelt es sich um einen wichtigen pathophysiologischen Bestimmungsfaktor bei *P. falciparum*-Infektionen. Während eine frühere Studie einen allgemeinen architektonischen Blick auf Knöpfe mittels Negativfärbe-Tomographie lieferte, besteht Bedarf an einer hochauflösenden Kryo-EM-Struktur *in situ*, um die Struktur des Knopfkomplexes in verschiedenen Stadien der Parasitenentwicklung zu untersuchen und seine Assoziation mit dem Erythrozytenmembranskelett zu erforschen. Kapitel 3 versucht, diese Lücke zu schließen, indem der Knopfkomplex in mit *Plasmodium falciparum*-infizierten menschlichen Erythrozyten abgebildet wird, und die Strukturbestimmung des Knopfkomplexes durch StA kann strukturelle Einblicke bieten und zukünftige Arbeiten zur Aufdeckung der molekularen Zusammensetzung und der Rolle dieser nativen Knöpfe bei der Plasmodium-Infektion und Immunität lenken.

Diese Forschung hat erstmals die Struktur des Knopfkomplexes mit einer Auflösung von 31,3 Å in membrangeistereten Erythrozytenmembranen mittels Cryo-ET und StA aufgezeigt. Sie zeigte die Anwesenheit von stockartigen Dichten, die den Knopfspiral an die Lipiddoppelschicht zu verankern scheinen. Darüber hinaus hat diese Studie zusätzliche Merkmale aufgedeckt, darunter die intra-spiralen Dichten zwischen der zweiten und dritten Wendung, die die Spirale stabilisieren könnten. Kronenartige zusätzliche Dichten wurden am Rand der Spiralspitze beobachtet, die möglicherweise an der Verbindung der Spirale mit filamentösen Strukturen beteiligt sind. Die Ergebnisse zeigten zudem eine hohe Variabilität zwischen Spiralen hinsichtlich der Anzahl der Wendungen und der Anzahl der peripheren Proteine, was möglicherweise verschiedene Stadien und/oder Funktionen der Knopfkonfiguration widerspiegelt. Die in dieser Forschung gewonnene Struktur des Knopfkomplexes liefert ein Modell, um die Organisation der Kernknopfkomponenten zu verstehen, und könnte in zukünftigen Studien möglicherweise neuartige Proteine als Knopfkomponenten aufdecken, und möglicherweise könnte sie die Prozesse reflektieren, die an der parasiteninduzierten Reorganisation und Auflösung des Spektrin/Aktin-Netzwerks in

menschlichen RBCs auf molekularer Ebene beteiligt sind. Das in dieser Studie gewonnene Wissen kann in der Entwicklung von verbesserten Impfstrategien oder Arzneimitteldesignansätzen verwendet werden, um den Knopfkomplex zu destabilisieren, der ein wichtiger Virulenzbestimmungsfaktor bei *P. falciparum*-Infektionen ist.

Diese Arbeit präsentiert die erste StA-Karte des 120-kDa-NaChBac, der in Liposomen eingebettet ist, unter einem Ruhepotential der Membran, und die erste Kryo-EM-Struktur des supramolekularen Knopfkomplexes in *P. falciparum*-infizierten menschlichen Erythrozyten. Diese Arbeit eröffnet mehrere vielversprechende Ansätze für zukünftige Studien von Membranproteinen *in vitro* und *in situ*, bei denen andere Membranproteine in physiologisch relevanten Umgebungen untersucht werden können. Bereits mit der aktuellen Generation von Cryo-EM-Hardware und -Software stellt diese Arbeit bahnbrechende Forschung im Bereich der strukturellen Biologie von Membranproteinen dar.

Contents

Summary	i
Ausführliche deutschsprachige Zusammenfassung	vi
List of publications	xv
List of figures	xvi
List of tables	xviii
Abbreviations	xviii
Chapter 1 Introduction	1
1.1 Membrane proteins	1
1.2 From TEM to Cryo-EM	2
1.2.1 Single-particle cryo-electron microscopy	5
1.2.2 Cryo-electron tomography (Cryo-ET) and subtomogram averaging (StA)	11
1.3 Cryo-EM study of membrane proteins in structural biology	15
1.3.1 Membrane protein structures <i>in vitro</i>	18
1.3.2 Membrane protein structures <i>in situ</i>	21
1.4 Aims of the thesis	23
Chapter 2 Determining the structure of the bacterial voltage-gated sodium channel NaChBac embedded in liposomes by cryo-ET and StA	25
2.1 Introduction	25
2.1.1 Conformational cycle of a voltage-gated sodium channel (VGSC)	25
2.1.2 Membrane potential measurements in proteoliposomes using fluorescent indicators	27
2.1.3 Membrane protein structures embedded in liposomes	28
2.1.4 Aim	29
2.2 Materials and methods	30
2.2.1 Materials, instrumentation, and programs	30
2.2.1.1 Materials	30
2.2.1.2 Instrumentation	31
2.2.1.3 Programs	32
2.2.2 Methods	33
2.2.2.1 Expression and purification of NaChBac	33
2.2.2.2 NaChBac reconstitution into liposomes	33

2.2.2.3 Density gradient centrifugation.....	34
2.2.2.4 Negative-staining EM	34
2.2.2.5 Proteoliposome flux assay.....	34
2.2.2.6 Preparation of proteoliposomes with polarized membranes for cryo-EM	35
2.2.2.7 Single-particle data acquisition and data processing.....	35
2.2.2.8 Cryo-ET data collection, image processing, and subtomogram averaging.....	36
2.3 Results	37
2.3.1 Sample preparation.....	37
2.3.1.1 Protein expression and purification.....	37
2.3.1.2 Proteoliposome reconstitution.....	38
2.3.1.3 Preparation of proteoliposomes with polarized membranes	40
2.3.1.4 Cryo-EM grid preparation.....	42
2.3.2 Single-particle cryo-EM of NaChBac proteoliposomes.....	43
2.3.3 Cryo-ET of NaChBac proteoliposomes	46
2.3.4 Subtomogram averaging of NaChBac proteoliposomes	48
2.3.5 Structural analysis of NaChBac in liposomes	53
2.4 Summary and discussion.....	55
Chapter 3 Molecular architecture of the knob complex in <i>Plasmodium falciparum</i>-infected human erythrocytes by cryo-ET and StA.....	57
3.1 Introduction	57
3.1.1 Malaria and the parasite <i>Plasmodium falciparum</i>	57
3.1.2 Knob complex and its interactions with the erythrocyte membrane skeleton during <i>P. falciparum</i> infection	60
3.1.3 Aim.....	62
3.2 Materials and methods	63
3.2.1 Materials, instrumentation, and programs.....	63
3.2.1.1 Materials.....	63
3.2.1.2 Instrumentation.....	63
3.2.1.3 Programs.....	63
3.2.2 Methods.....	64
3.2.2.1 Parasite culture and erythrocyte ghost membrane preparation	64
3.2.2.2 Sample preparation, cryo-ET, and image processing of <i>P. falciparum</i> -infected human erythrocytes	64
3.2.2.3 StA of knobs.....	65

3.3 Results	66
3.3.1 Cryo-ET of <i>P. falciparum</i> -infected human erythrocytes <i>in situ</i>	66
3.3.2 StA of knob spirals.....	68
3.3.3 3D structure of the knob complex	70
3.4 Summary and discussion.....	72
Chapter 4 Conclusions and future perspective.....	74
Appendix	79
A. Detailed overview of the experimental conditions.....	79
A.1 Protein sequence (full-length <i>Bacillus halodurans</i> NaChBac, NP_242367)	79
A.2 Growth media	79
A.3 Transforming <i>E. coli</i>	79
A.4 NaChBac purification.....	80
A.5 SDS-PAGE.....	80
B. NaChBac in liposomes	81
C. Knob complex.....	83
References	88
Acknowledgements	
Curriculum vitae	

List of publications

1. Chang, S. S.; Dijkman, P. M.; Wiessing, S. A.; Kudryashev, M., Determining the structure of the bacterial voltage-gated sodium channel NaChBac embedded in liposomes by cryo electron tomography and subtomogram averaging. *Sci Rep* 2023, 13 (1), 11523.
2. Sanchez, C. P.; Patra, P.; Chang, S. S.; Karathanasis, C.; Hanebutte, L.; Kilian, N.; Cyrklaff, M.; Heilemann, M.; Schwarz, U. S.; Kudryashev, M.; Lanzer, M., KAHRP dynamically relocates to remodeled actin junctions and associates with knob spirals in *Plasmodium falciparum*-infected erythrocytes. *Mol Microbiol* 2022, 117 (2), 274-292.
3. Dijkman, P. M.; Marzluf, T.; Zhang, Y.; Chang, S. S.; Helm, D.; Lanzer, M.; Bujard, H.; Kudryashev, M., Structure of the merozoite surface protein 1 from *Plasmodium falciparum*. *Sci Adv* 2021, 7 (23).

List of figures

- Figure 1.1 General process of cryo-EM
- Figure 1.2 Basic concepts of structure determination by single-particle analysis (SPA)
- Figure 1.3 The steps involved in single-particle cryo-EM workflow
- Figure 1.4 Increase in the number of EM map depositions in the Electron Microscopy Data Bank (EMDB) since 2010
- Figure 1.5 High-resolution sub-200 kDa structures obtained by single-particle cryo-EM analysis
- Figure 1.6 Subtomogram averaging (StA) in the cryo-electron tomography (cryo-ET) pipeline
- Figure 1.7 Scheme of cryo-ET and StA data processing workflow
- Figure 1.8 Trends in the determination of membrane protein structures by X-ray crystallography and single particle cryo-EM
- Figure 1.9 Scheme of different membrane mimetic systems
- Figure 2.1 Conformational cycle of a VGSC during an action potential
- Figure 2.2 Graphic workflow of Chapter 2
- Figure 2.3 Purification of NaChBac
- Figure 2.4 Reconstitution efficiency of NaChBac in proteoliposomes
- Figure 2.5 Optimization of proteoliposome reconstitution
- Figure 2.6 Cryo-images during optimization of NaChBac proteoliposome reconstitution
- Figure 2.7 Preparation of polarized NaChBac-containing liposomes
- Figure 2.8 Optimization of cryo-EM grid preparation
- Figure 2.9 Particle auto-picking on micrographs
- Figure 2.10 2D classification for the selection of good protein particles embedded in liposomes
- Figure 2.11 Visualization of NaChBac proteoliposomes by cryo-ET
- Figure 2.12 Protein identification on NaChBac proteoliposomes by template matching
- Figure 2.13 Particle extraction from NaChBac proteoliposomes using geometric modelling tools
- Figure 2.14 A workflow for structural determination of NaChBac embedded in liposomes by StA
- Figure 2.15 An overview of the dataset cleaning process with Dynamo
- Figure 2.16 Fourier shell correlation (FSC) curve of the masked map and slices through the structure of NaChBac map in liposomes along the z-axis

Figure 2.17 Structure of NaChBac embedded in liposomes with C4 symmetry

Figure 2.18 Structure of NaChBac in proteoliposomes and comparison to the structure in nanodiscs (EMD-21425)

Figure 3.1 People in humanitarian need in malaria-endemic countries as of December 2021

Figure 3.2 Electron micrographs of red blood cells infected with *Plasmodium falciparum*

Figure 3.3 Spiral-like feature of knob complex and model of knob formation structure

Figure 3.4 Graphic workflow of Chapter 3

Figure 3.5 Cryo-ET of knob spirals

Figure 3.6 Masks used for the StA analysis of spirals

Figure 3.7 Structure of the knob complex

Figure 3.8 Structural analysis of the knob complex

Appendix Figure B.1 Processing pipeline for tomogram reconstruction and subtomogram averaging

Appendix Figure C.1 Negative-staining image of erythrocyte ghost membrane

Appendix Figure C.2 Visualization of knob spirals in tomograms

Appendix Figure C.3 Masks used for spiral alignment

Appendix Figure C.4 StA and reconstruction of the knob complex

List of tables

Appendix Table B.1 Data processing statistics

Appendix Table C.1 Data processing statistics

Abbreviations

Two-dimension (2D)

Three-dimension (3D)

Artificial intelligence (AI)

Anabaena cyanobacterium sensory rhodopsin (ASR)

Adenosine triphosphate (ATP)

Aquaporin-1 (AQP1)

Cell adhesion molecule (CAM)

Cold field emission electron gun (CFEG)

3-[(3-Cholamidopropyl)dimethylammonio]-1-propanesulfonate (CHAPS)

3-[(3-Cholamidopropyl)dimethylammonio]-2-hydroxy-1-propanesulfonate (CHAPSO)

Critical micelle concentration (CMC)

Coronavirus disease 2019 (COVID-19)

Cryo-correlative microscopy (Cryo-CLEM)

Cryo-electron microscopy (Cryo-EM)

Cryo-electron tomography (Cryo-ET)

Cryo-focused ion beam (Cryo-FIB)

Contrast transfer function (CTF)

Column volume (CV)

n-Decyl-beta-Maltoside (DM)

n-Dodecyl β -d-maltoside (DDM)

Detective quantum efficiency (DQE)

Epidermal growth factor receptors (EGFR)

Empty liposome (ELS)

Electron Microscopy Data Bank (EMDB)

Electron paramagnetic resonance (EPR)

Femtosecond (fs)
Fourier shell correlation (FSC)
G protein-coupled receptor (GPCR)
Human immunodeficiency virus (HIV)
Immobilized metal chelate affinity chromatography (IMAC)
Knob-associated histidine-rich protein (KAHRP)
Lipidic cubic phase (LCP)
Light-harvesting complex II (LHC II)
Lauryl maltose neopentyl glycol (LMNG)
Light-dependent protochlorophyllide oxidoreductase (LPOR)
Lipid-to-protein ratio (LPR)
Leucine-rich repeat kinase 2 (LRRK2)
Merozoite surface protein 1 (MSP-1)
Membrane scaffold protein (MSP)
Nuclear magnetic resonance (NMR)
Nuclear pore complex (NPC)
Pore domain (PD)
P. falciparum erythrocyte membrane protein 1 (PfEMP1)
Phosphoethanolamine (POPE)
Phosphatidylglycerol (POPG)
Escherichia coli outer-membrane protein A (OmpA)
n-Octyl- β -d-Glucopyranoside (OG)
Natronomonas pharaonis phototaxis receptor sensory rhodopsin II (pSRII)
Red blood cell (RBC)
Ryanodine receptor (RyR)
Subtomogram averaging (StA)
Sapoin-lipoprotein (salipro)
S-adenosylmethionine-IV (SAM-IV)
Severe acute respiratory syndrome coronavirus 2 (SARS-CoV-2)
Small-angle X-ray scattering (SAXS)
Structure-based drug discovery (SBDD)
Sickle cell disease (SCD)
Sodium dodecyl sulfate (SDS)
Size-exclusion chromatography (SEC)

Scanning electron microscopy (SEM)
Serial femtosecond crystallography (SFX)
Styrene-maleic acid (SMA)
Styrene-maleic acid co-polymer lipid particles (SMALPS)
Signal-to-noise ratio (SNR)
Single-particle analysis (SPA)
Sarcoplasmic reticulum (SR)
Transmission electron microscopy (TEM)
Transient receptor potential cation channel subfamily V member 1 (TRPV1)
Mus musculus mitochondrial translocator protein (TSPO)
Polyoxyethylene sorbitol ester (Tween)
Voltage-gated ion channel (VGIC)
Voltage-gated sodium ion channel (VGSC)
Voltage-sensing domain (VSD)
X-ray free-electron laser (XFEL)
Yersinia enterocolitica transmembrane domain of adhesin A (YadA)

Chapter 1

Introduction

1.1 Membrane proteins

Biological membranes serve as physical barriers in cells and organelles, enabling the maintenance of chemical or ionic gradients that are essential for triggering various integral, peripheral, or lipid-anchored membrane proteins, necessary for their life-essential functions^{1,2}.

Membrane proteins are embedded in biological membranes and perform crucial roles in cellular activities. Among them, membrane receptor proteins, including glutamate receptors³, 5-hydroxytryptamine (Serotonin) receptors⁴, and epidermal growth factor receptors (EGFR)⁵, which receive extracellular molecules and transmit signals to the cell interior. These extracellular molecules encompass neurotransmitters, hormones, growth factors, cytokines, cell adhesion molecules, and nutrients. Through signal transduction, they initiate cascading changes in cell metabolism and activity. Furthermore, membrane transport proteins, responsible for transporting ions or molecules across the membrane. Channel proteins, such as ion channels and aquaporins⁶, facilitate the movement of ions, water molecules, or small hydrophobic molecules down their concentration gradients via facilitated diffusion. ATP-powered pumps, like the sodium-potassium pump⁷, are electrogenic transmembrane ATPases that utilize ATP energy to export three sodium ions and import two potassium ions, thereby maintaining the resting potential across the membrane. In addition, membrane-embedded enzymes, such as ATP synthase⁸, oxidoreductase, transferase, and hydrolase, which catalyze various reactions in cells. Also, cell adhesion molecules (CAMs), which are proteins that facilitate cell recognition and interaction with neighboring cells or the extracellular matrix, and they are particularly involved in processes such as immune response⁹. Due to their crucial roles, membrane proteins represent potential targets for over 50% of currently available drugs¹⁰⁻¹³. Additionally, understanding the structural characteristics of membrane proteins is essential for elucidating their functional mechanisms and their applications in new drug discovery.

However, the study of membrane proteins has unique challenges due to their hydrophobic nature, limited expression levels, and inherent flexibility. These characteristics make it difficult to obtain their structure information for comprehensive understanding their functions and mechanisms. Traditional high-resolution techniques like X-ray crystallography and nuclear magnetic resonance (NMR) are less effective in determining the atomic resolution structures of membrane proteins compared to soluble proteins. Despite their functional significance, the structural determination of membrane proteins has remained a challenging task for decades. Currently, advancements in electron microscopy of frozen-hydrated samples (Cryo-electron microscopy, Cryo-EM) have revolutionized the field by providing unprecedented opportunities for studying the structures of membrane proteins and other biological macromolecules. Single-particle analysis (SPA) enables the determination of high-resolution three-dimensional (3D) structures using minimal amounts of specimen without the need for crystallization^{14, 15}. Additionally, cryogenic electron tomography (Cryo-ET) and subtomogram averaging (StA) offer the ability to study membrane protein complexes, cellular architecture, and molecular interactions (or so-called molecular sociology) *in situ* while preserving close-to-life conditions^{16, 17}. These cutting-edge methods have led to a wealth of information not only regarding the structural basis for rational drug design but also shedding light on cellular processes that were previously inaccessible with traditional structural biology techniques¹⁸. By overcoming the limitations of classical approaches, cryo-EM and related techniques have opened new avenues for unraveling the intricate molecular landscapes of membrane proteins and enhancing our understanding of cellular function and disease mechanisms.

1.2 From TEM to Cryo-EM

Transmission electron microscopy (TEM) is a powerful microscopy technique in which an electron beam is transmitted through a thin specimen to form an image used in the physical, chemical, and biological sciences. TEM has found widespread applications in various fields, including semiconductor research, materials science, and cancer research. In biological sample preparation for TEM, negative staining techniques are commonly employed. This involves using substances such as uranyl acetate or uranyl formate to stain isolated macromolecules¹⁹. In the case of embedded sections from chemical fixation, osmium tetroxide staining can be applied to enhance image contrast and preserve tissue lipids²⁰. Negative-staining EM provides valuable information about protein homogeneity and overall outer shape, but it does not reveal

internal structural details. It is important to note that the chemical staining process at room temperature may introduce some degree of distortion and sample damage.

Cryogenic electron microscopy (cryo-EM) as a microscopy technique has emerged, enabling the imaging of biological samples at cryogenic temperatures. The biological specimen is preserved in an amorphous ice layer for the structure determination in their near-native state without the need for chemical staining. Since the first electron microscope was developed by Ernst Ruska in 1933, Jacques Dubochet and his colleagues developed a plunge freezing method of vitrification of samples, in which thin films of water form a glass-like ice rather than a crystalline ice^{21, 22}. Joachim Frank developed image processing techniques, allowing the reconstruction of 3D protein structures from two dimensional (2D) images of individual protein particles²³⁻²⁵. Henderson and Unwin overcame challenges in determining the structures of membrane proteins using electron microscopy, achieving the first 7-Å resolution map of bacteriorhodopsin through electron crystallography from unstained specimens²⁶, and finally Richard Henderson and his colleagues obtained the first cryo-EM structure of bacteriorhodopsin at an impressive resolution of 3.5 Å²⁷. The groundbreaking achievements in cryo-EM, particularly in single particle analysis (SPA), has been selected as the Method of the Year 2015²⁸. In 2017, the Nobel Prize in Chemistry was awarded to Jacques Dubochet, Joachim Frank, and Richard Henderson for their pioneering work on the use of cryo-EM to solve high-resolution structures of biomolecules (**Figure 1.1**).

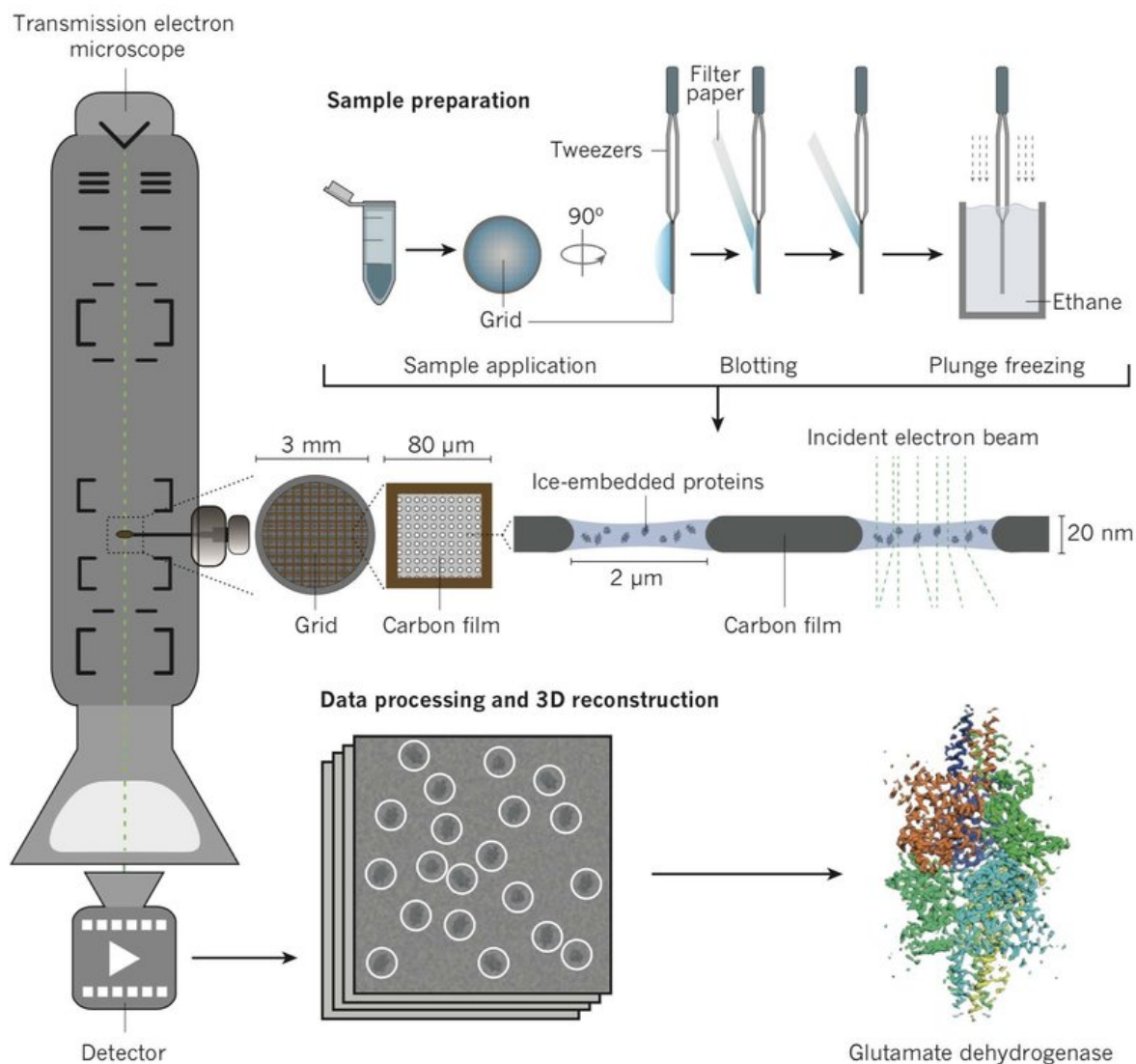


Figure 1.1 General process of cryo-EM. Protein structure determination through cryo-EM involves several stages: sample grid preparation, data collection and data processing followed by 3D reconstruction. Image from²⁹.

To date, SPA stands as a mainstream technique in the field of structural biology, enabling the study of complex systems that pose challenges to traditional structural characterization methods. Furthermore, cryo-electron tomography (Cryo-ET) has emerged as a powerful tool for visualizing the molecular architecture of preserved cellular landscapes in three dimensions. By employing subtomogram averaging (StA), macromolecular and supramolecular structures can be determined *in situ* with near-atomic resolution. These advancements have significantly expanded our ability to explore and understand the molecular world and uncover new insights into the complexities of life.

1.2.1 Single-particle cryo-electron microscopy

Structure determination of protein complexes and membrane proteins through X-ray crystallography is hindered by the requirement for large sample quantities and the bottleneck of protein crystallization. NMR does not need crystallization for structure determination. However, it requires substantial sample amounts as well as isotopic enrichment, and size limitations have generally restricted this technique to small biological molecules.

Single-particle cryo-EM (or Single particle analysis, SPA) overcomes these limitations as it does not rely on crystallization and only requires small sample volumes (approximately 20 μL at a concentration of 0.5 mg/mL) for data collection. This technique is particularly well-suited for studying challenging biological targets close to their native environments. For instance, it enables the investigation of full-length, wild-type proteins, thereby minimizing the potential effects of truncations or mutations that are present in abundance on target proteins for protein stability reasons. For the structure determination of membrane proteins, it can be studied in solution with mild detergents or membrane mimetic systems, thereby mitigating the crystallization artifacts often observed on protein surfaces. Specimens for single-particle cryo-EM typically consist of purified sample on holey carbon film-supported copper grids in thin, vitreous ice. An optimized specimen should prevent particle adsorption to air-water interfaces and ensure a high density of molecules in a broad range of orientations³⁰. Micrographs of the specimens are taken using an electron microscope for subsequent image processing (**Figure 1.2**). Particle coordinates are identified and extracted from the micrographs, followed by 2D and 3D classification, 3D structure refinement, and map evaluation and validation to generate accurate structural information (**Figure 1.3**)³¹.

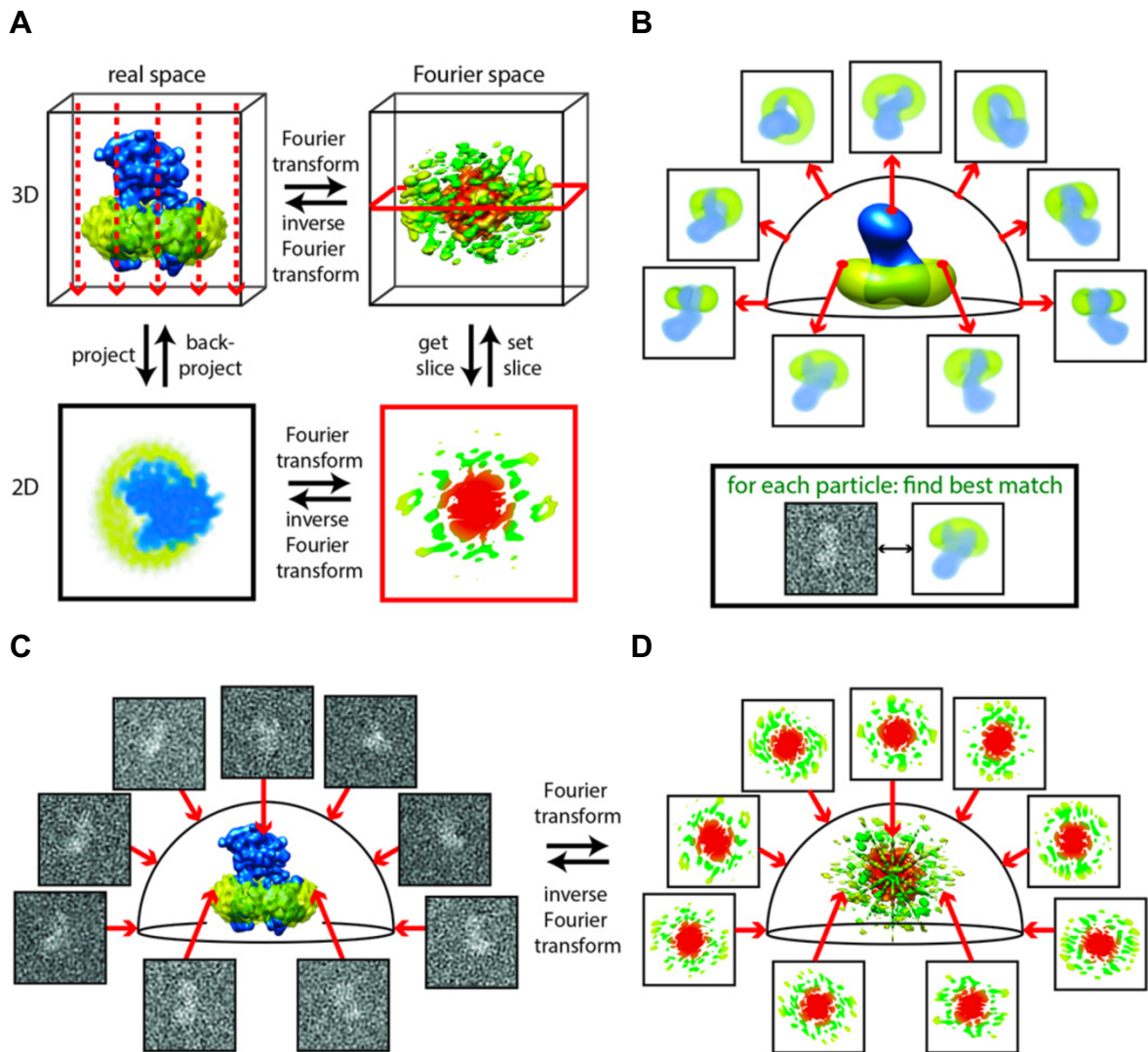


Figure 1.2 Basic concepts of structure determination by single-particle analysis (SPA). (A) The projection-slice theorem establishes that the 2D projection of a 3D object in real-space (left column) corresponds to extracting a central 2D slice from the 3D Fourier transform of that object (right column), and then applying an inverse Fourier transform to return to real-space. (B) Experimental projections of a 3D object are collected in various orientations as references. Each experimental projection is compared with all references to find the best match based on similarity. (C) The orientations of all experimental projections are determined relative to the 3D structure. (D) The 3D reconstruction is calculated by positioning the 2D Fourier transforms of all experimental projections into the 3D Fourier transform and performing an inverse Fourier transform to obtain the final 3D structure. Image from¹⁵.

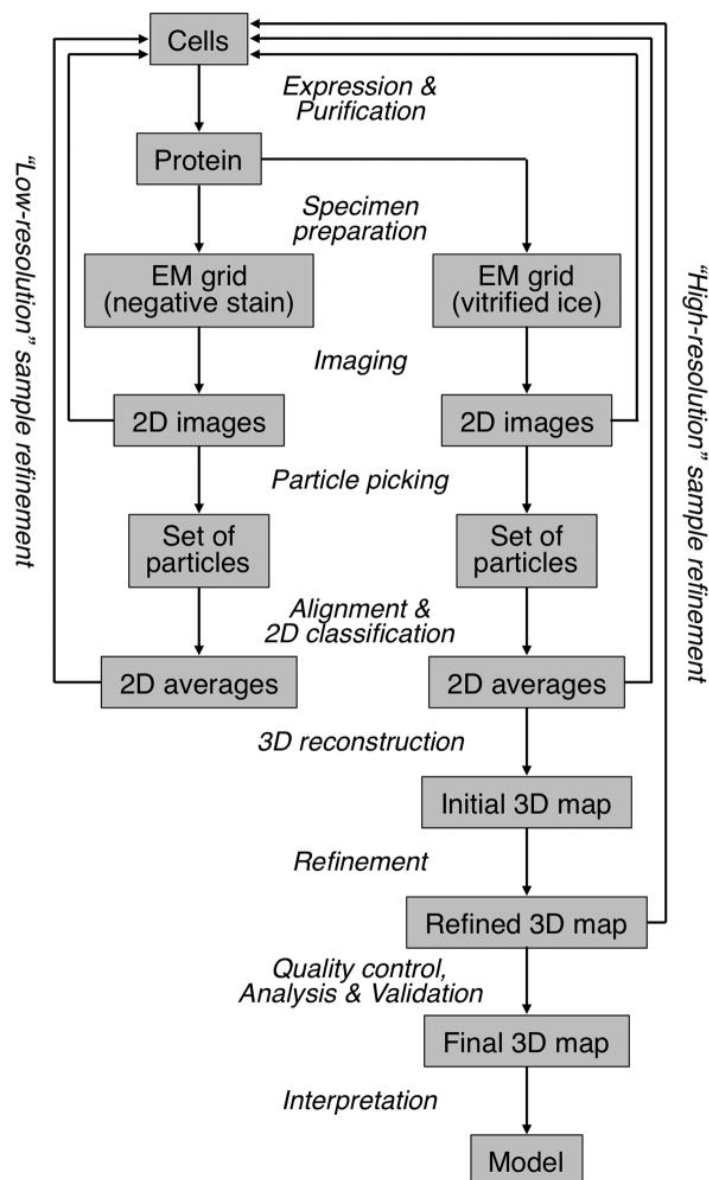


Figure 1.3 The steps involved in single-particle cryo-EM workflow. Beginning with a purified sample, the process involves with a characterization of the specimen in negative-staining EM and cryo-EM. After the sample optimization, cryo-grid screening, and data acquisition, the micrographs, 2D class averages and 3D maps obtained with vitrified specimens may indicate the need for further improvement of the sample quality to reach near-atomic resolution. Image from³¹.

The field of cryo-EM faced criticism for many years due to the limited resolution of most single-particle cryo-EM maps, often worse than 10 Å, leading many to deride cryo-EM structures as “blob-ology”. Until 2010s, significant advancements in instrumentation and software have dramatically improved the potential of SPA to produce structures at atomic resolutions, and it marked cryo-EM into a new era known as the “Resolution Revolution”³².

These advancements included the development of stable specimen stages, improved microscope vacuums, and automated data collection with the introduction of direct electron detection cameras³³⁻³⁵. Detector performance can be characterized by the detective quantum efficiency (DQE), which describes the signal and noise performance of digitally recorded images over the spatial frequency range³⁶. Combining direct electron detection with single electron counting has greatly improved the DQE, and the fast readout rate of these cameras not only showed beam-induced motion of vitrified specimen, but also enabled computational solutions by treating images as movies rather than individual exposures³⁷. Concurrently with these cameras, powerful maximum-likelihood image processing packages, such as RELION, became available, offering a user-friendly tool for defining reliable and objective criteria using a Bayesian approach and handling heterogeneous samples for single-particle image averaging^{38, 39}. Thus, we have been experiencing a flood of cryo-EM structure depositions at better than 4-Å resolution since 2014, marking a significant breakthrough in the field (**Figure 1.4**)⁴⁰.

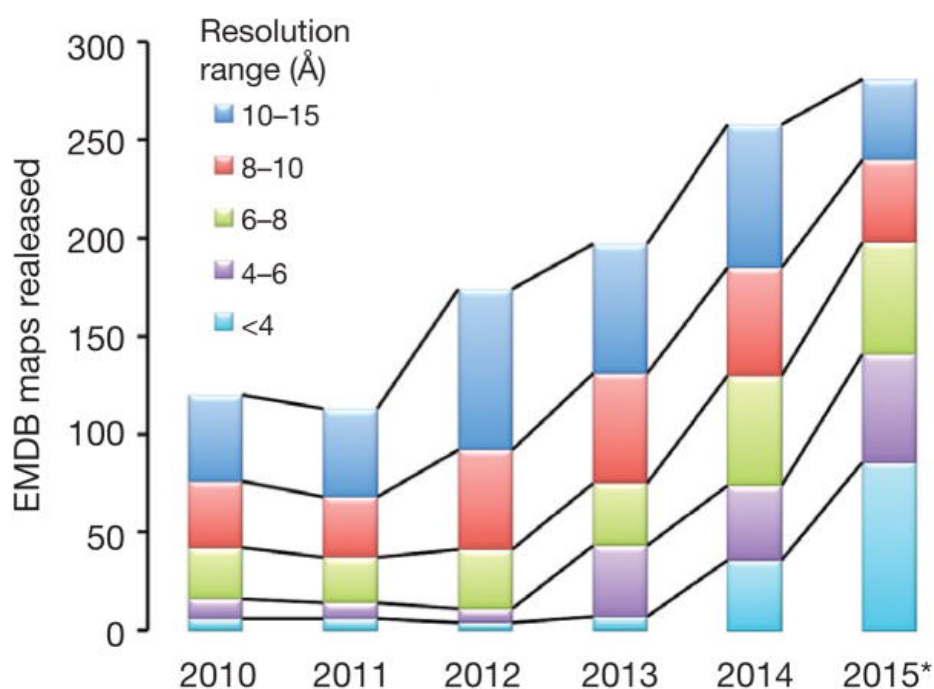


Figure 1.4 Increase in the number of EM map depositions in the Electron Microscopy Data Bank (EMDB) since 2010. The most notable growth is in the number of structures resolved at better than 4-Å resolution starting from 2014. Image from⁴⁰.

The direct visualization of individual atoms in protein molecules is crucial for understanding their roles in biological processes and gaining mechanistic insights into protein function. Achieving resolutions better than 4 Å allows for the possibility of atomic model building.

However, to directly visualize individual atoms in proteins, an atomic resolution (better than 1.5 Å) is required. Recent developments in electron microscope hardware, such as the implementation of a new cold field emission electron gun (CFEG), an improved energy filter, and the use of the new Falcon direct electron camera, have significantly enhanced the signal-to-noise ratio (SNR) of cryo-EM images. This has led to the determination of high-resolution structures, such as the human $\beta 3$ GABA_A receptor at 1.7 Å resolution and mouse apoferritin at 1.22 Å resolution⁴¹. Also, a prototype cryo-EM equipped with additional electron-optical elements, including a monochromator to reduce energy spread of the electron beam and an aberration corrector to minimize optical aberrations, enabled the acquisition of a 1.25 Å-resolution structure of human apoferritin⁴². These advancements have further improved the performance of the instrument and expanded the capabilities of cryo-EM in achieving atomic-level resolution.

Yet, high-resolution structural studies of smaller biological molecules using single-particle cryo-EM still remain significant challenges. Specimens with low molecular mass have fewer scattering atoms, leading to a poor SNR in micrographs when embedded in vitreous ice. Due to advancements in cryo-EM technologies currently, such as sample preparation, imaging, and data processing algorithms, have greatly improved our ability to visualize and analyze small biological targets (**Figure 1.5**)⁴³. In 2016, the first breakthrough was achieved with the determination of a 3.8-Å structure of the ~93 kDa isocitrate dehydrogenase, surpassing the 100 kDa barrier⁴⁴. Subsequently, a 3.7-Å structure of the ~40 kDa S-adenosylmethionine-IV riboswitch RNA is the smallest target resolved without a molecular scaffold to date⁴⁵, which is close to the predicted 38 kDa limit of single-particle cryo-EM⁴⁶. Regarding membrane protein studies, it is now feasible to determine the structures of sub-100 kDa membrane proteins at a resolution better than 5 Å⁴⁷.

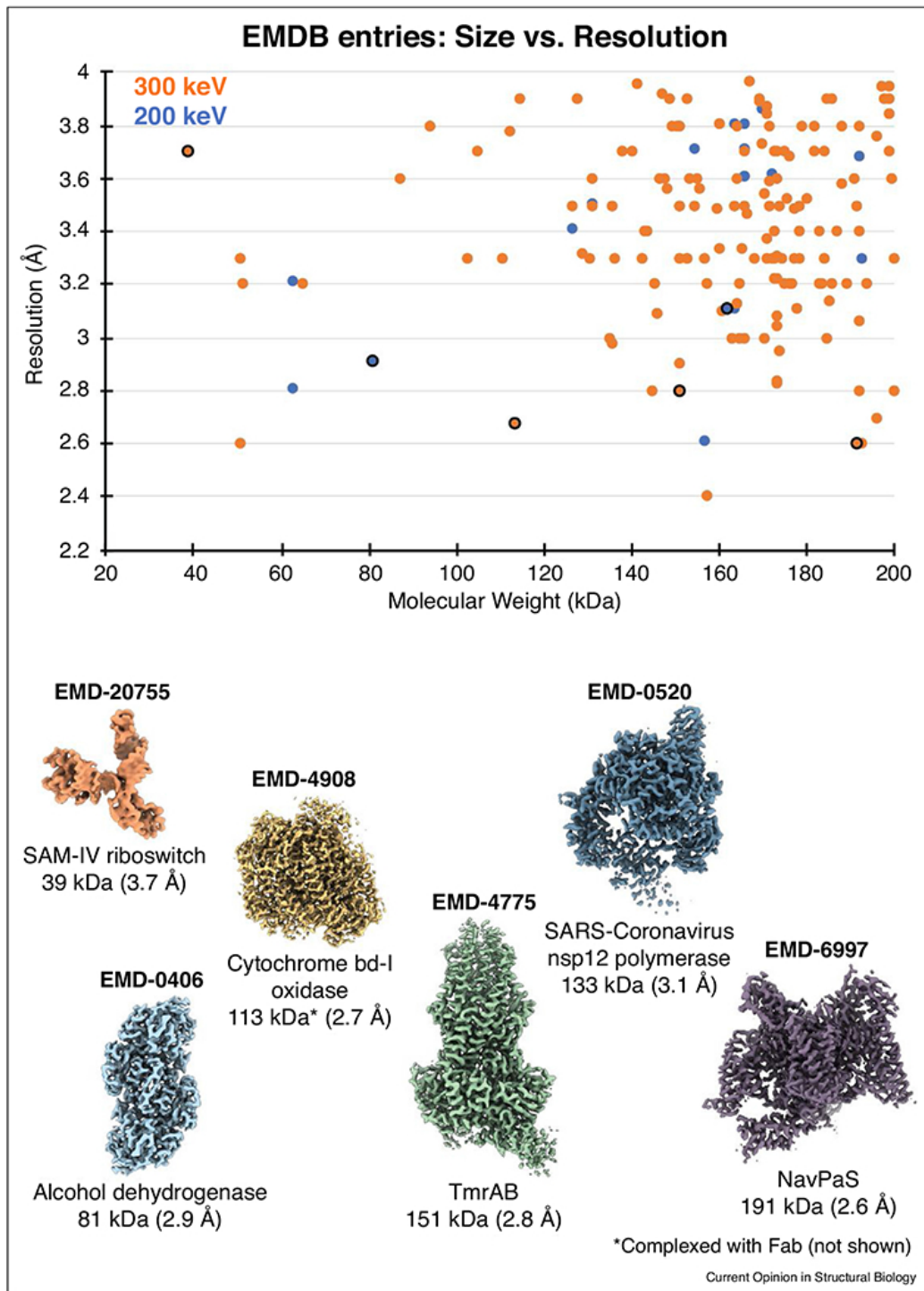


Figure 1.5 High-resolution sub-200 kDa structures obtained by single-particle cryo-EM analysis. Top: Electron Microscopy Data Bank (EMDB) entries of complexes with molecular weights below 200 kDa and resolutions better than 4 Å are plotted. Bottom: Cryo-EM density is shown for selected entries (outlined in black in the plot above), along with the corresponding EMDB identifier, molecule name, molecular weight, and reported resolution. It is notable that the cryo-EM structure of a 40 kDa S-adenosylmethionine-IV (SAM-IV) riboswitch RNA is the smallest target with a resolution better than 4 Å. Image from⁴³.

With improvements such as automated sample vitrification instruments may mitigate sample adsorption to the air-water interface by shortening the sample dispense-to-plunge time and may offer the better control for thin ice with reproducibility⁴⁸⁻⁵¹. The ongoing development of a continuous-wave focused phase plate⁵² that can generate a constant phase shift without information loss might be possible to yield higher-quality data and improved resolution for small target proteins. Machine learning techniques applied to the heterogeneous cryo-EM reconstruction of protein samples have also shown great potential. These methods are able to characterize conformational and compositional heterogeneity, identify new structural states, and visualize large-scale continuous motions and dynamic features in biological samples^{53, 54}. By integrating additional approaches to accelerate data acquisition and improve sample quality, single-particle cryo-EM has the potential to become a routine method for high-throughput screening of small molecule modulators and structure-based drug discovery (SBDD) in the foreseeable future.

1.2.2 Cryo-electron tomography (Cryo-ET) and subtomogram averaging (StA)

Visualizing the structures of macromolecular assemblies in cells can provide direct insights into their functions and mechanisms. However, the majority of structural biology techniques typically require the purification of macromolecular complexes to isolate them from their natural cellular habitat. As a consequence, information regarding the context and molecular interactions underlying cellular processes and phenomena is often lost.

Cryo-electron tomography (Cryo-ET) can provide low-resolution 3D views of tissues, cells, organelles, or viruses. To achieve this, biological samples are preserved in a close-to-native state by the flash freezing process, thinned to an appropriate thickness, and then imaged using an electron microscope. A series of micrographs are recorded as the sample is tilted along an axis, and these micrographs are subsequently aligned and merged using computational techniques to reconstruct a 3D volume, known as a tomogram⁵⁵. To obtain high resolution molecular information from the tomograms, subtomogram averaging (StA) can be employed (**Figure 1.6**). By computationally identifying, extracting, mutually aligning, and averaging macromolecular complexes that appear in multiple copies and orientations within the 3D tomographic reconstructions, it is possible to amplify the signal and achieve higher resolution and to map the spatial distribution of molecules within the cells (**Figure 1.7**)⁵⁶.

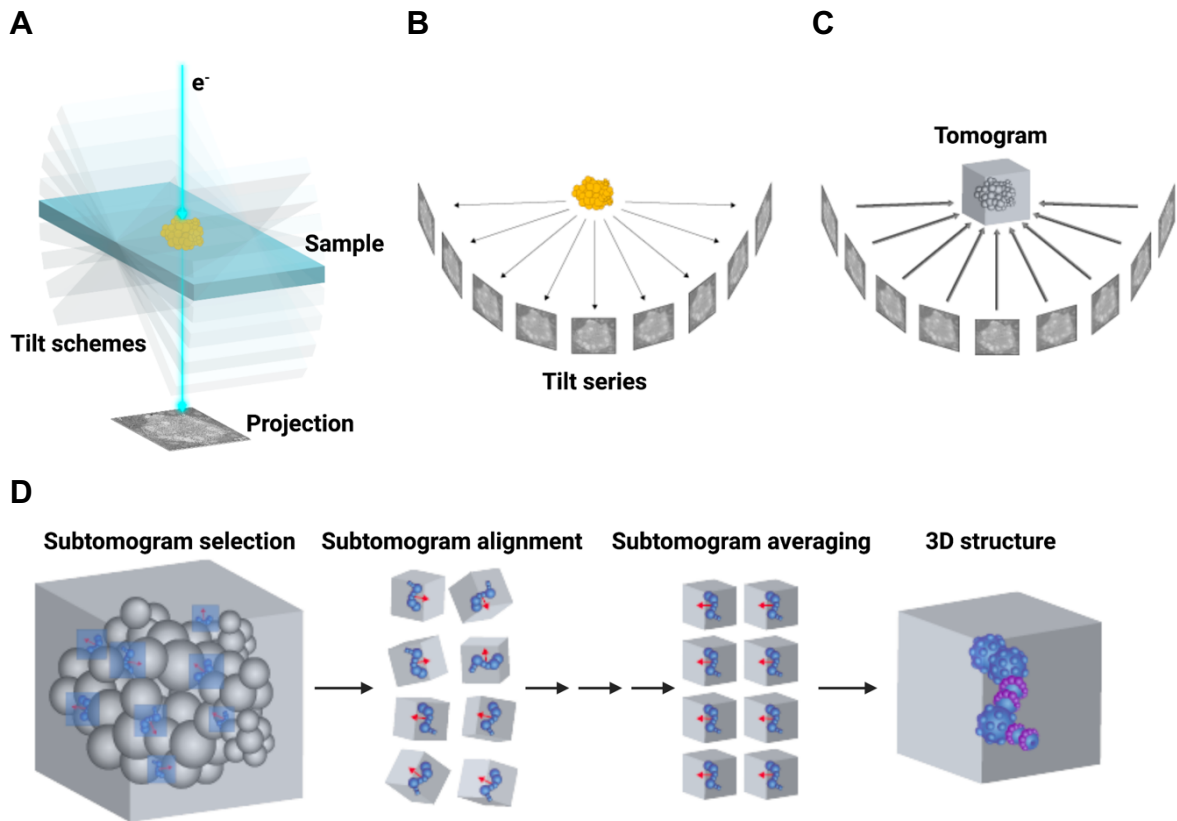


Figure 1.6 Subtomogram averaging (StA) in the cryo-electron tomography (cryo-ET) pipeline. (A) The sample stages are tilted, typically from -60° to $+60^{\circ}$, to record projection images of the specimen from various angles. (B and C) These 2D tilt-series data, are then computationally reconstructed to generate a 3D tomogram. Specific structural features of interest are identified and segmented to create 3D annotations, which can be utilized for both visualization and statistical studies. (D) Repetitive structures in a tomogram can be extracted as subtomograms for further processing steps such as alignment, classification, averaging, and refinement. These steps allow the generation of a 3D structure by combining information from multiple subtomograms.

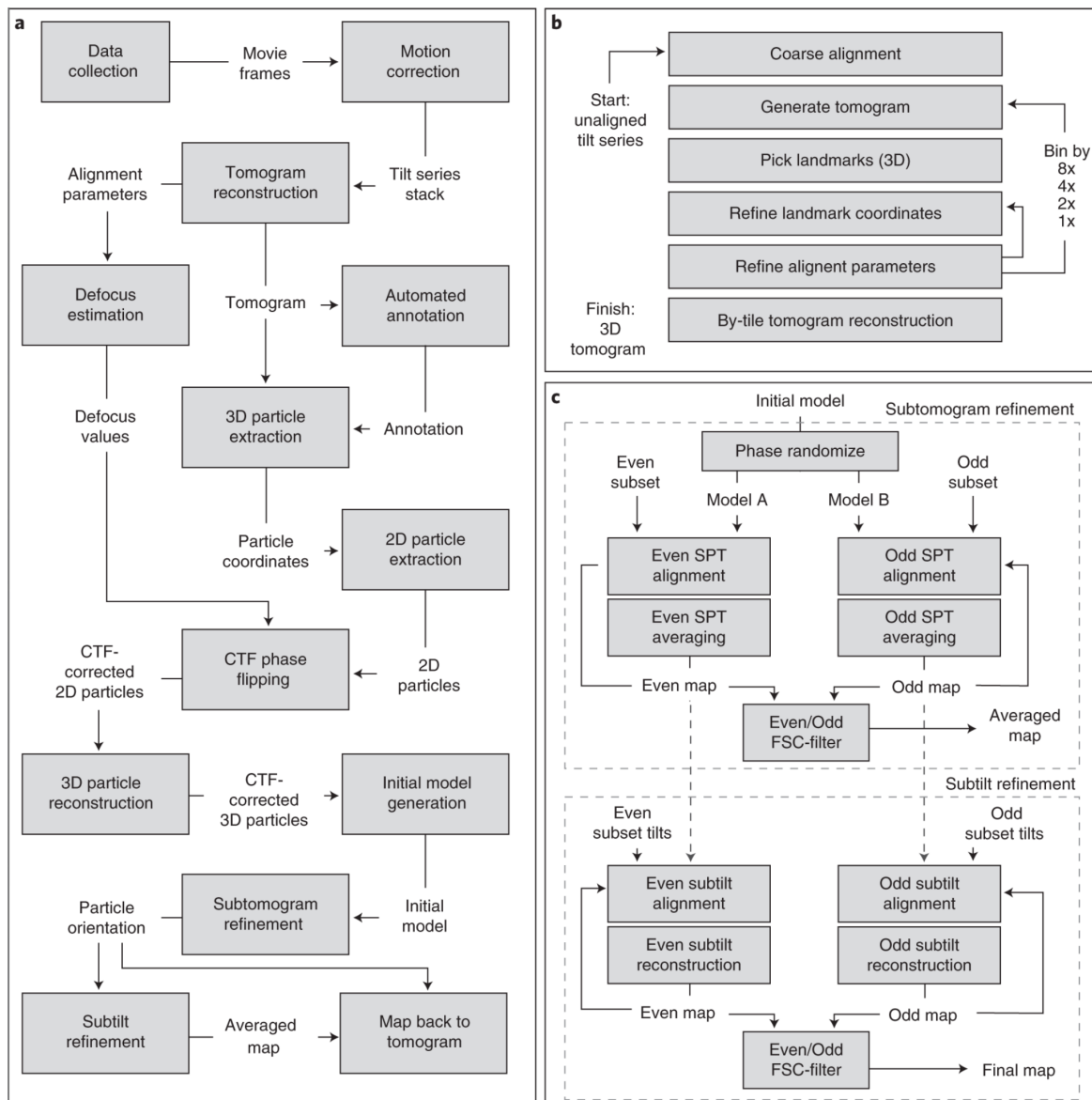


Figure 1.7 Scheme of cryo-ET and StA data processing workflow. (a) Overall workflow. (b) Workflow of tomogram reconstruction. (c) Workflow of subtomogram refinement and map evaluation. Image from⁵⁶.

A critical limitation of cryo-ET is the size of the samples that can be imaged in vitrified ice. The thickness limitation of 300-500 nm restricts the imaging to samples such as viruses, prokaryotic cells, extracted cellular fractions, and isolated organelles⁵⁷. However, for most eukaryotic cells, multicellular organisms, or tissues, which are thicker than 500 nm, cryo-ET is not accessible at a resolution sufficient for molecular interpretation *in situ*^{58,59}. To overcome this limitation, a workflow involving cryo-correlative microscopy (cryo-CLEM) and cryo-focused ion beam (cryo-FIB) milling techniques for the preparation of cryo-lamellas from frozen-hydrated cells has been developed. In cryo-CLEM, targets of interest are identified and

localized in a cryo-fluorescence light microscope⁶⁰, and then these targets can be thinned using cryo-FIB milling⁶¹⁻⁶³, achieving thicknesses as thin as 100-200 nanometers⁶⁴⁻⁶⁷. By combining these technical developments, cryo-ET and StA allow us to understand the in-cell architecture of the nuclear pore complex (NPC)⁶⁸, visualize the nuclear translocation of HIV-1 capsids⁶⁹, investigate the dynamics of NPC conformation *in cellulo*⁷⁰, and visualize ribosomes and their intermediates during a translation elongation cycle in living cells with high detail^{71, 72}. Cryo-ET and StA also offer a bridge between *in vitro* structural biology and biomedical research. For example, cryo-ET and StA revealed double-helical filaments of Parkinson's disease-linked leucine-rich repeat kinase 2 (LRRK2) around microtubules and the dimerization interfaces in cellular environment, providing structural insights for the design of LRRK2 therapeutic inhibitors⁷³. *In situ* structural analysis of SARS-CoV-2 spike proteins uncovered their flexible connections to the viral surface, and the spike was shielded by an extensive glycan coat. These native structures can potentially contribute to the development of safe vaccines⁷⁴. Imaging on Huntington's disease patient-derived induced pluripotent stem cells revealed organelle phenotypes that may serve as pathological biomarkers for diagnostics development⁷⁵.

Developments of hardware and software, including direct electron detectors and beam-induced motion correction algorithms are vital for enhancing the resolution of single particle cryo-EM structure, and these advancements also improve the visualization of structural features in tomograms, as well as the resolution determination through StA. Several structures have been revealed at the resolution of protein secondary structure using StA. Examples include an 8-Å structure of the hepatitis B capsid⁷⁶ and an 8.8-Å structure of the immature HIV-1 capsid in intact virus particles⁷⁷. With further optimizations of tilt-series data acquisition and data processing, a 3.9-Å structure of an immature HIV-1 particle was able to have an atomic model build-in, revealing a network of intra- and intermolecular interactions involved in immature HIV-1 assembly⁷⁸. Moreover, an efficient 3D-contrast transfer function (CTF) correction tool with improved correlation at higher frequencies enabled the determination of a 3.4-Å structure of HIV capsids⁷⁹. The recent development of the Warp⁸⁰-RELION³⁹-M pipeline for frame and tilt-series cryo-EM data refinement has further propelled this field, and a high-resolution map of a ribosome-antibiotic complex was obtained at 3.5 Å resolution in cells⁸¹.

Cryo-ET and StA have the potential to image the entire proteome of a cell, enabling visual proteomics and the generation of comprehensive molecular maps of cellular landscapes in a close-to-life state with subnanometer resolution⁸². Improvements in sample preparation, such

as cryo-lamellae preparation techniques^{83,84}, fast data acquisition methods⁸⁵, and advanced data interpretation techniques, including AI-based methods for tomogram reconstruction, macromolecule identification, and particle localization in their cellular context⁸⁶⁻⁸⁸, these continued advancements in technology and methodology have further enhanced cryo-ET and StA as powerful tools. Together, cryo-ET and StA provide valuable three-dimensional information about macromolecular complexes at the molecular scale, and allow us to understand cellular phenomena in terms of interaction networks.

1.3 Cryo-EM study of membrane proteins in structural biology

Getting directly to the structure is a most straightforward way to understand life at the molecular scale. Among the proteins encoded in the human genome, approximately 20-30% are membrane proteins⁸⁹, which mediate a broad range of biological processes. However, obtaining structural information for membrane proteins has always been a challenging endeavor from early days to now on.

Since the groundbreaking achievement of resolving the high-resolution X-ray crystal structure of an integral membrane protein, the photosynthetic reaction center, reported by Hartmut Michel and colleagues in 1985, significant progress has been made in the structural determination of membrane proteins. Over the past decades, the structures of various membrane proteins, such as F₁-ATPase⁹⁰ and the first ion channel KcsA potassium channel⁹¹, have been successfully resolved. The utilization of the lipidic cubic phase (LCP) method, which involves a crystalline phase with a toothpaste-like consistency, has played a pivotal role in facilitating the crystallization of membrane proteins⁹². LCP has enabled the determination of more protein structures like bacteriorhodopsin, marking a significant milestone⁹³, and G protein-coupled receptors (GPCRs)⁹⁴. Despite these advancements, it still remains a challenge to crystallize many membrane proteins sufficiently to obtain usable X-ray diffraction patterns for structure determination.

Membrane-protein NMR occupies a unique niche in structural biology, providing valuable information into structure, dynamics, folding, and ligand interactions of membrane proteins. Since the first report of the NMR structure of the *Escherichia coli* outer-membrane protein A (OmpA)⁹⁵, notable successes have been achieved in determining the structures of other

membrane proteins, including pSRII (*Natronomonas pharaonis* phototaxis receptor sensory rhodopsin II)⁹⁶, TSPO (*Mus musculus* mitochondrial translocator protein, a cholesterol and porphyrin importer into mitochondria)⁹⁷, YadA (*Yersinia enterocolitica* transmembrane domain of adhesin A, an outer-membrane autotransporter)⁹⁸, and ASR (*Anabaena* cyanobacterium sensory rhodopsin)⁹⁹ using solution NMR or solid-state NMR techniques. However, NMR analysis of membrane proteins also faces special challenges, including sample preparation requiring large and concentrated membrane protein samples, size limitation within the 10- to 40-kDa molecular mass range, spectral crowding leading to low sensitivity, and sparse data accumulation. Therefore, hybrid structural approaches combining NMR with other techniques such as electron paramagnetic resonance (EPR) spectroscopy, fluorescence spectroscopy, and computational simulation have been commonly employed to study the structure, dynamics, and function of membrane proteins^{100, 101}.

X-ray free-electron lasers (XFELs) and serial femtosecond crystallography (SFX) have revolutionized the study of membrane proteins, enabling investigations into their structure, dynamics, and function at near-atomic resolution and in the femtosecond to millisecond time regime with microcrystals^{102, 103}. As the XFEL pulses are not only ultrabright ($10e^{12}$ photons per pulse) but also ultrafast (10-50 fs), allowing for the “diffraction before destruction” principle to avoid most forms of radiation damage¹⁰⁴. Together with time-resolution up to the femtosecond range, a 2.9 Å-resolution SFX structure of the trimeric photosystem I, as an example on structure determination of large membrane protein complexes (> 1 MDa) with XFELs. Nevertheless, the development of low sample consumption injection systems is essential, particularly for membrane proteins that are challenging to express and isolate in large quantities, as a large fraction of the sample is typically wasted in between pulse trains¹⁰⁵. Continued advancements in sample delivery techniques and efficient utilization of limited sample quantities are crucial for further progress in XFEL-based studies of membrane proteins.

Solution small-angle X-ray scattering (SAXS) is another powerful technique for studying protein-protein and protein-ligand interactions, as it allows for the quantification of conformational changes and structural rearrangements. Unlike crystallography, SAXS does not require protein crystallization, making it a valuable tool for investigating solubilized membrane proteins. By providing low-resolution (~10 Å resolution) structural information, SAXS can complement existing studies and help fill in missing details¹⁰⁶.

Cryo-electron microscopy (cryo-EM) has already held a promising solution for studying membrane proteins at atomic resolution (**Figure 1.8**)¹⁰⁷. Both cryo-EM single-particle analysis (SPA) and cryo-electron tomography (cryo-ET) combined with subtomogram averaging (StA) have proven their ability to overcome traditional challenges associated with studying membrane proteins in a wide range of protein size, including low expression yields and limited stability in detergent micelles, among others. With more improvements of cryo-EM technologies, high-resolution structures of membrane proteins *in vitro* can allow people to understand their mechanisms and functions, and to facilitate the design and optimization of new therapeutic agents. Furthermore, there has been significant growth in the structural characterization of membrane proteins *in situ*, as studying biomolecules within their physiological context is an ultimate goal in structural biology for a comprehensive understanding of molecular networks in cells.

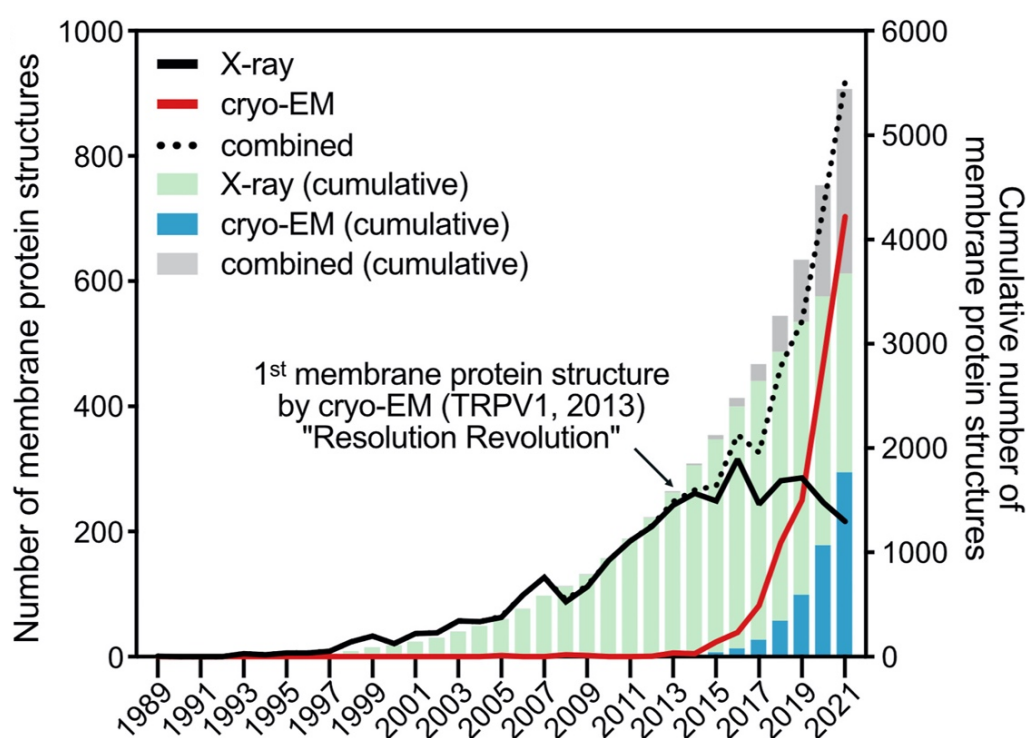


Figure 1.8 Trends in the determination of membrane protein structures by X-ray crystallography and single particle cryo-EM. Since 2010s, the advancements in cryo-EM have greatly improved the capability of SPA to achieve atomic-resolution structures of membrane proteins. Numbers per year are shown as lines (solid black for X-ray, solid red for cryo-EM, dotted black for X-ray and cryo-EM combined) and cumulative numbers are shown as bars (green for X-ray, blue for cryo-EM, gray for X-ray and cryo-EM combined). Image from¹⁰⁷.

1.3.1 Membrane protein structures *in vitro*

The determination of membrane protein three-dimensional maps by electron crystallography with cryo-EM was a milestone to a number of successful membrane protein research in the early days. Structures of various membrane proteins such as bacteriorhodopsin²⁷, Light-harvesting complex II (LHC II)¹⁰⁸, aquaporin-1 (AQP1)¹⁰⁹, microsomal glutathione transferase¹¹⁰, and nicotinic acetylcholine receptor¹¹¹⁻¹¹³ were obtained at resolutions ranging from 3 to 6 Å. Still, electron crystallography required laborious 2D crystallization screening and optimization, similar to X-ray crystallography, but with less developed tools, for obtaining good electron diffraction patterns. As a cryo-EM technique, electron crystallography had limitations in the structure determination of membrane proteins until the emergence of single-particle cryo-EM technique. With single-particle cryo-EM, structures of even relatively small membrane proteins with sub-100 kDa molecular mass can now be determined without the need for crystals, and at considerably higher resolutions⁴⁷.

Due to the amphipathic nature of membrane proteins, their production, purification, and isolation pose significant challenges compared to soluble proteins. To maintain the membrane protein fold in an aqueous buffer after disrupting lipid membranes, the use of detergents is common and often essential. Detergents can support membrane proteins in a non-bilayer environment by forming detergent micelles. These amphipathic molecules consist of a large headgroup and a single aliphatic chain, and above a certain critical micelle concentration (CMC) in aqueous media, they spontaneously assemble into small, globular micellar structures. The choice of detergent in membrane protein studies is crucial and highly protein-specific, often determined through trial and error, despite some general considerations. Detergents can be categorized into three major types based on their headgroup charge and polarity: ionic, non-ionic, and zwitterionic. Ionic detergents, such as sodium dodecyl sulfate (SDS), are considered “harsh” as they effectively solubilize membrane proteins but can also disrupt protein hydrophobic interactions that are essential in maintaining protein fold, leading to protein unfolding and denaturation. Non-ionic detergents, such as Triton X-100, n-Decyl-beta-Maltoside (DM), n-Dodecyl β-d-maltoside (DDM), lauryl maltose neopentyl glycol (LMNG), Digitonin, polyoxyethylene sorbitol ester (Tween), and n-Octyl-β-d-Glucopyranoside (OG), are considered as “mild” detergents since they primarily affect protein-lipid or lipid-lipid interactions. Zwitterionic detergents, such as 3-[(3-Cholamidopropyl)dimethylammonio]-1-propanesulfonate (CHAPS) and 3-[(3-Cholamidopropyl)dimethylammonio]-2-hydroxy-1-propanesulfonate (CHAPSO), are also commonly used surfactants for solubilizing biological

macromolecules¹¹⁴. Once the appropriate detergent is determined for the membrane protein of interest, achieving an optimal concentration is important to maintain protein stability while minimizing the detergent background for high-resolution single-particle cryo-EM data acquisition, and which can be assessed quickly by negative-staining EM¹¹⁵. Although detergent micelles can keep membrane proteins soluble in aqueous solutions, the micellar environment is not considered ideal for membrane protein structural biology. This is because the composition of micelles differs significantly from physiological native membranes, often affecting both the structure and function of membrane proteins.

Amphipols are a family of amphipathic polymers that can solubilize membrane proteins by wrapping around the hydrophobic region of the protein, similar to detergent micelles. They significantly improve the stability of membrane proteins in general, making them suitable for a wide range of biophysical studies. Amphipols offer a detergent-free environment, which can be advantageous for studying membrane proteins. However, it is important to acknowledge that while amphipols provide an alternative to detergents, they differ from lipid bilayers and native membranes in terms of their structural properties^{116, 117}.

To study membrane proteins in a lipid environment, several technologies have been developed, such as lipid nanodiscs¹¹⁸, saposin-lipoprotein (salipro)¹¹⁹, and styrene-maleic acid co-polymer lipid particles (SMALPS)¹²⁰, as membrane mimetic systems (**Figure 1.9**)¹⁰¹. Lipid nanodiscs and salipro enable the reconstitution of membrane proteins in a lipid environment that is stabilized by membrane scaffold proteins^{121, 122}. Styrene-maleic acid (SMA) copolymers, these amphipathic molecules are able to destabilize lipid bilayers to the form of lipid discs bounded by the polymer, and membrane proteins can be directly solubilized in a patch of their native membrane in the polymer-bounded nanodiscs¹²³. When visualizing integral membrane proteins in detergents or amphipols, important information regarding lipid interactions and their effects on protein structure is lost. This is particularly relevant for proteins in which lipids play both structural and regulatory roles. For instance, the cryo-EM structure of TRPV1 (transient receptor potential cation channel subfamily V member 1) in lipid nanodisc revealed insights into ligand and regulatory lipid mechanisms¹²⁴. Also, this $\sim 3\text{-\AA}$ density maps obtained with nanodiscs exhibited superior quality compared to cryo-EM structures of TRPV1 in amphipols^{125, 126}, showing better side-chain densities within transmembrane regions and connecting loops that interact with lipids.

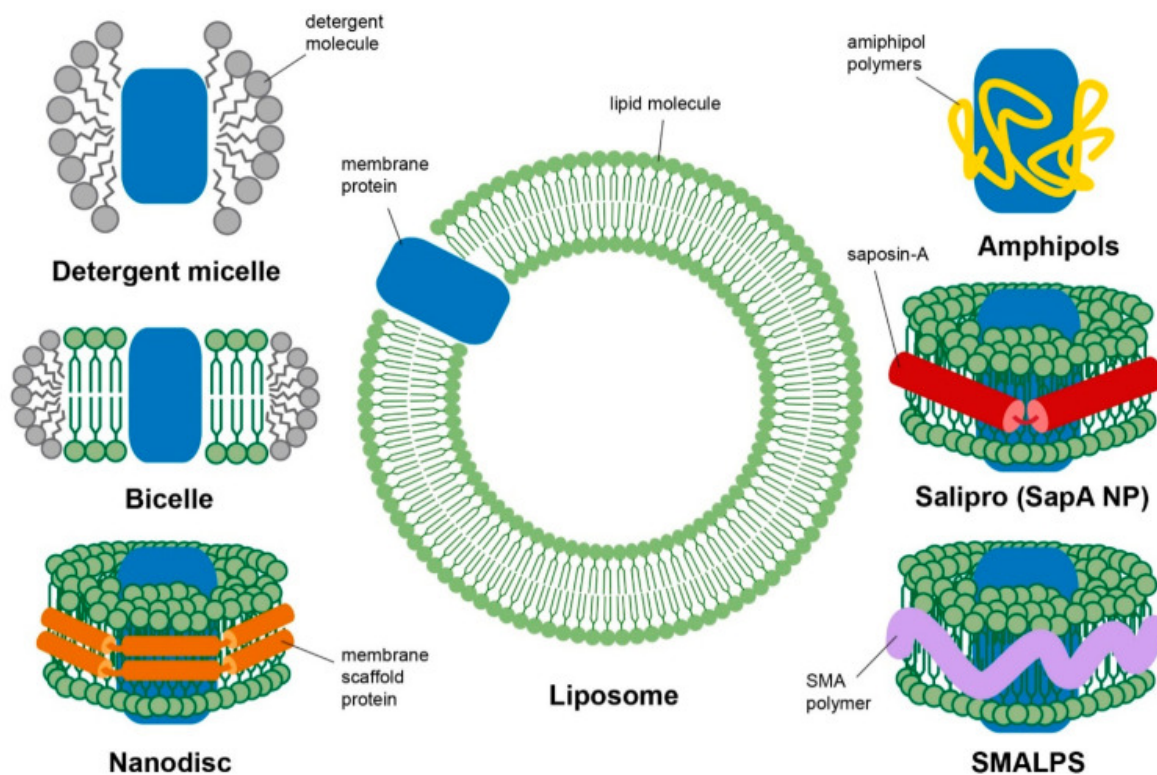


Figure 1.9 Scheme of different membrane mimetic systems. Detergent micelle, amphipols, bicelle, nanodisc, salipro, SMALPS, and liposome. Membrane protein is represented as a blue cartoon block. Image from¹⁰¹.

A drawback of the membrane-mimetic systems discussed above is the absence of an actual lipid bilayer environment. Such an environment is essential for the structure, function and stability of membrane proteins¹²⁷. To address this issue, membrane proteins can be reconstituted into liposomes, and this closed membrane environment closely mimics the physiological conditions of the proteins¹²⁸. Reconstitution into liposomes offers the opportunity to systematically investigate membrane proteins in their functional states and capture specific structural conformations close to their native environments using cryo-EM¹²⁹. This approach involves membrane proteins, which can be produced recombinantly or extracted from native membranes. These proteins are then purified using detergent carriers and subsequently reconstituted into liposomes in preparation for cryo-EM studies. Notably, high-resolution cryo-EM structures of individual detergent-solubilized ryanodine receptor 1 (RyR1) channels have been resolved at resolutions of 3.5-6 Å, revealing insights into the gating and activation mechanisms¹³⁰⁻¹³³. A 6.1-Å structure of RyR1 in the closed state and an 8.5-Å structure of RyR1 in the open state, which showed a conformational switch mechanism of RyR1 channel, and in the both cases RyR1 was reconstituted into lipid nanodiscs, providing a

lipid environment that is critical for the structural integrity of ion channels¹³⁴. More recently, structures of the RyR1 channel in the primed and open states were resolved in liposomes at resolutions of 3.4 and 4.0 Å, respectively. The liposome system not only offers a near-to-native lipid environment but also allows for the creation of asymmetric environments, such as that of the sarcoplasmic reticulum (SR), where calcium concentrations differ significantly between the lumen (millimolar concentration) and the cytosol (nanomolar concentration)¹³⁵.

A recently described method involves the structure determination of membrane proteins within cell-derived membrane vesicles. This innovative approach allows for the structural analysis of membrane proteins without disrupting weakly interacting proteins, lipids, and cofactors that are essential for biological function. A notable example is the determination of Slo1 ion channel structures in enriched Slo1-containing vesicles derived directly from cells at a resolution of approximately 3.5 Å using single-particle cryo-EM, serving as a proof-of-concept for the structure determination of membrane proteins with a less disruptive approach¹³⁶. The use of liposomes or cell-derived vesicles for structure determination is expected to significantly expand in the *in vitro* study of membrane proteins and membrane-associated proteins, particularly for capturing transient complexes in specific functional states. This advancement promises to provide more detailed insights into molecular mechanisms and enhance our understanding of these proteins.

1.3.2 Membrane protein structures *in situ*

Resolving the structures of membrane proteins in their native cellular context is considered the ideal approach for understanding their functions and associated molecular networks. While single-particle cryo-EM can achieve higher resolution than subtomogram averaging (StA), it often requires at least partial purification of the target molecules from their native environment inside cells and tissues. By combining averaging tools on subvolumes obtained through cryo-electron tomography (cryo-ET), structures can currently be determined at resolutions of 10-30 Å¹³⁷. These maps can then be fitted with high-resolution structures obtained using other techniques, such as SPA, to create detailed models of structures and complexes as they occur in cells.

Recent examples of such studies include the visualization of a mitochondrial ATP synthase dimer at a resolution of ~30 Å¹³⁸, a conserved arrangement of complex I/III supercomplexes in the mitochondrial respiratory chain at ~25 Å resolution¹³⁹, and a bacterial type VI secretion

system membrane complex at 17 Å resolution¹⁴⁰. Moreover, subnanometer-resolution structures of membrane proteins *in situ* can provide more detailed insights. For example, a 9-Å structure of the light-dependent protochlorophyllide oxidoreductase (LPOR) in etioplasts showed a novel membrane-associated structural model¹⁴¹, and a 12.6-Å structure of RyR1 in native membranes was determined¹⁴², which was further improved to 9.1 Å with better-resolved secondary structures using a hybrid StA-SPA method¹⁴³. These studies highlight the potential of *in situ* cryo-EM in elucidating the mechanisms and cellular functions of membrane proteins.

Cryo-ET and StA have gained widespread recognition as powerful tools for determining the structures of macromolecules and membrane proteins within cells in recent years. In spite of remaining some challenges in the current cryo-ET workflow, like low throughput in sample preparation, slow data acquisition speeds, difficulties in target identification, and limited usability of image processing software, several proof-of-concept strategies have emerged to address these issues, as discussed in earlier sections. With ongoing advancements and refinements in cryo-ET methodologies, routine high-resolution structure determination *in situ* is poised to become a valuable tool for both structural and cell biologists in the long run, and the field holds great promise for further expanding our understanding of cellular structures and processes at the molecular level.

1.4 Aims of the thesis

The main aim of this thesis is to further our knowledge about the structure and function of membrane protein in lipid bilayer vesicles and membrane-associated protein complexes in their native environment. The research focuses on two specific targets: a small prokaryotic voltage-gated sodium ion channel, NaChBac, and a large knob complex found on the surface of *Plasmodium falciparum*-infected human erythrocyte.

In order to gain a deeper understanding of the functions of membrane proteins, it is crucial to create an environment that mimics their physiological conditions, such as liposomes. The structures of these proteins embedded in liposomes can be determined using cryo-EM, enabling us to investigate their mechanisms in specific states. There have been several structures of voltage-gated sodium ion channels (VGSCs) determined in the past decades. However, current structures of VGSCs under such conditions are expected in a membrane at 0 mV, and chemical cross links, mutations, and toxins have been used to capture or stabilize voltage sensors in conformations thought to mimic the resting condition. Chapter 2 of this study aims to explore the structure of NaChBac, a VGSC, embedded in liposomes under the resting membrane potential. By introducing a transmembrane electrochemical gradient into proteoliposomes, cryo-ET and StA techniques are employed to analyze the structure of NaChBac. This structure is then compared to the single particle cryo-EM structure (EMD-21425) of NaChBac in nanodiscs, which lacks the membrane potential¹⁴⁴. This comparison can provide insights into the conformational changes and functional implications of NaChBac under the influence of the resting membrane potential.

Malaria remains a major and growing threat to public health and economic development of countries in the tropical and subtropical regions of the world to date. *Plasmodium falciparum*, the human malaria parasite, infects red blood cells (RBCs) and induces the formation of numerous small membrane protrusions that render their initially smooth surface bumpy. These changes on the surface of RBCs result in sequestration of parasitized erythrocytes in the microvasculature and lead to severe disease. For each protrusion, termed as a knob, is a major pathophysiological determinant in *P. falciparum* infections. While a previous study provided an overall architectural view of knobs using negative stain tomography¹⁴⁵, there is a need for a higher-resolution cryo-EM structure *in situ* to investigate the knob complex scaffold and the

connections between knob complex and erythrocyte membrane in details. Chapter 3 of this thesis attempts to bridge this gap by imaging knob complex to visualize its structure and dynamics. This research can provide an insight that can guide future studies, shedding light on the molecular composition and functional role of these native knobs in *Plasmodium* infection and immunity.

General conclusions and outlook are presented and described in Chapter 4.

Chapter 2

Determining the structure of the bacterial voltage-gated sodium channel NaChBac embedded in liposomes by cryo-ET and StA

2.1 Introduction

2.1.1 Conformational cycle of a voltage-gated sodium channel (VGSC)

Biological membranes provide physical barriers in cells and organelles, and allow the maintenance of electrochemical gradients that are essential to triggering various membrane proteins for physiologically critical functions^{1, 2}. Voltage-gated ion channels (VGICs) are a class of transmembrane proteins that are selectively permeable to ions, such as Na⁺, K⁺, Ca²⁺, and Cl⁻ when they are activated and undergo conformational changes due to changes in membrane potential around the channels¹⁴⁶. In neuronal signaling and muscular contraction, Na⁺ influx through voltage-gated sodium channels (VGSCs, Na_v) corresponds to the rapid rising phase of the action potential in the membranes of neurons and other electrically excitable cells^{147, 148}. VGSCs undergo a series of conformational changes between open, closed, and inactivated states during a cycle of an action potential (**Figure 2.1**)¹⁴⁹⁻¹⁵¹. Each action potential is followed by a refractory period, during which the VGSCs enter an inactivated state while the Na⁺ and K⁺ ions return to their resting state distributions across the membrane, yielding a resting membrane potential of approximately -70 mV in most neurons. Under the resting potential, VGSCs transition back to their resting state in which they remain until the next action potential.

tarantula toxin and voltage-shifting mutations were designed for trapping the resting state of a Na_v1.7 chimera¹⁶⁰. The structures of the potassium channels Eag and KCNQ1 under membrane potential have recently been reported, describing conformational changes in the voltage-sensing domain and the interplay between the channel and lipids^{161, 162}.

Despite the great progress made for the potassium channels, a structure of a VGSC under a physiological resting membrane potential to provide support for the classical “sliding helix” model for gating from the resting state to the activated state still remains missing¹⁵⁹. In particular, for small VGSCs, such as the 120-kDa NaChBac, structural analysis in unrestricted membranes in presence of the electrochemical gradients is still challenging.

2.1.2 Membrane potential measurements in proteoliposomes using fluorescent indicators

Proteoliposomes, which are lipid vesicles containing reconstituted membrane proteins, provide an excellent experimental system for functional and structural studies of membrane proteins under conditions that mimic those *in vivo*¹²⁹. Proteoliposomes allow preservation of the functional lipid environment, generation of transmembrane ionic gradients or pH gradients and do not restrict the motion of transmembrane helices in the membrane plane. This approach typically includes a series of steps, including the generation of a lipid film, extrusion of the lipid film, destabilization of liposome with detergents, incubation of membrane proteins with detergent-destabilized liposomes, and subsequent removal of the detergent¹⁶³.

The transmembrane potential depends on the ion concentrations on either side of the membrane. The membrane potential can be estimated by using the Nernst equation

$$V_{Eq.} = \frac{RT}{zF} \ln \left(\frac{[X]_{out}}{[X]_{in}} \right)$$

where the $V_{Eq.}$ is the equilibrium potential (Nernst potential) for a given ion. R is the universal gas constant. T is the temperature in Kelvin. z is the valence of the ionic species. F is Faraday's constant. $[X]_{out}$ and $[X]_{in}$ are the concentration of the ionic species X in the extracellular and the intracellular fluid, respectively. The presence of ion-selective conductance should lead to Nernst potentials which can be assayed using potential-sensitive probes, such as JC-1^{164, 165}.

JC-1 is a fluorescent indicator commonly used in cellular biology to monitor changes in membrane potential. It is a carbocyanine dye with a delocalized positive charge that forms a concentration-dependent fluorescence consisting of J-aggregates. When excited at 490 nm, the JC-1 monomers emit fluorescence at 527 nm, and J-aggregates emit at 590 nm. Increasing concentrations of JC-1 above a certain concentration result in a linear rise in the J-aggregate fluorescence, while the monomer fluorescence remains constant. For example, in energized mitochondria with a negative membrane potential interior, JC-1 is taken up into the matrix, leading to the formation of J-aggregates¹⁶⁶, which can be assayed for mitochondria function.

Valinomycin, a highly potassium-selective ionophore, is a naturally cyclic peptide used in the transport of potassium and as an antibiotic¹⁶⁷. The presence of valinomycin renders proteoliposomes selectively permeable to potassium ions, resulting in the establishment of a transmembrane electrical potential. This potential can be monitored by measuring the formation of J-aggregates of JC-1 using a spectroscopic assay. This fluorescence emitted by the J-aggregates is pH independent within the physiological pH range of 7.15-8.0 and can be linearly calibrated with valinomycin-induced K^+ diffusion potentials. Despite extensive functional characterizations using proteoliposomes, successful attempts to employ this system for structural elucidation of membrane proteins are still limited and require further exploration.

2.1.3 Membrane protein structures embedded in liposomes

Structures of several membrane proteins, such as hBK channel^{168, 169}, AcrB transporter¹⁷⁰, Eag potassium channel¹⁶¹, KCNQ1 potassium channel¹⁶², PIEZO1 channel¹⁷¹, and ryanodine receptor 1 (RyR1)¹³⁵ in liposomes have been determined by single particle cryo-EM at resolutions ranging from 3.4 to 7 Å. However, without a significantly large soluble domain, it may be challenging to “identify” fully transmembrane proteins in electron micrographs for further alignment and averaging¹⁷⁰. Indeed, the molecular weights of these proteins for which structures were solved from proteoliposomes are relatively high: KCNQ1 channel is ~240 kDa, AcrB transporter is ~350 kDa, Eag channel is ~390 kDa, hBK channel is ~500 kDa, Piezo1 channel is ~860 kDa, and RyR1 is ~2.2 MDa, and they have substantial extramembranous domains.

Cryo-ET and StA techniques have also been employed for determining structures of membrane proteins in proteoliposomes: structures of the small membrane protein MspA (~160 kDa) and the serotonin receptor ion channel 5-HT₃R (~275 kDa) were determined at resolutions of ~17

and ~ 12 Å, respectively in 2012 and 2015^{172, 173}. Later, a structure of a large ion channel RyR1 was reported *in situ* first at 12.6 Å resolution and then at subnanometer resolution of 9.1 Å allowing to resolve alpha helices^{142, 143}. While the structure resolution achieved by StA is generally lower compared to single particle reconstructions, it still demonstrates the potential to determine structures of smaller membrane proteins in lipid vesicles as a technique.

2.1.4 Aim

To date, structures of VGSCs have been determined in crystals, detergent micelles, or nanodiscs. Various approaches, such as chemical cross-linking, mutations, and toxins have been employed to stabilize voltage sensors in conformations that mimic the resting state of VGSCs in cells. The concern remains that the changes observed may not accurately represent the behavior of the channels in their native membrane, as they lack a voltage difference across membranes. Studying NaChBac gating mechanisms in a membrane environment is therefore of great interest.

This chapter aims to obtain structural and dynamic information on NaChBac in liposomes, and on how the channel is influenced by a physiological resting membrane potential. However, NaChBac is a small (~ 120 kDa) membrane protein without a significantly large soluble domain, making it challenging to accurately identify fully transmembrane proteins in electron micrographs for alignment and averaging. With recent advancements in cryo-ET and StA, the techniques might be able to target smaller membrane proteins in proteoliposomes, as tomograms contain the third dimension compared to 2D imaging in single particle cryo-EM.

To this end, the experimental process involves the purification of NaChBac, reconstitution of the protein into liposomes, establishment of a transmembrane potential in the proteoliposomes, optimization of cryo-grid preparation, processing of cryo-ET data, and structural analysis by subtomogram averaging (StA) (**Figure 2.2**).

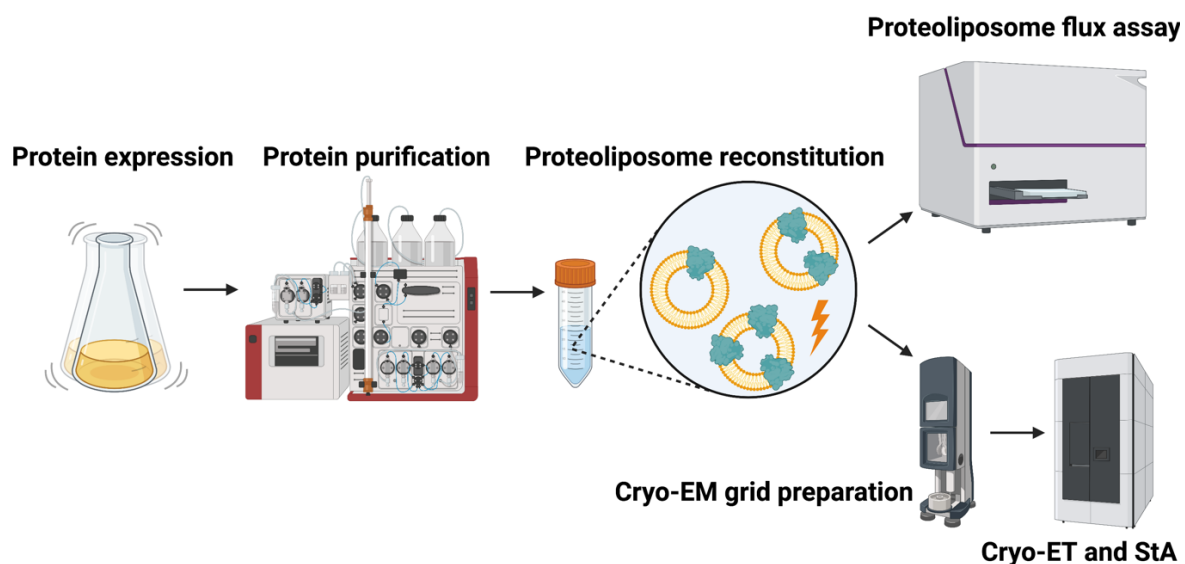


Figure 2.2 Graphic workflow of Chapter 2. The experimental workflow involves the expression and purification of NaChBac, NaChBac reconstitution into liposomes, measurement of membrane potential in proteoliposomes, cryo-EM grid preparation and optimization, cryo-ET data collection, image processing, and StA.

2.2 Materials and methods

2.2.1 Materials, instrumentation, and programs

2.2.1.1 Materials

Bio-Beads SM-2 resin (Bio-Rad)

Chloroform (Carl Roth)

DDM, n-dodecyl β -d-maltoside (Anatrace)

Fiducial gold 10 nm (Cell Microscopy Core, University Medical Center Utrecht)

HEPES, N-2-Hydroxyethylpiperazine-N'-2-ethane sulphonic acid (Carl Roth)

Imidazole (Carl Roth)

IPTG, Isopropyl- β -D-thiogalacto-pyranoside (Carl Roth)

JC-1, 5P,5P,6,6P-tetrachloro-1,1,3,3P-tetraethylbenzimidazolylcarbocyanine iodide (Invitrogen)

PageRuler™ Prestained Protein Ladder (Thermo Fisher Scientific)

E. coli Polar Lipid Extract (Avanti Polar Lipids)

Potassium chloride (Carl Roth)

Slide-A-Lyzer MINI dialysis devices (Thermo Fisher Scientific)

Sodium chloride (Carl Roth)

Sucrose (Carl Roth)
Tris (Carl Roth)
Uranyl acetate (Carl Roth)
Valinomycin (Invitrogen)
Whatman® No. 1 filter paper (Whatman)
Whatman® No. 4 filter paper (Whatman)

2.2.1.2 Instrumentation

Biochemical, cellular, and optical instruments

Biocomp gradient master (ScienceServices)
BioPhotometer (OD 600) (Eppendorf)
ChemiDoc MP Imaging System (Bio-Rad)
Fluorescence spectrophotometer, F-4500 (Hitachi)
High-pressure homogenizer, CF1 (Constant Systems)
Mini Extruder (Avanti Polar Lipids)
Mini Gel Tank, SDS-PAGE (Invitrogen)
Nanodrop one (Thermo Fisher Scientific)
Shake incubator, New Brunswick™ Innova® 44 (Eppendorf)
Thermomixer Comfort (Eppendorf)
Ultrasonic bath, SONOREX (BANDELIN)

Centrifuges and rotors

Avanti J-20 XP centrifuge (Beckman Coulter)
JLA-8.100 Fixed-angle rotor (Beckman Coulter)
JA-20 Fixed-angle rotor (Beckman Coulter)
MiniSpin Centrifuge (Eppendorf)
Optima MAX-TL ultracentrifuge (Beckman Coulter)
Optima XE ultracentrifuge (Beckman Coulter)
SW 40 Ti Swinging-bucket rotor (Beckman Coulter)
TLA-100 Fixed-angle rotor (Beckman Coulter)
Type 45 Ti Fixed-angle rotor (Beckman Coulter)

Fast protein liquid chromatography (FPLC) system and columns

ÄKTA pure™ chromatography system (Cytiva)

Nickel-charged IMAC resin (Cytiva)

Superose 6 Increase 10/300 GL (GE Healthcare)

Microscopes and others

Glacios cryo-TEM (Thermo Fisher Scientific)

Tecnai Spirit BioTwin (Thermo Fisher Scientific)

Titan Krios G2 cryo-TEM (Thermo Fisher Scientific)

Titan Krios G3i cryo-TEM (Thermo Fisher Scientific)

Falcon 3 direct electron detector (Thermo Fisher Scientific)

K3 direct electron detector with BioQuantum imaging filter (Gatan)

Glow discharge cleaning system, easiGlow™ (PELCO)

Vitrobot Mark IV (Thermo Fisher Scientific)

2.2.1.3 Programs

crYOLO

CryoSPARC v4.1.2

Dynamo 1.1.532

EPU 3

Gctf 1.06

IMOD 4.11

MATLAB 2023

MotionCor2 1.6.3

RELION-3.1

RELION-4.0-beta

SerialEM 4.0

tomoBEAR v0.1

Topaz v0.2.5

The illustrations in this chapter were created with BioRender.com.

2.2.2 Methods

2.2.2.1 Expression and purification of NaChBac

The full-length NaChBac cDNA was cloned into pET21a with an amino terminal His₆-GFP^{A206K} fusion protein (**Appendix A.1**). Overexpression in *E. coli* C41(DE3) cells was induced with 0.25 mM IPTG (final concentration) at 22 °C when the OD₆₀₀ reached 0.8 to 1.0 (**Appendix A.2 and A.3**).

Cells were harvested after 20-h incubation at 22 °C, and cell pellets were resuspended in a buffer containing 25 mM Tris, pH 8.5, and 300 mM NaCl. The cells were disrupted by high-pressure homogenization, and insoluble fractions were removed by centrifugation at 30,000 × g for 30 minutes. The supernatant was subjected to ultracentrifugation at 150,000 × g for 2 hours. The membrane-containing pellets were resuspended in an extraction buffer containing 25 mM Tris, pH 8.5, 300 mM NaCl, 20 mM imidazole, and 1% (wt/vol) DDM, incubated at 4 °C for 2 hours, and subsequently centrifuged at 30,000 × g for 30 minutes. The supernatant was applied to Ni-NTA resin, and washed with 20 column volumes of wash buffer containing 25 mM Tris, pH 8.5, 300 mM NaCl, 20-80 mM imidazole, and 0.1% DDM. Target proteins were eluted with 3 column volumes of elution buffer containing 25 mM Tris, pH 8.5, 300 mM NaCl, 250 mM imidazole, and 0.1% DDM. After concentration, proteins were further purified by size exclusion chromatography (Superose 6 Increase column) in a running buffer containing 25 mM Tris, pH 8.5, 150 mM KCl, and 0.1% DDM (**Appendix A.4 and A.5**).

2.2.2.2 NaChBac reconstitution into liposomes

The protocol for proteoliposome reconstitution was carried out as described before¹⁶³, with minor modifications. *E. coli* Polar Lipid Extract dissolved in 400 µL chloroform at a concentration of 25 mg/mL was dried to form a thin film under a gentle stream of nitrogen and resuspended in 1 mL of reconstitution buffer containing 25 mM HEPES, pH 7.5, and 150 mM KCl. After water-bath sonication for 5 minutes, the lipid solution was frozen with liquid nitrogen and thawed in water bath for 10 cycles, and the lipid solution was subject to repeated extrusion through 100 nm filters. To destabilize the liposomes prior to protein reconstitution, they were incubated with 2% (wt/vol) DDM as a final concentration at 25 °C for 2 hours. Subsequently, purified NaChBac was added to the detergent-destabilized liposomes at a lipid-to-protein ratio of 2:1 (wt/wt). After incubation at 4 °C for 1 hour, the lipid-protein-detergent mixture was loaded into a dialysis bag, and dialyzed against the reconstitution buffer at 4 °C for approximately one week with gentle rotation. Following dialysis, Bio-Beads SM-2 resin¹⁷⁴

0.4 g was added to the sample to remove residual detergents from the proteoliposomes. After incubation at 4 °C overnight, Bio-beads were removed through filtration, and the proteoliposomes were ready for liposome flux assays.

2.2.2.3 Density gradient centrifugation

Sucrose gradients were prepared in SW 40 Ti ultracentrifuge tubes on a Biocomp Gradient Master based on the method of Coombs and Watts¹⁷⁵. A concentrated sucrose solution (25 mM HEPES, pH 7.5, 150 mM KCl, and 1 M sucrose) was layered under an equal volume of light solution (25 mM HEPES, pH 7.5, 150 mM KCl, and 0.3 M sucrose) in centrifuge tubes. The tubes were closed with caps to expel all air, and the gradient (10-30%) was formed by rotation. Before adding the samples, a 400 μ L volume was removed from the top of each tube, and then a 400 μ L liposome sample with or without protein was loaded into each tube and centrifuged at $130,000 \times g$ for 18 hours at 4 °C. After ultracentrifugation, opaque liposome bands were collected with a syringe and diluted with reconstitution buffer to remove most of the sucrose. The liposomes were pelleted by centrifugation at $90,000 \times g$ for 1 hour at 4 °C and resuspended in the reconstitution buffer, and samples were identified by SDS-PAGE.

2.2.2.4 Negative-staining EM

Proteoliposome samples were diluted in a buffer containing 25 mM HEPES, pH 7.5, and 150 mM KCl to a series concentration. The sample was applied to freshly glow-discharged carbon-coated grids, rinsed with several drops of the dilution buffer, and stained with 1% uranyl acetate or uranyl formate. Images were recorded at a magnification of $49,000 \times$ with defocus values ranging from -2.5 to -3.5 μ m, resulting in a pixel size of 2.26 Å/pixel with Spirit Biotwin. As most of the protein was inserted with GFP located in the liposome lumen, it was not possible to screen protein insertion with negative-staining EM.

2.2.2.5 Proteoliposome flux assay

The proteoliposome, prepared in a solution of 150 mM KCl, were diluted 100-fold into a 3 mM KCl solution (25 mM HEPES, pH 7.5, and 3 mM KCl) containing 1 μ M of JC-1 dye. Once the JC-1 fluorescence reached a stable baseline, valinomycin was added to the system at a final concentration of 1 μ M. The fluorescence signal of the J-aggregates ($\lambda_{ex} = 480$ nm, $\lambda_{em} = 595$ nm) was monitored upon the addition of valinomycin, which initiated K^+ efflux from all the proteoliposomes until the external K^+ concentration was increased by the addition of 2.5 M

KCl solution. The obtained data were normalized and averaged across three independent measurements. The mean values along with the corresponding standard errors are reported.

2.2.2.6 Preparation of proteoliposomes with polarized membranes for cryo-EM

The proteoliposomes prepared earlier were diluted into 3 mM KCl solution (25 mM HEPES, pH 7.5, and 3 mM KCl) containing 10-nm gold fiducial markers, and 1 μ M valinomycin was added followed by a 5-minute incubation on ice. A 2 μ L aliquot of the polarized proteoliposome solution was applied onto a glow-discharged holey gold grid (Quantifoil Au R2/2, 400 mesh). The use of gold specimen support has been shown to effectively reduce radiation-induced motion and improve image quality during data acquisition^{176, 177}. After incubating the sample on the grid for 3 minutes at 10 °C with a humidity of 100%, excess solution was manually blotted from the side the grid using a Whatman® No. 4 filter paper. Another 2 μ L of the polarized proteoliposome solution was applied to the same grid for 15 seconds, and then the grid was blotted with a Whatman® No. 1 filter paper and plunge-frozen in liquid ethane to preserve the sample in a vitrified ice.

2.2.2.7 Single-particle data acquisition and data processing

A total number of 7,652 raw movie stacks were automatically recorded by EPU software (Thermo Fisher Scientific) on a 300 kV Cs-corrected Titan Krios G3i cryo-TEM equipped with a BioQuantum imaging filter at 20 eV slit width and a K3 direct electron detector. The acquisition areas were selected based on the liposome distribution pattern. Raw movies were collected at a nominal magnification of 105,000 \times in counting mode (spot size 5, C2 aperture 70 μ m) resulting in a pixel size of 0.837 Å, with a defocus range of -2 to -3.5 μ m. The dose rate on the camera was set to be \sim 14 counts per physical pixel per second. The total exposure time was set to 2.5 s with 0.05 s per frame to generate 50-frame gain normalized tiff stacks. The total dose for a stack was 50 e⁻/Å².

Movie stacks were drift corrected using CryoSPARC¹⁷⁸. Contrast transfer function (CTF) information was estimated from nondose weighted images by Patch-based CTF estimation in CryoSPARC. Particles were picked by CryoSPARC auto-picking from three different strategies: 1) blob picker, 2) Topaz picker¹⁷⁹, and 3) template-based picker with projections from a 3D reference EMD-21425. After particle extraction, multiple rounds of 2D classification were performed.

2.2.2.8 Cryo-ET data collection, image processing, and subtomogram averaging

Imaging was performed on a Titan Krios G2 cryo-TEM with a K3 direct electron detector and a BioQuantum imaging filter slit width of 20 eV operated by SerialEM software¹⁸⁰. Tomographic series were acquired using a dose-symmetric scheme¹⁸¹, with tilt range $\pm 45^\circ$, 3° angular increment, and defoci between -2.5 and -3.5 μm . The acquisition magnification was 81,000 \times , resulting in a calibrated pixel size of 1.39 \AA . The electron dose for each untilted image was increased to $\sim 20 \text{ e}^-/\text{\AA}^2$, and tilt images were recorded as 10-frame movies in counting mode, with a total dose per tilt series of around 130 $\text{e}^-/\text{\AA}^2$.

Data processing was performed using early versions of tomoBEAR¹⁸², implemented as a set of MATLAB scripts. Frames were aligned and motion-corrected using MotionCor2¹⁸³. Tilt series were aligned using 10-nm gold fiducial markers by IMOD^{184, 185}. Contrast transfer function (CTF) estimation was performed using defocus values measured by Gctf¹⁸⁶ for each projection. A total of 98 tomograms and the four binned reconstructions were generated from CTF-corrected and aligned stacks using weighted back projection in IMOD.

Subtomogram positions ($\sim 86,000$) were generously picked manually from 4-times binned tomograms, and extracted with a box size of 128 cubic voxels from 2-times binned tomograms using the Dynamo Catalogue system¹⁸⁷. Initial alignment was performed manually on ~ 200 particles, and the center of four GFPs and the direction of the central axis based on the membrane were defined using *dynamo_gallery* after which the roughly aligned particles were summed up low-pass-filtered to 40 \AA . This volume was used as an initial reference for the global alignment of all subtomograms, resulting in all particles aligned to the same Z height in 3D. Several rounds of initial classification by multireference alignment were performed to remove junk particles, with the first step 360° in-plane search (XY plane) being performed on all particles in C1, and a large soft-edged sphere mask was applied for the particle cleaning. Further multireference alignment and averaging with a soft-edged ellipsoid alignment mask was applied throughout and the averaging results showed a prominent tetrameric feature between the lipid bilayer in C1. In total, $\sim 25,500$ particles from good class averages were then subjected to the RELION-4.0¹⁸⁸ for further 3D classification and refinement. Final converged averages were formed by 3,116 particles in C1 at 16.3 \AA resolution, and a smaller sphere mask was applied to improve the resolution. No symmetry was applied during processing.

2.3 Results

2.3.1 Sample preparation

2.3.1.1 Protein expression and purification

After protein overexpression, His₆-GFP^{A206K}-NaChBac from *Escherichia coli* C41(DE3) cells was purified using a two-step purification approach of affinity and size-exclusion chromatography (SEC). The cells were harvested after overnight culture, and the cell pellets were resuspended in a detergent-free buffer and disrupted by high-pressure homogenization. Insoluble fractions were removed by centrifugation, and the resulting supernatant was subjected to ultracentrifugation to obtain membrane-containing pellets. NaChBac was extracted from the membrane-containing pellets using a buffer containing DDM. The extracted sample was then applied to Ni-NTA resin, and the target protein was washed and eluted with a buffer containing an imidazole gradient (**Figure 2.3 A**). Eluted proteins were further purified with Superose 6 Increase column in a SEC buffer, resulting a monodisperse peak (**Figure 2.3 B**). The final yield of purified NaChBac was 1.6 ± 0.3 mg/L cell culture. The purity of His₆-GFP^{A206K}-NaChBac monomer (55 kDa) was assessed by SDS-PAGE analysis (**Figure 2.3 C**).

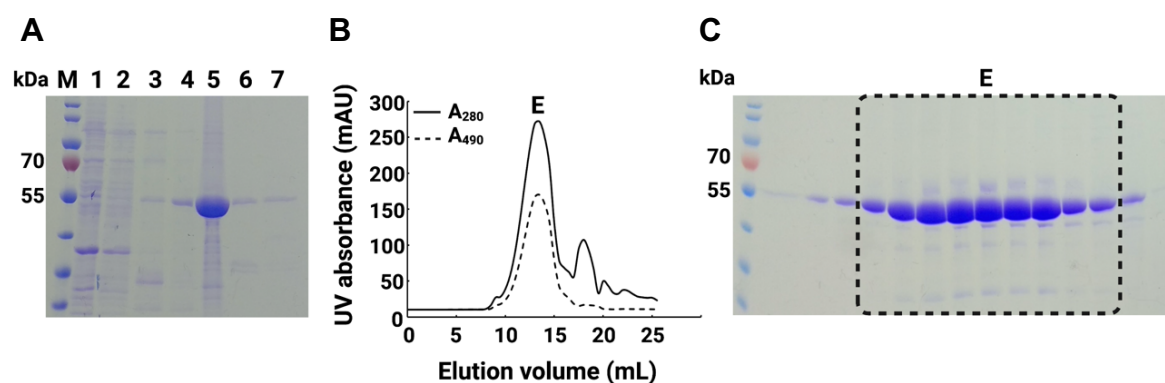


Figure 2.3 Purification of NaChBac. (A) SDS-PAGE of protein purification with Ni-NTA column. M, protein Ladder, lane 1, flow-through, lane 2, wash with 20 mM imidazole buffer, lane 3, wash with 50 mM imidazole buffer, lane 4, wash with 80 mM imidazole buffer, lane 5-6, elution with 250 mM imidazole buffer, lane 7, elution with 500 mM imidazole buffer. (B) SEC profile, a monodisperse peak of His₆-GFP^{A206K}-NaChBac tetramer (220 kDa) identified as E. (C) SDS-PAGE of protein purification with SEC. E, elution.

2.3.1.2 Proteoliposome reconstitution

Next, NaChBac was reconstituted into liposomes using *E. coli* polar lipid extract to mimic the native bacterial membrane environment. In order to maximize the number of particles per proteoliposome and thus the efficiency of cryo-ET data collection, a systematic optimization of lipid compositions, lipid-to-protein ratios, and detergent removal rate was necessary.

A simple approach involving ultracentrifugation and SDS-PAGE analysis could quickly provide a rough idea of how much protein was successfully reconstituted into liposomes (**Figure 2.4 A**). A comparison between NaChBac reconstituted in phospholipids POPE:POPG (3:1) liposomes and *E. coli* polar lipid liposomes revealed a higher supernatant-to-pellet ratio in the latter case, indicating a more efficient reconstitution and a higher presence of functional proteins after reconstitution (**Figure 2.4 B**). This can be attributed to the similarity between *E. coli* polar lipid composition and the native lipid environment of bacterial NaChBac.

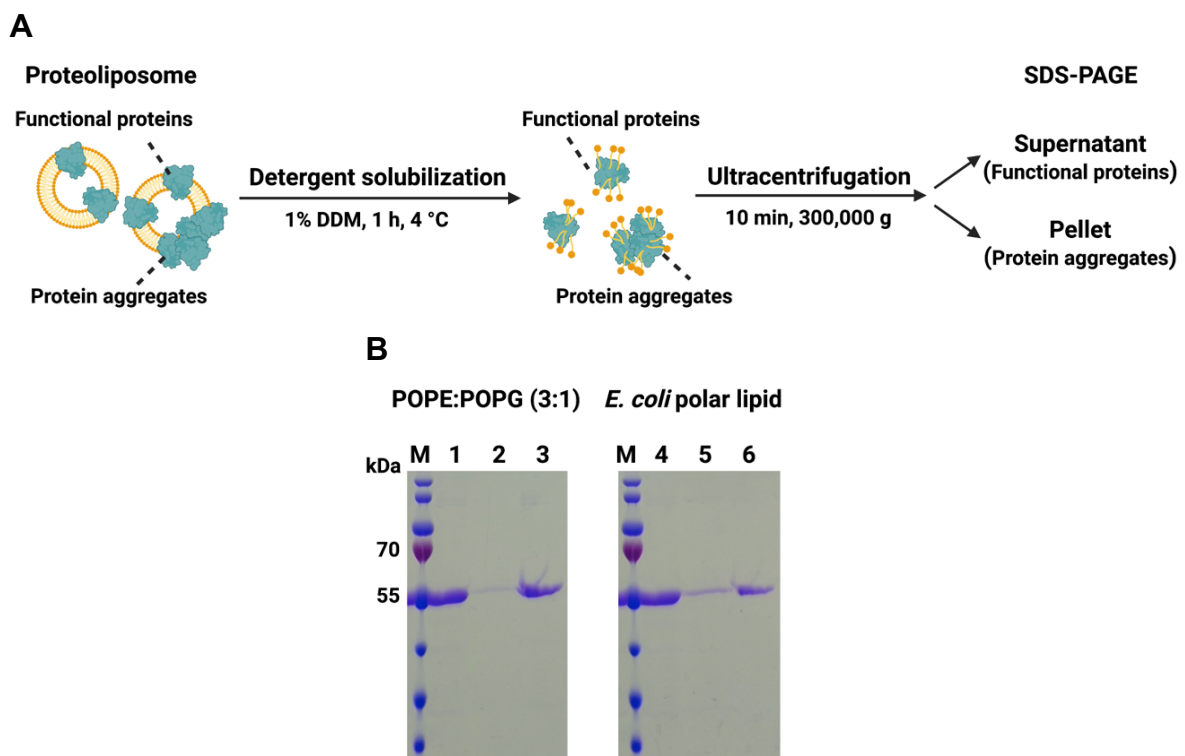


Figure 2.4 Reconstitution efficiency of NaChBac in proteoliposomes. (A) The reconstitution efficiency can be assayed using ultracentrifugation and SDS-PAGE analysis. (B) A comparison of the supernatant-to-pellet ratio between POPE:POPG (3:1) and *E. coli* polar lipid as lipid sources is shown. M, protein Ladder, lane 1 and 4, samples before detergent solubilization, lane 2 and 5, supernatant, lane 3 and 6, pellet.

During the screening of lipid-to-protein ratios (LPRs, weight to weight) for proteoliposome reconstitution, LPR10, LPR5, LPR2, and LPR1 were evaluated using gradient ultracentrifugation. The results showed a significant protein band shift in each proteoliposome sample compared to empty liposomes (ELS) (**Figure 2.5 A**). However, the LPR1 proteoliposomes exhibited heavy aggregation at the bottom of the sucrose gradient (not shown here), therefore a relatively low LPR of 2:1 (mol ratio = 27350:1) was decided for the reconstitution conditions.

In the final step of reconstitution, the detergent DDM was removed by dialysis, followed by incubation with Bio-beads. Due to the very low critical micelle concentration (CMC) of DDM, a relatively long time for the dialysis (around one week) and subsequent incubation with Bio-Beads were necessary, otherwise the resulting proteoliposomes showed the membrane with a “fluid edge” (**Figure 2.5 B and C**). SDS-PAGE analysis confirmed that the his-tagged GFP^{A206K}-NaChBac showed no signs of contamination or protein degradation after this long proteoliposome preparation procedure (**Figure 2.5 D**).

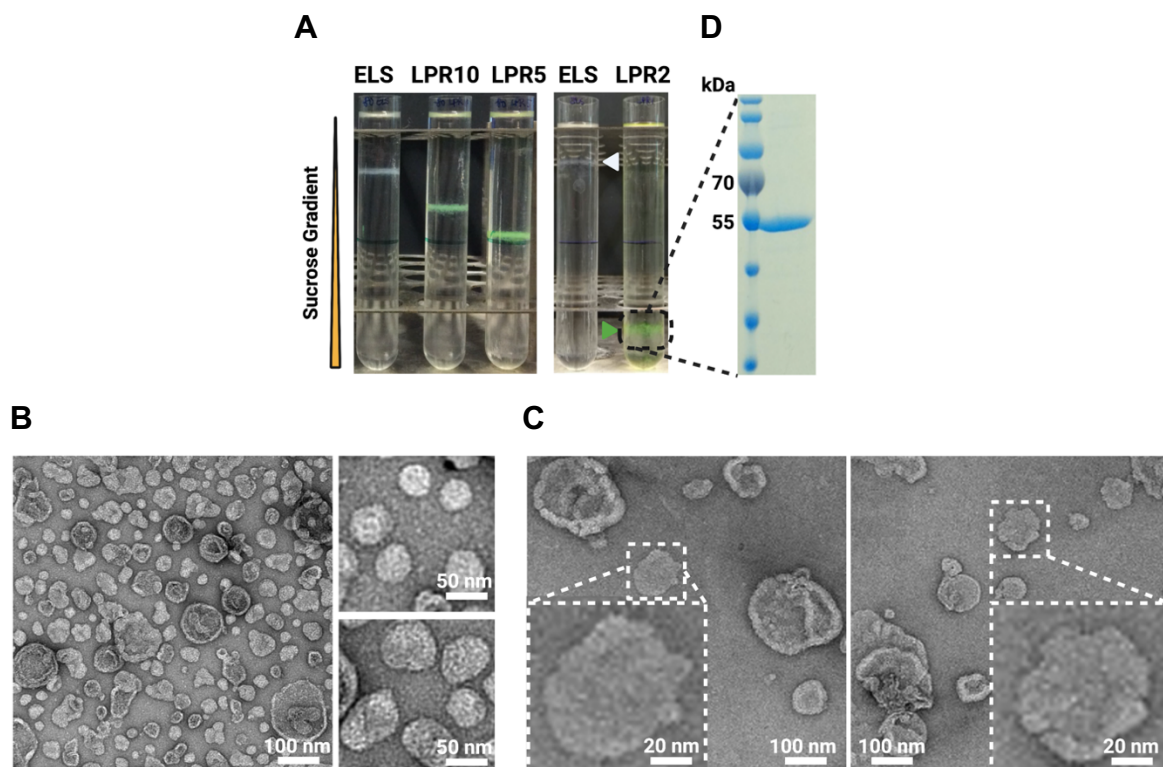


Figure 2.5 Optimization of proteoliposome reconstitution. (A) Sucrose gradient ultracentrifugation showed a significant band shift between empty liposomes (ELS) and each proteoliposome sample with different LPRs. The white triangle indicates the band of ELS,

while the green triangle indicates the band of proteoliposomes with LPR2. (B) A negative-staining image of proteoliposomes with detergent removal entirely. The insets showed proteoliposomes with “sharp edge” features. (C) Negative-staining images of proteoliposomes with residual detergent during dialysis. The insets showed proteoliposomes with “fluid edge” features. (D) The protein showed no degradation on the SDS-PAGE after proteoliposome reconstitution.

Interestingly, I observed that reducing the rate of detergent removal improved the reconstitution efficiency, resulting in more protein copies per proteoliposome and reduced proteoliposome aggregation, as observed by cryo-EM imaging (**Figure 2.6**). In short, the efficiency of membrane protein incorporation in liposomes depends on a variety of factors such as lipid composition, detergent type and concentration, lipid-to-protein ratios, detergent removal rate, and the nature of membrane proteins.

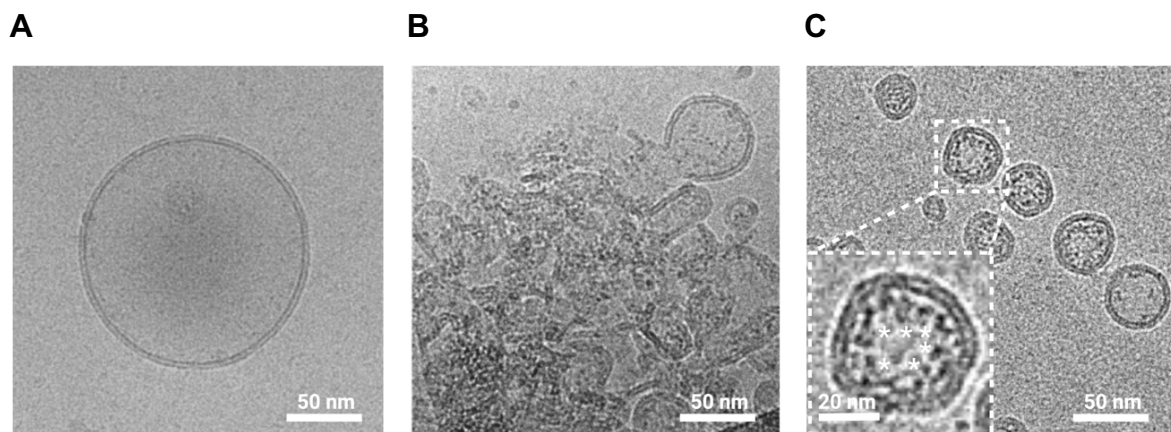


Figure 2.6 Cryo-images during optimization of NaChBac proteoliposome reconstitution. (A) A representative image of an ELS. (B) A representative image of proteoliposome aggregation. (C) A representative image of proteoliposomes. The inset highlighted a proteoliposome with proteinaceous densities. White asterisks indicate distinct non-membrane densities.

2.3.1.3 Preparation of proteoliposomes with polarized membranes

In order to establish a membrane potential, a well-established protocol with minor modifications was employed¹⁶⁸. Proteoliposomes prepared with a buffer containing a high concentration of KCl were resuspended into a buffer with a low KCl concentration, followed by addition of a potassium ionophore valinomycin. The membrane potential across the

NaChBac-containing proteoliposome bilayer was assayed using the voltage-sensitive cationic fluorescent dye JC-1^{164, 166} (**Figure 2.7 A**). Proteoliposomes were prepared in a buffer with 150 mM KCl and were resuspended into 3 mM KCl buffer in the presence of 1 μ M valinomycin (DMSO as a control experiment), resulting in a membrane potential of -100 mV at room temperature (298 K) as estimated using the Nernst equation for the calculation of the potassium diffusion potential¹⁶⁵. Measuring the fluorescence over time showed stable levels of membrane potential over tens to thousands of seconds. Increasing the external concentration of KCl led to a decrease in JC-1 fluorescence due to a reduced negative membrane potential, thus indicating the K⁺-selective permeability and the stability of proteoliposomes (**Figure 2.7 B and C**). These polarized proteoliposomes, mimicking conditions of the native negative resting membrane potential (-100 mV), were immediately subjected to a holey gold grid and frozen for structural analysis by cryo-EM.

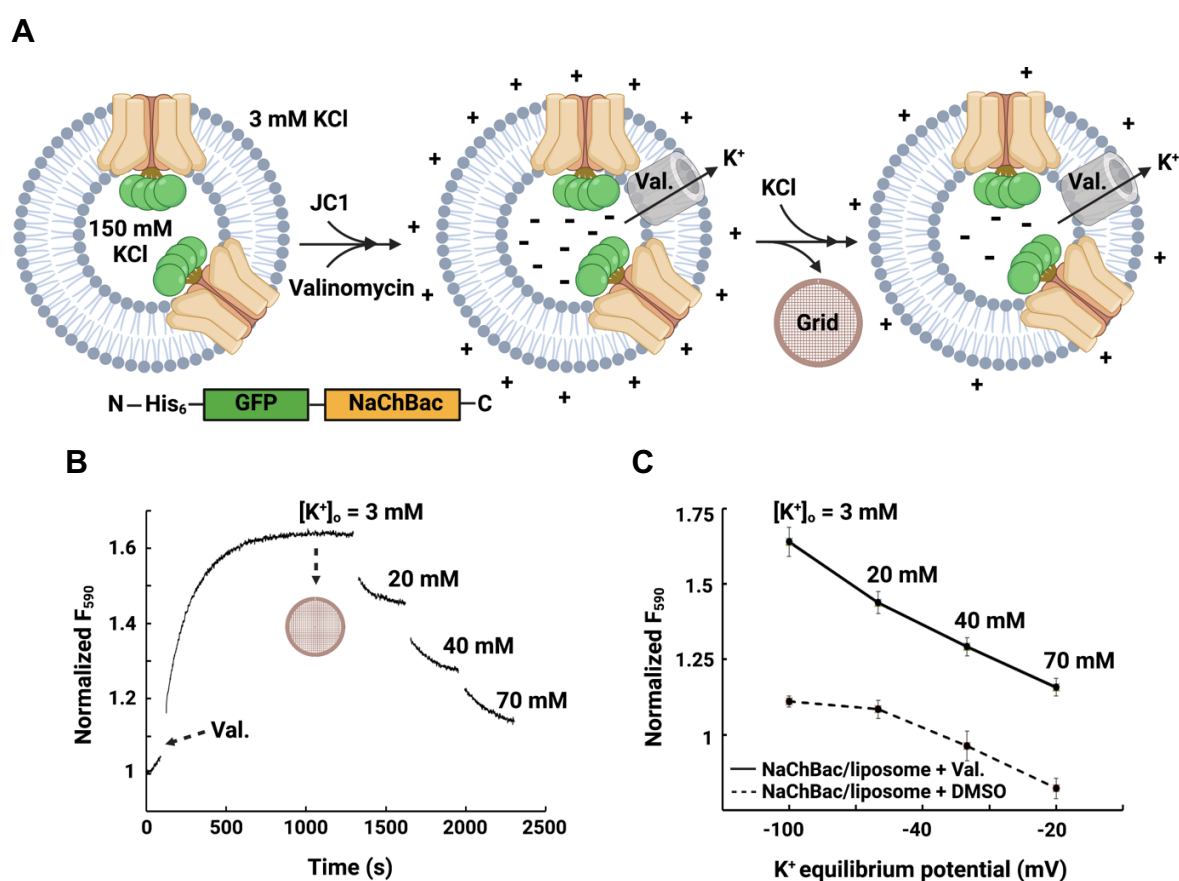


Figure 2.7 Preparation of polarized NaChBac-containing liposomes. (A) A schematic of the protocol used to obtain polarized proteoliposomes for cryo-EM analysis. Proteoliposomes loaded with 150 mM KCl were resuspended into 3 mM KCl buffer, and valinomycin was added to mediate potassium flux. Potassium efflux through valinomycin generated a negative

potential inside of the proteoliposomes with respect to the outside, and the red fluorescence of JC-1 aggregates was measured. (B) Fluorescence-based liposome flux assay of proteoliposome membrane potential. Addition of valinomycin allowed potassium efflux, and a subsequent decrease in fluorescence as external KCl concentration was increased, indicating K⁺-selective permeability and the stability of proteoliposomes. Proteoliposomes were then frozen on gold-supported gold grids for structure determination while $[K^+]_{out} = 3 \text{ mM}$, $[K^+]_{in} = 150 \text{ mM}$, yielding a membrane potential ($V_{Eq.}$) of -100 mV at room temperature (298 K). (C) Normalized fluorescence showed the difference between proteoliposomes in the presence of 1 μM valinomycin and DMSO (control), indicating potassium equilibrium potential was triggered by valinomycin. Error bars indicated s.e.m. (n = 3-5).

2.3.1.4 Cryo-EM grid preparation

Proteoliposomes were screened by negative-staining EM and cryo-EM, showing a large population of proteoliposomes with a diameter of up to 150 nm (**Figure 2.5 B and 2.6 C**). While some proteoliposomes were much larger, the smaller ones were more amenable to producing thin ice for single-particle cryo-EM and cryo-ET imaging. The initial cryo-EM preparations showed a significant clustering of proteoliposomes near the edges of the grid holes with empty hole centers (**Figure 2.8 A**). This was a major challenge in characterizing liposomes using cryo-EM, as achieving a high number of liposomes in the holes of holey TEM grids was difficult. Thus, optimization of cryo-EM grids was essential. In order to produce a uniform sample distribution, a multi-sample application method was performed on gold-supported gold grids inspired by previous reports^{189, 190}, tuning the parameters of the sample preparation robot, resulting in the final sample for cryo-EM (**Figure 2.8 B and C**).

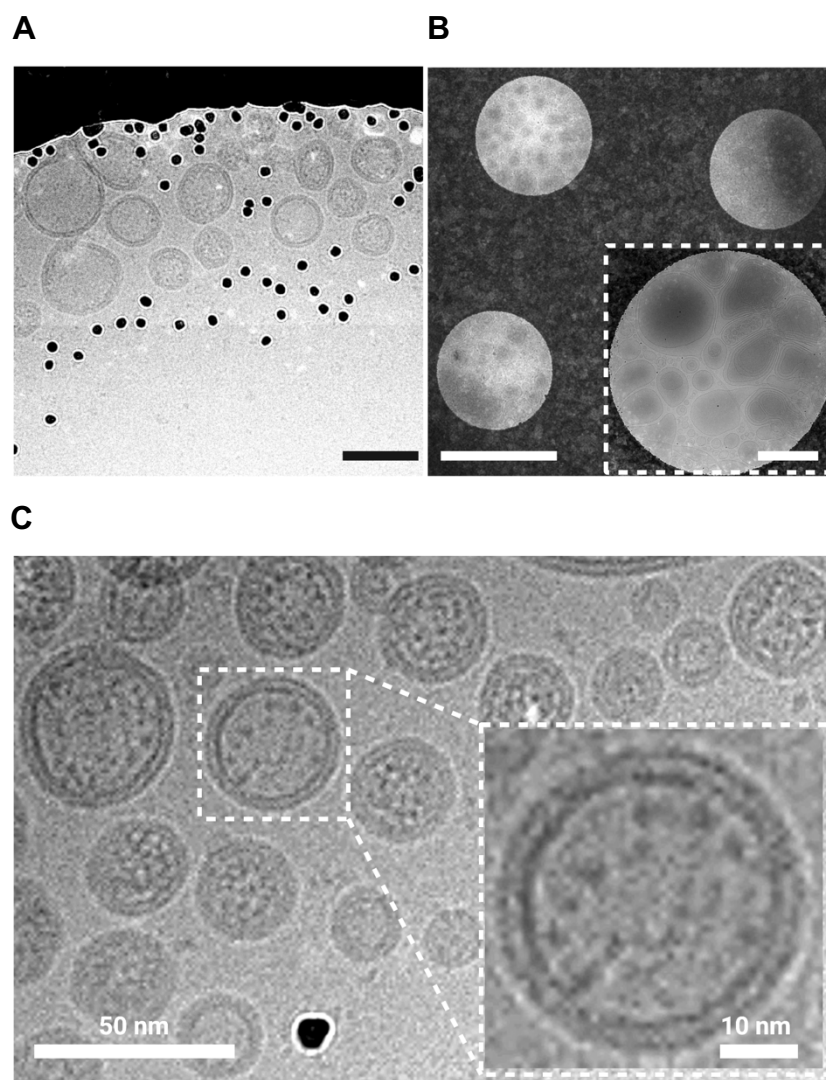


Figure 2.8 Optimization of cryo-EM grid preparation. (A) Cryo-EM micrograph of proteoliposomes on holey gold grids, where the proteoliposomes preferred to attach to the support film instead of entering the holes. Scale bar: 100 nm (B) Low- and intermediate- (the inset, scale bar: 500 nm) magnification cryo-EM images after the optimization, showing that the hole areas were saturated by liposomes. Scale bar: 2 μm (C) A cryo-image of proteoliposomes, which showed the success of the multi-sample application method in increasing the density of liposomes in holes, allowing for cryo-EM data acquisition in the thin ice over the hole areas. The inset showed a proteoliposome with proteinaceous densities.

2.3.2 Single-particle cryo-EM of NaChBac proteoliposomes

While the previous report¹⁷⁰ has discussed that signals from the soluble domain of embedded membrane proteins was essential in particle selection from 2D micrographs. Without a distinctively sized soluble domain, it would be impractical to select the transmembrane domain

of membrane proteins from the membrane. In the study of NaChBac proteoliposomes, GFP was fused to the N-terminal end of each of the channel subunits to function as an “anchor” for identifying the channels in the membrane, which may help the particle identification in micrographs. Thus, three different particle picking strategies were compared: blob picker with CryoSPARC as a straightforward particle picking method, Topaz picker as a deep learning-based particle picking method, and template-based picker with CryoSPARC using the structure of NaChBac in nanodiscs as a reference.

By intentionally tuning and reducing the picking threshold to include more potential particles, each strategy yielded a range of 3 to 4 million particles. However, only a small fraction of protein particles were discernible in the micrographs and were selected by these strategies, suggesting a low accuracy of particle picking for per-liposome. Also, a large number of particles were selected from the background area, introducing a high presence of junk particles in the dataset for next 2D classification. Despite this, notable differences were observed among the three strategies. The blob picker method showed rare particles from the side view of membranes (**Figure 2.9 A**), while the Topaz picker method exhibited numerous particles selected from the background (**Figure 2.9 B**). Therefore, the particles picked by the template-based picker method (**Figure 2.9 C**) were processed with 2D classification to exclude junk particles.

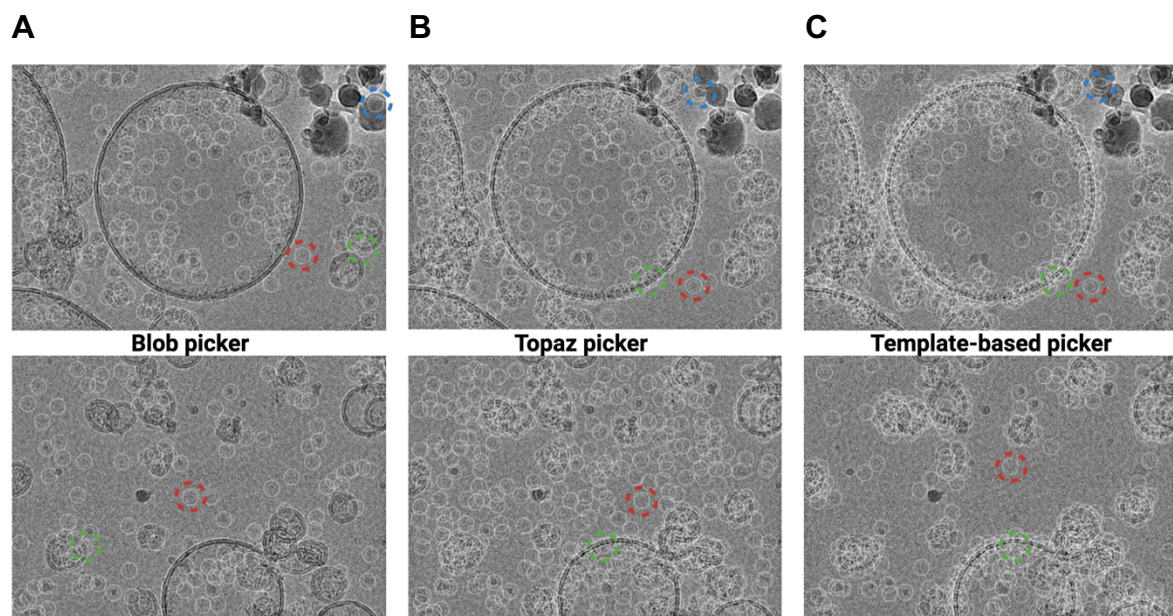


Figure 2.9 Particle auto-picking on micrographs. (A) Particle picking using a blob picker and (B) using a Topaz picker showed low accuracy in particle selection. (C) Template

matching-based picking was performed in CryoSPARC with EMD-21425 as a reference, resulting in a higher number of particles being picked from the liposome regions. Particles were selected on the background (red circles), on membranes (green circles), and on contaminants (blue circles).

A multi-round 2D classification strategy was applied to exclude junk particles, and particles with distinctive structural features, such as the lipid bilayer signal, were successfully isolated. The 2D classification approach was able to separate useful particles from those seemingly “lipid-only” classes. However, the features of the transmembrane domain of NaChBac remained unclear when compared to the features from GFPs, which served as the soluble domain. Moreover, no top-view particles embedded in the liposome were observed in 2D averages even after multiple rounds of 2D classification, leading to a failure in generating a promising 3D initial model (**Figure 2.10**).

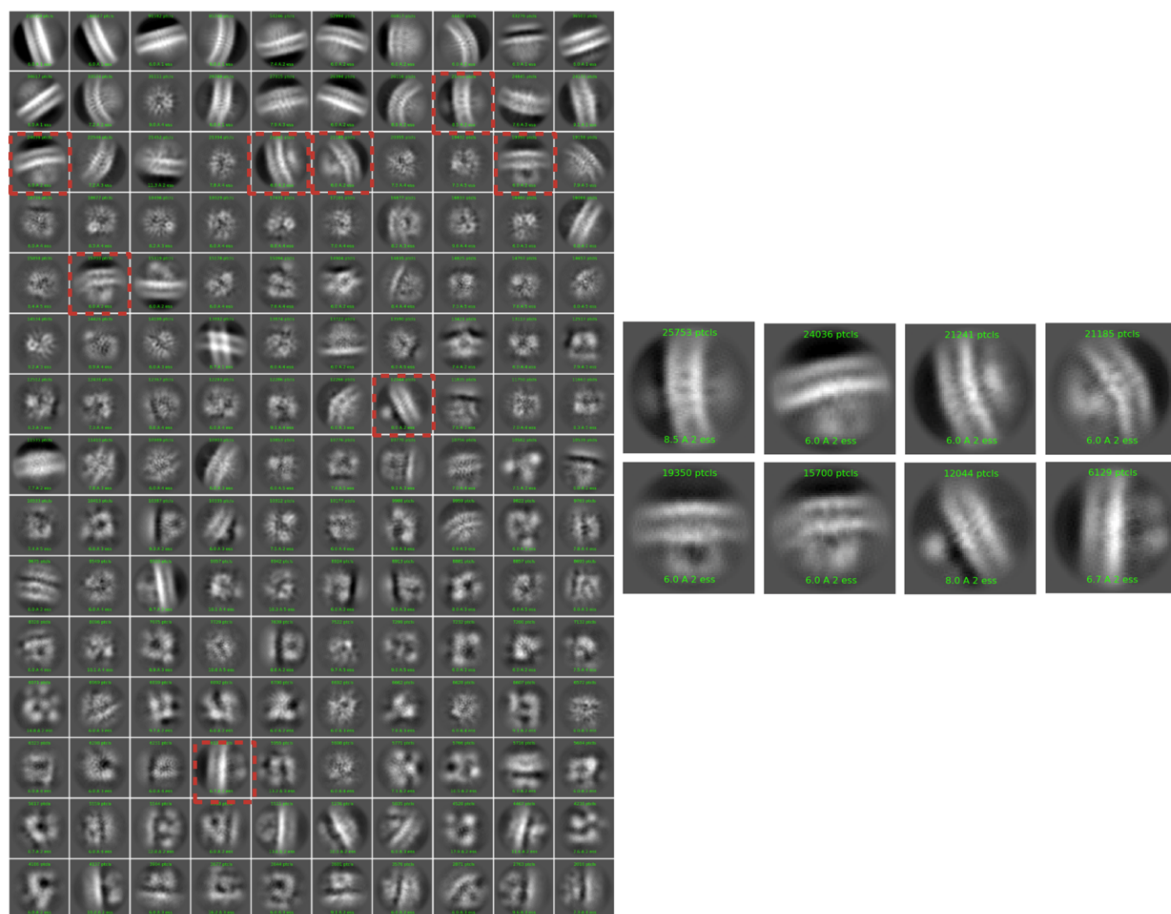


Figure 2.10 2D classification for the selection of good protein particles embedded in liposomes. Good particle classes were indicated by red boxes. The insets revealed that the

selected particles (~145,000) displayed subtle protein features between the lipid bilayer, while displaying clear GFP signals outside the membrane.

2.3.3 Cryo-ET of NaChBac proteoliposomes

I collected 98 tomograms (**Appendix Table B.1**), they were processed using early versions of tomoBEAR, which combined Motioncor2, Gctf, IMOD, and Dynamo. Tomographic reconstructions clearly revealed GFP densities and occasional densities between the membranes. The majority of the particles had the GFP “in the lumen of the proteoliposome”. Knowledge of the orientation of the majority of the channels defined how the voltage was established across the membrane, *i.e.* directed similarly to potential found across the inner membrane of the native bacterium. “Side-views” and tetramer-resembling “top-views” with putative GFP densities positioned closely to the membrane could be observed in tomograms (**Figure 2.11**).

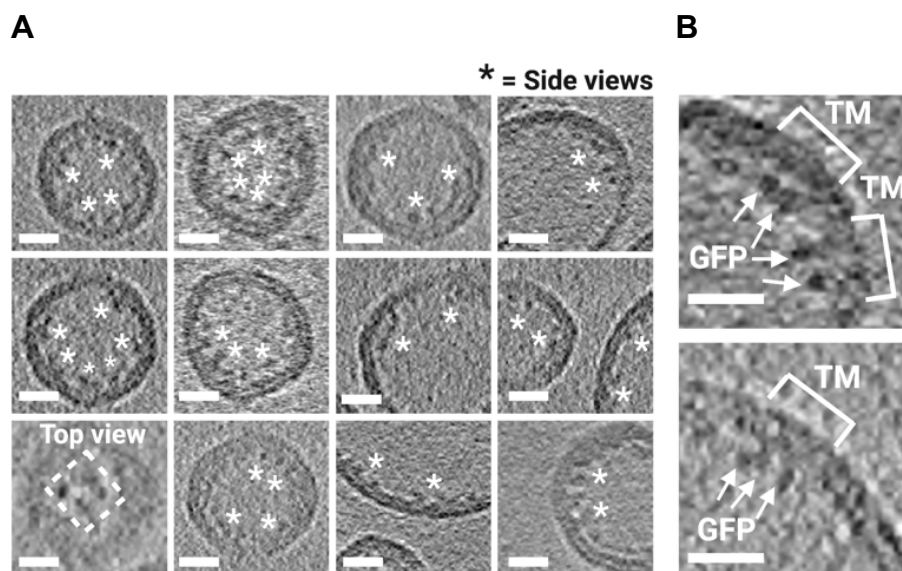


Figure 2.11 Visualization of NaChBac proteoliposomes by cryo-ET. (A) Cryo-ET slices of proteoliposomes showed particle positions and the side view and the top view of his-GFP-NaChBac. White asterisks indicate distinct non-membrane densities. (B) Near-equatorial slices through tomograms of proteoliposomes showed GFPs outside the lipid bilayer in the lumen of the proteoliposomes and the transmembrane domains of NaChBac embedded in the membrane. Scale bars: 10 nm.

Attempts were performed to identify protein particles using template matching with the NaChBac structure in nanodiscs (EMD-21425) as a reference on binned 8 tomograms with or without non-linear anisotropic diffusion. Template matching involves systematically cross-

correlating a template molecule against a tomogram, resulting in a cross-correlation map. Each pixel in this map represents a score assigned to the corresponding pixel in the tomogram map, indicating the similarity of the neighborhood of the tomogram pixel to the template. Although structural features such as the lipid bilayer signal were successfully identified, the identification of protein particles was unsuccessful (**Figure 2.12**).

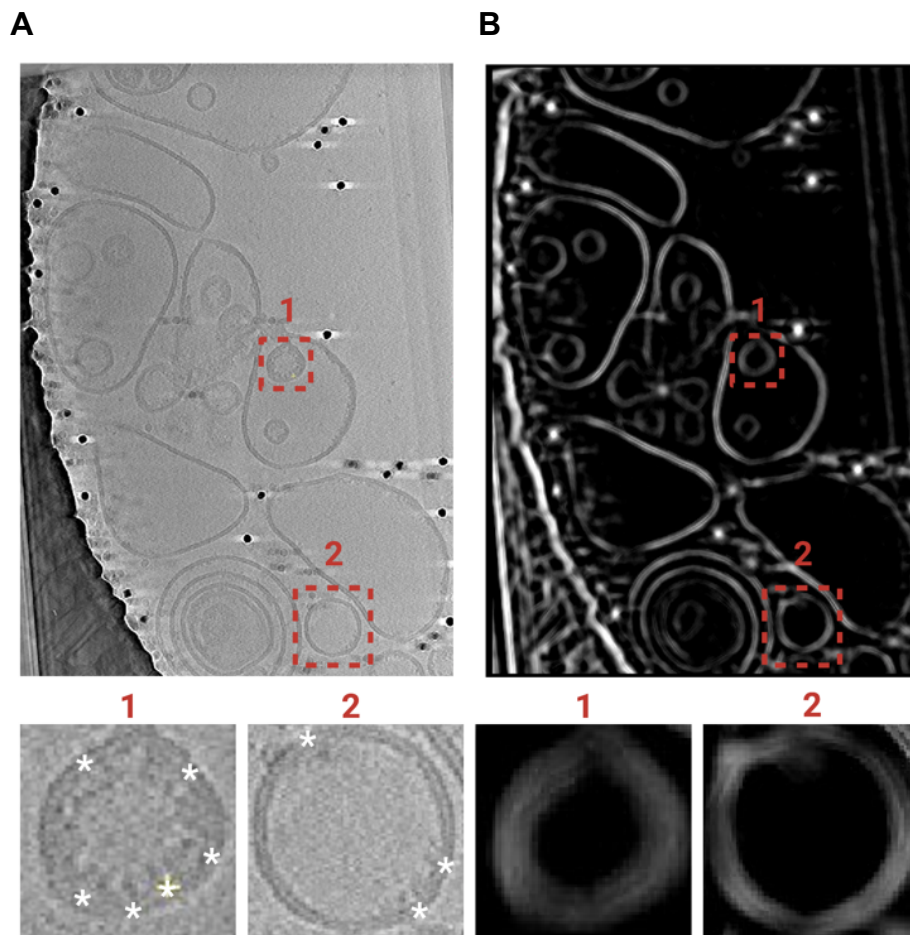


Figure 2.12 Protein identification on NaChBac proteoliposomes by template matching. (A) An example tomogram, and (B) its corresponding cross-correlation map, showed a satisfactory match with the liposomes, but the signals of proteins could not be identified in the cross-correlation map (red boxes).

Additional attempts to parameterize the membranes followed by subtomogram classification of positions in order to separate the protein-containing particles from empty membranes (**Figure 2.13**). Unfortunately, this approach also did not work due to the low protein fraction on the membrane, small size of the protein, and a significant heterogeneity in the curvature of proteoliposomes. Therefore, a manual approach was adopted, where ~86,000 tomographic

positions were picked from the cryo-ET volumes (prioritizing tomograms with thin ice) using the Dynamo catalogue system. This manual selection process provided more accurate protein particle positions in 3D, which were then used for subsequent particle cleaning and classification.

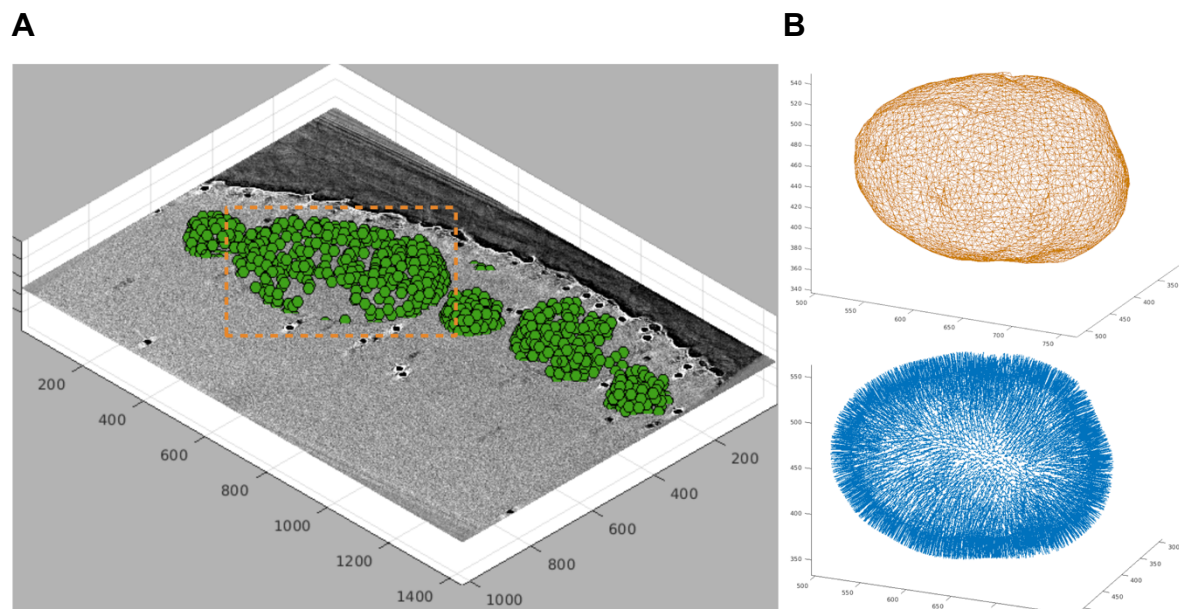


Figure 2.13 Particle extraction from NaChBac proteoliposomes using geometric modelling tools. (A) Geometry-supported particle extraction by “drawing” membranes (green dots). A membrane model in (B) was indicated by a yellow box. (B) Each cross-point on the surface represented the position of a particle for extraction (above). The blue arrows indicated the initial direction of each particle point, showing the direction towards the outside of the membrane surface (below).

2.3.4 Subtomogram averaging of NaChBac proteoliposomes

Subtomogram alignment and classification were performed to clean the particle dataset. First, Dynamo was used to align all the subtomograms to a reference created by manually aligning a small subset of particles and allowing them to rotate 360 degrees around the unit sphere (the first two Euler angles) and applying high rotational symmetry around the vertical axis (without searching the last Euler angle). This resulted in a curved membrane with a defined density at the concave side of the membrane (**Figure 2.14**). The membrane was less ordered at the edges of the box reflecting various sizes of proteoliposomes leading to “averaging out” of the bilayer.

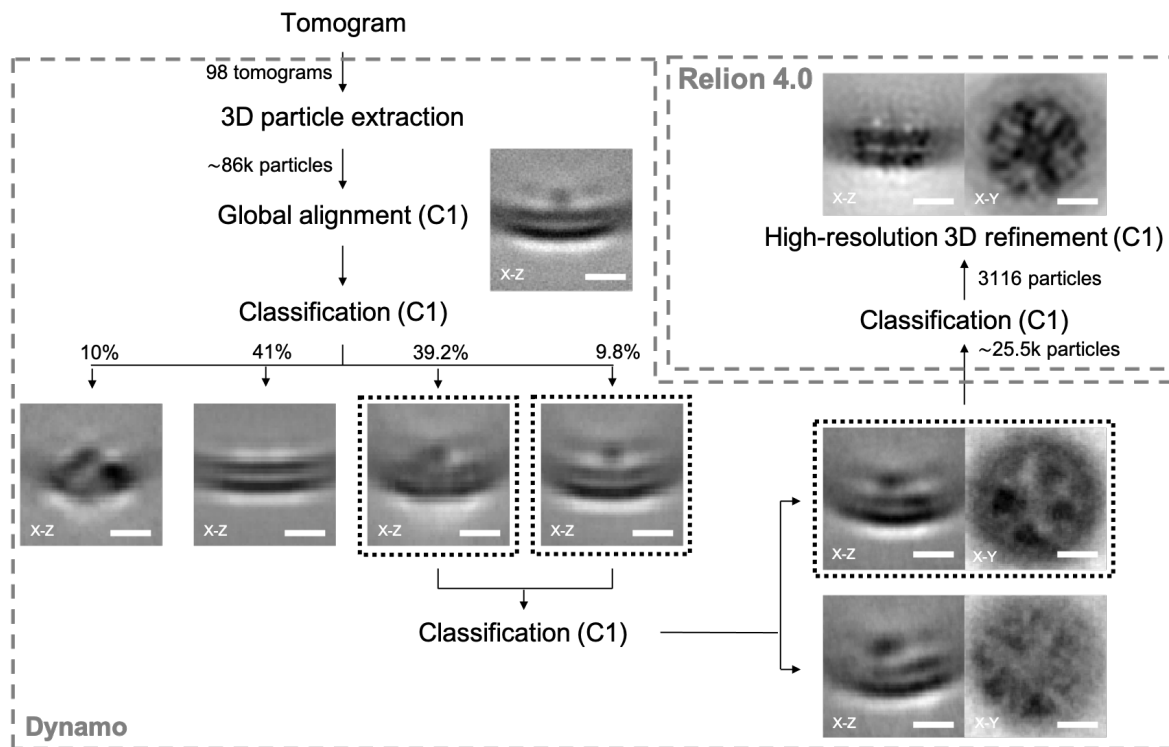


Figure 2.14 A workflow for structural determination of NaChBac embedded in liposomes by StA. Manually identified particles (~86,000) were extracted from 98 tomograms. Following a global alignment of all extracted particles, multiple rounds of classification were applied to isolate classes containing tetrameric features in the top-views. Particles with clear protein signals were then subjected to RELION-4.0 for further classification and refinement. The final subtomogram averaging from 3,116 particles displayed clear domain features of NaChBac (Scale bars: 5 nm.). More detailed information can be found in **Appendix Figure B.1**.

Next, a classification was performed of all the particles into 10 classes, allowing for rotation around the third Euler angle while limiting rotations around the first two. This resulted in several classes resembling tetrameric features containing ~42,100 particles, and the dataset was further cleaned to ~31,800 particles with more classifications. Further classification based on rejecting classes with poorly resolved membranes narrowed down the dataset to ~25,500 particles. This refined particle set showed a tetrameric arrangement of density in the transmembrane domain (**Figure 2.14 and 2.15**). The resulting particle set was subjected to RELION-4.0 for further classification and refinement.

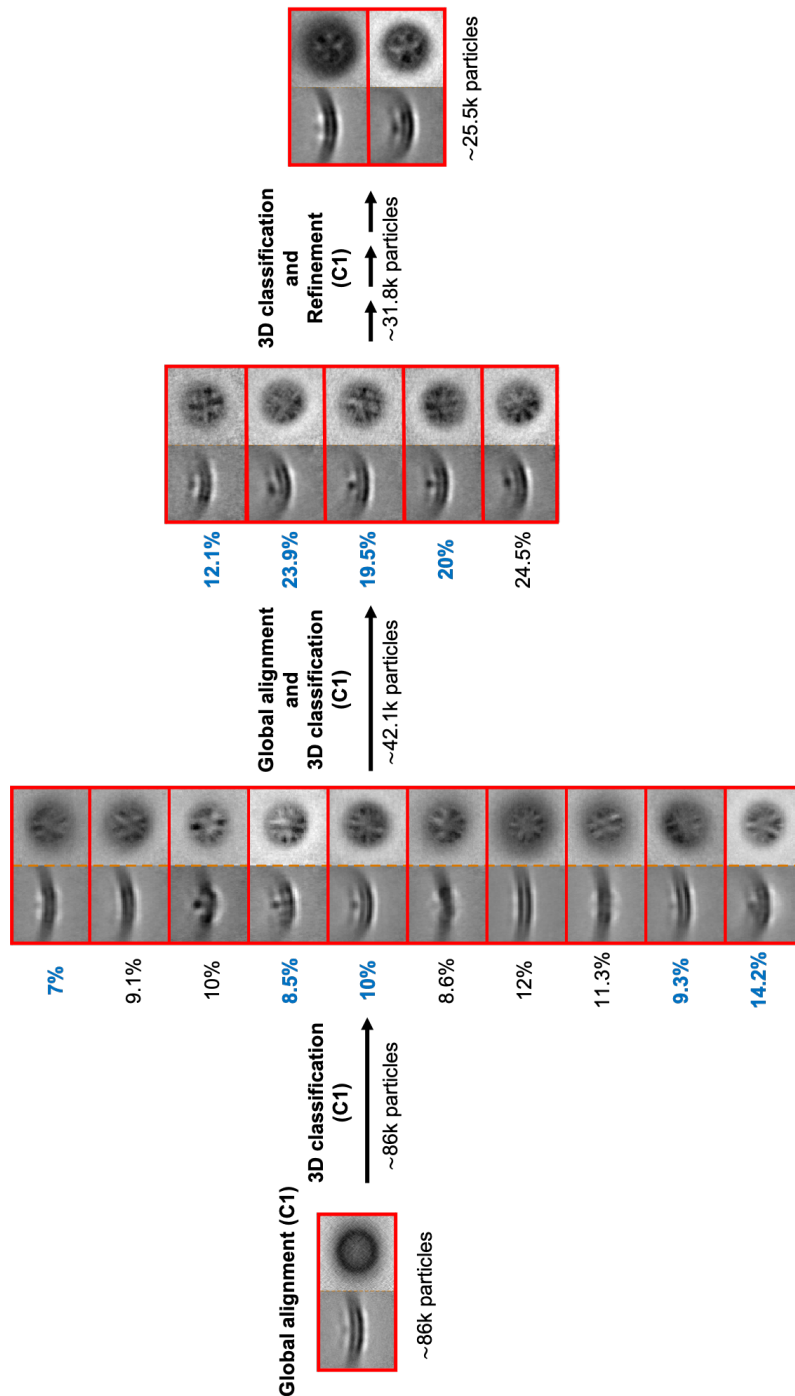


Figure 2.15 An overview of the dataset cleaning process with Dynamo. Central slices through the averages in X-Z and X-Y directions, produced by Dynamo, are shown. First, ~86,000 particles were globally aligned and were implemented to 3D classification for the particle cleaning. ~42,100 particles were selected for further classification. After collecting good particles (~31,800) from the previous steps, multiple rounds of 3D classification and refinement were performed, and ~25,500 particles were selected for additional 3D classification and refinement using RELION-4.0. During the outlined process no symmetry was applied and only tetrameric-looking classes were selected for further processing.

At this stage, significant differences in membrane curvatures were still observed among the classes. Therefore, several rounds of classification were performed, and auto-refine was applied to the resulting datasets with more or fewer particles, and ultimately, a dataset of 3,116 particles yielded a structure with a resolution of 16.3 Å (**Figure 2.16 A**). While the structure appeared overall tetrameric, the symmetry was not perfect, and refinement of the structure with C4 symmetry did not result in a better structure at a promising resolution (**Figure 2.17**). Symmetry expansion also did not help to improve the structure. Comparing the structure to the intermediate class averages (**Figure 2.14**), which could not be auto-refined, revealed heterogeneity in the positioning of the voltage-sensing domains (VSDs) (**Figure 2.15**). Finally, despite multiple attempts with different masks for alignment, the best alignment was achieved when the mask did not accommodate the densities of GFP. This suggests that the densities of GFP, located on a 15-long residue linker, while useful for the localization of the 120-kDa predominantly transmembrane protein NaChBac in tomograms and helpful for the initial alignment, were flexible and did not help to the alignment of particles during the final refinement (**Figure 2.16 B and C**).

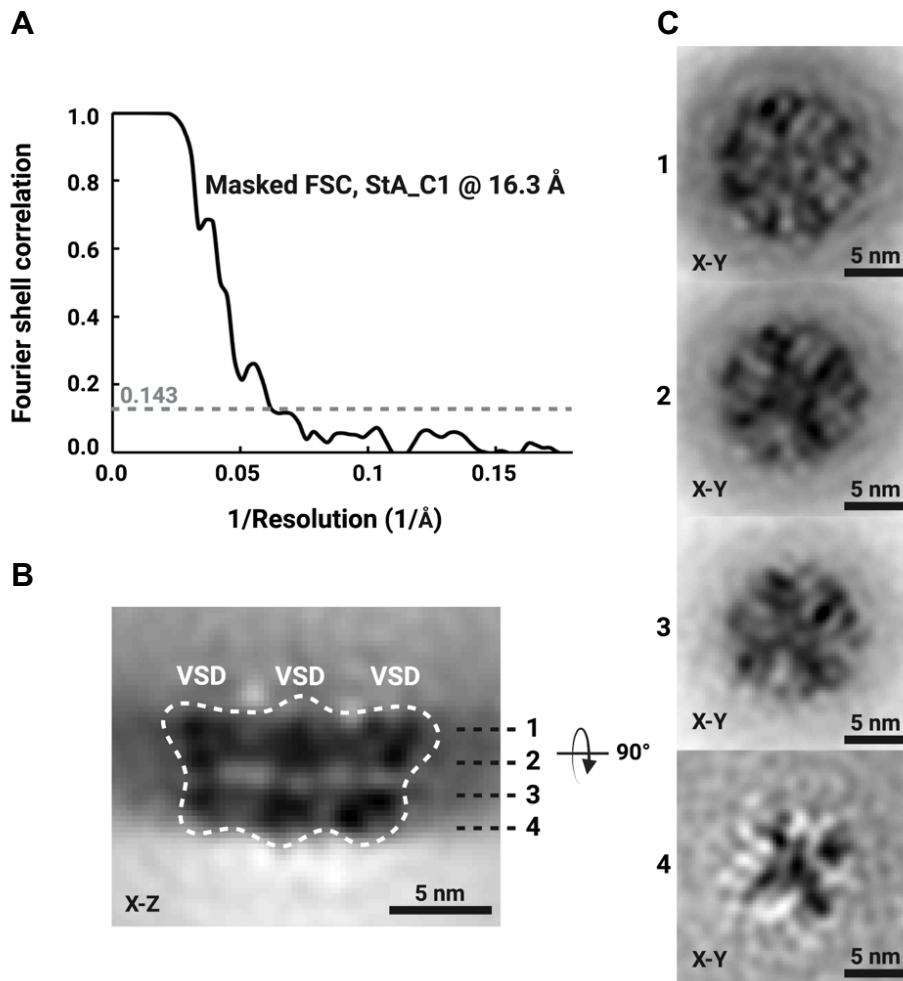


Figure 2.16 Fourier shell correlation (FSC) curve of the masked map and slices through the structure of NaChBac map in liposomes along the z-axis. (A) Gold standard FSC (criteria 0.143) curve of the masked map with a reported resolution of 16.3 Å for the map with C1 symmetry. (B and C) The voltage sensing domains (VSDs) and a pore domain (PD) could be visualized as a tetrameric feature in the X-Y plane along the z-axis. The white dashed mask indicates the mask used for refinement.

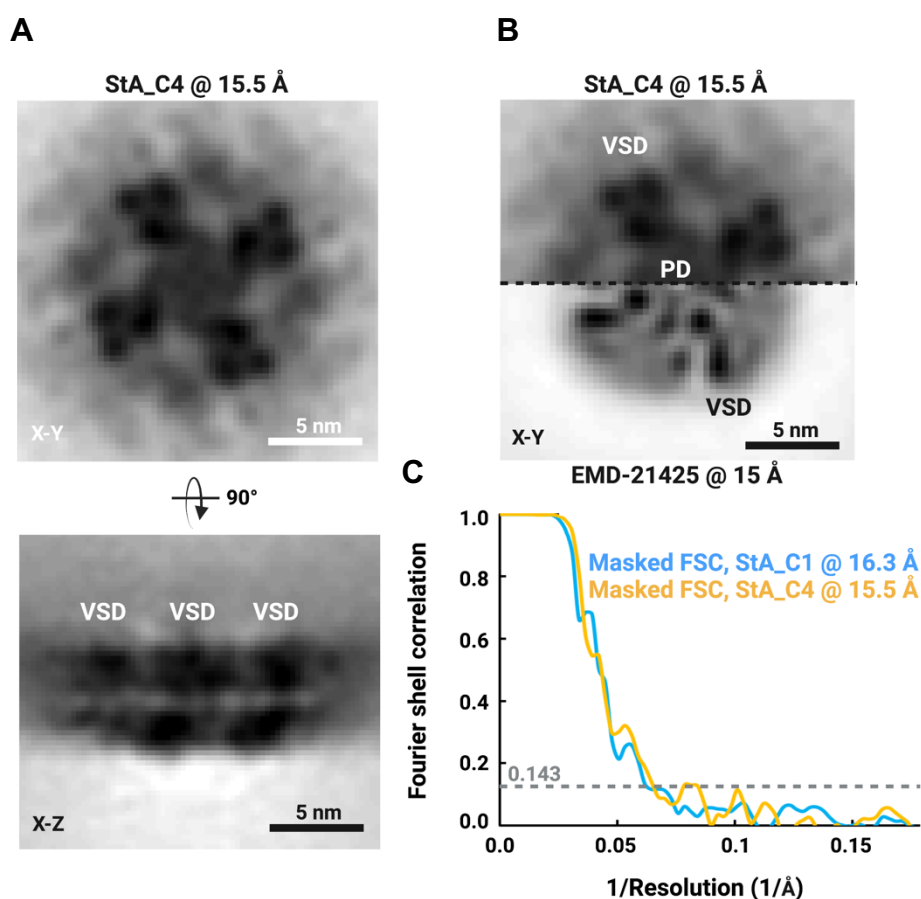


Figure 2.17 Structure of NaChBac embedded in liposomes with C4 symmetry. (A) The central pore domain (PD) surrounded by four voltage sensing domains (VSDs) could be visualized in the StA map of NaChBac in a liposome. (B) Comparison of the StA map (above) at 15.5 Å resolution with the recalculated cryo-EM structure (EMD-21425) at 15 Å resolution (below) showed an overall similarity. The volumes were mutually aligned. (C) Gold standard FSC (criteria 0.143) curve of the masked map with a reported resolution of 15.5 Å for the map with C4 symmetry.

2.3.5 Structural analysis of NaChBac in liposomes

The StA map provided a clear visualization of the domains of NaChBac in the lipid bilayer. At this domain-level resolution, the tetrameric-appearing pore domain (PD), which contains eight full transmembrane helices, and the four smaller voltage-sensing domains (VSDs), each of which contains four transmembrane helices, could be identified. Comparison of the StA reconstruction with the map from the single particle cryo-EM structure in lipid nanodisc reported previously (EMD-21425), resampled and low-pass filtered to 16 Å, showed an overall similarity (**Figure 2.18 A to C**). The corresponding atomic model fitted the StA density well, considering the moderate resolution (**Figure 2.18 D to F**). Interestingly, the StA structure was

~8 Å, or ~10% wider compared to the structure in nanodiscs filtered to the same resolution (Figure 2.18 A and B). However, given the current achievable resolution of the structure, it is not possible to see the conformational changes of the channel caused by changes in membrane potential. The observed increase in channel size may not solely be attributed to the applied potential but could also be a consequence of imaging the channel in a lipid bilayer without physical restraints.

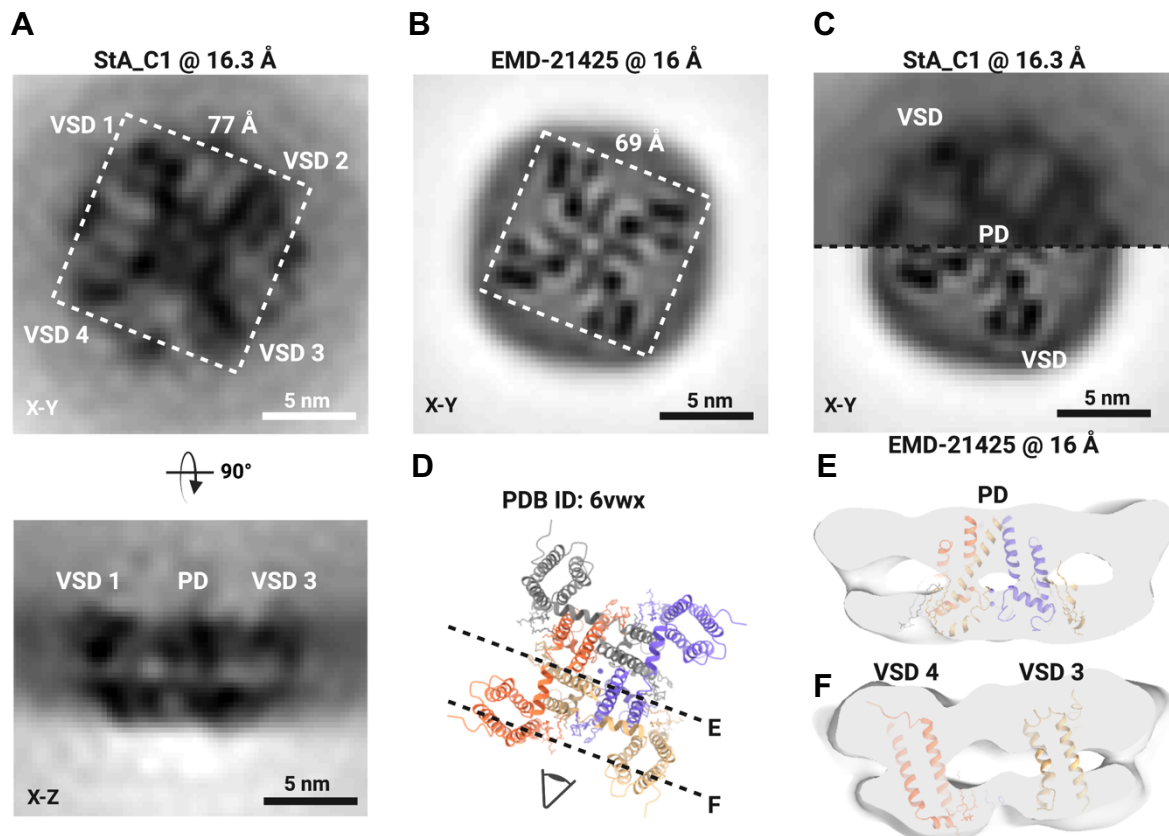


Figure 2.18 Structure of NaChBac in proteoliposomes and comparison to the structure in nanodiscs (EMD-21425). (A) StA map of NaChBac embedded in a liposome. (B) Cryo-EM map of NaChBac embedded in a nanodisc. (C) Comparison of the StA map (above) at 16.3 Å resolution with the recalculated cryo-EM structure (EMD-21425) at 16 Å resolution (below). The volumes were mutually aligned. The voltage sensing domains (VSDs) and pore domain (PD) could be visualized as a tetrameric feature from the top of the StA structure. (D) Atomic model of EMD-21425 in an inactivated state. (E and F) Segmented StA maps of NaChBac embedded in a liposome overlaid with the atomic model built based on the single particle cryo-EM structure (EMD-21425). The model showed the density of the PD surrounded by four VSDs based on the fit of the PDB ID: 6vwx to the StA map.

2.4 Summary and discussion

To better understand the structures and functions of membrane proteins, it is important to create an environment like liposomes that can mimic their physiological conditions. Despite extensive functional characterizations using proteoliposomes, there have been limited attempts to employ this system for the structural elucidation of small membrane proteins.

The results of this study demonstrate the feasibility of identifying and aligning small, mostly transmembrane proteins like NaChBac embedded in liposomes using StA and obtaining a correct structure, albeit at a modest resolution compared to the limits of single-particle analysis (SPA) processing. Here, fused GFP was used to locate the proteins of interest in tomograms and perform a rough alignment. However, for the final steps of the alignment, GFP was not useful due to the flexibility of the linker region. It is possible that a more ordered interacting partner, such as a specific toxin¹⁹¹, a Fab fragment¹⁹² or a legobody¹⁹³, would be more useful to support particle alignment to the average. Toxins or Fab fragments were not used in this study, as their structures would likely be similar to previously reported structures of purified channels^{160, 191}. The tetrameric NaChBac with a molecular weight of ~120 kDa and mostly transmembrane residues is on the smaller side of the molecular weight range that could be approached using current technology. For the structure determination, the channels were imaged in thin ice, a large number of particles were picked, and a combination of classification algorithms (Dynamo and RELION-4.0) was used. Even with such optimizations, the achieved resolution was only ~16 Å. While this resolution is higher than the average resolution of StA structures deposited in the Electron Microscopy Data Bank in 2022 (20 Å), it provides only domain-level resolution. I believe that imaging of even smaller proteins in membranes without large soluble domains, such as monomeric GPCRs without interaction partners, may be too ambitious given the current level of technology.

At the obtained resolution, the pore (PD) and voltage-sensing domains (VSDs) of the channel could be reliably observed. It was estimated that the structure of the channel in proteoliposomes is ~10% wider than the structure reported in nanodiscs (EMD-21425) filtered to the same resolution. This could be physiologically relevant for two reasons. Firstly, nanodiscs have been shown to confine lipids inside the polymer¹⁹⁴ and to modify the conformations of pentameric ligand-gated ion channels¹⁹⁵. Secondly, molecular dynamics simulations for the K_v channel

have showed substantial motion of the VSDs¹⁹⁶, which, on average, could make the proteins wider compared to the compact versions typically observed in nanodiscs. The possible motion of the VSDs is another factor that potentially limits the obtainable resolution and could partially explain why the application of the C4 symmetry in this case did not lead to a much-improved structure. While the observed increase in protein diameter might be a result of the applied membrane potential, a recent report by Mandala and MacKinnon on the movements of the VSDs in the Eag K_v channel showed that the cryo-EM structures of the channel with and without the transmembrane potential were overall similar in size¹⁶¹. Therefore, in the case of NaChBac, the increased size of the channel may not be solely due to the applied potential but rather a consequence of imaging the channel in a lipid bilayer without physical restraints.

The approach presented in this study, which can be widely applied to cryo-EM analysis of membrane proteins, with a specific focus on membrane proteins with small soluble domains, lays the foundation for cryo-ET and StA of integral or peripheral membrane proteins whose functions are affected by transmembrane electrochemical gradients and/or membrane curvatures.

Chapter 3

Molecular architecture of the knob complex in *Plasmodium falciparum*-infected human erythrocytes by cryo-ET and StA

3.1 Introduction

3.1.1 Malaria and the parasite *Plasmodium falciparum*

Malaria is a disease caused by the parasite *Plasmodium falciparum* and typically presents symptoms such as fever, tiredness, vomiting, and headaches. In severe cases, it can lead to jaundice, seizures, coma, or even death. Despite over a century of efforts to eradicate or control malaria, it remains a major and growing threat to the public health and economic development of countries in the tropical and subtropical regions worldwide. According to the *World Malaria Report 2022*, malaria cases continued to rise in 2021, although at a slower pace compared to 2020. An estimated 247 million cases were reported in 2021, compared to 245 million in 2020 and 232 million in 2019. Additionally, there were approximately 619,000 malaria-related deaths in 2021, which was 6,000 (1%) fewer than in 2020, but still 51,000 (9%) higher than in 2019 before the COVID-19 pandemic. A large portion of these additional malaria deaths and cases can be attributed in part to COVID-19-related disruptions, which constrained access to crucial malaria interventions. However, there is hope in the ongoing development of new anti-malaria tools and strategies, including insecticide-treated bed nets, rapid diagnostic tests, and anti-malarial treatments such as artemisinin-based combination therapy and malaria vaccines. These advancements offer a promising pipeline for combating malaria and reducing its devastating impact (**Figure 3.1**)¹⁹⁷.

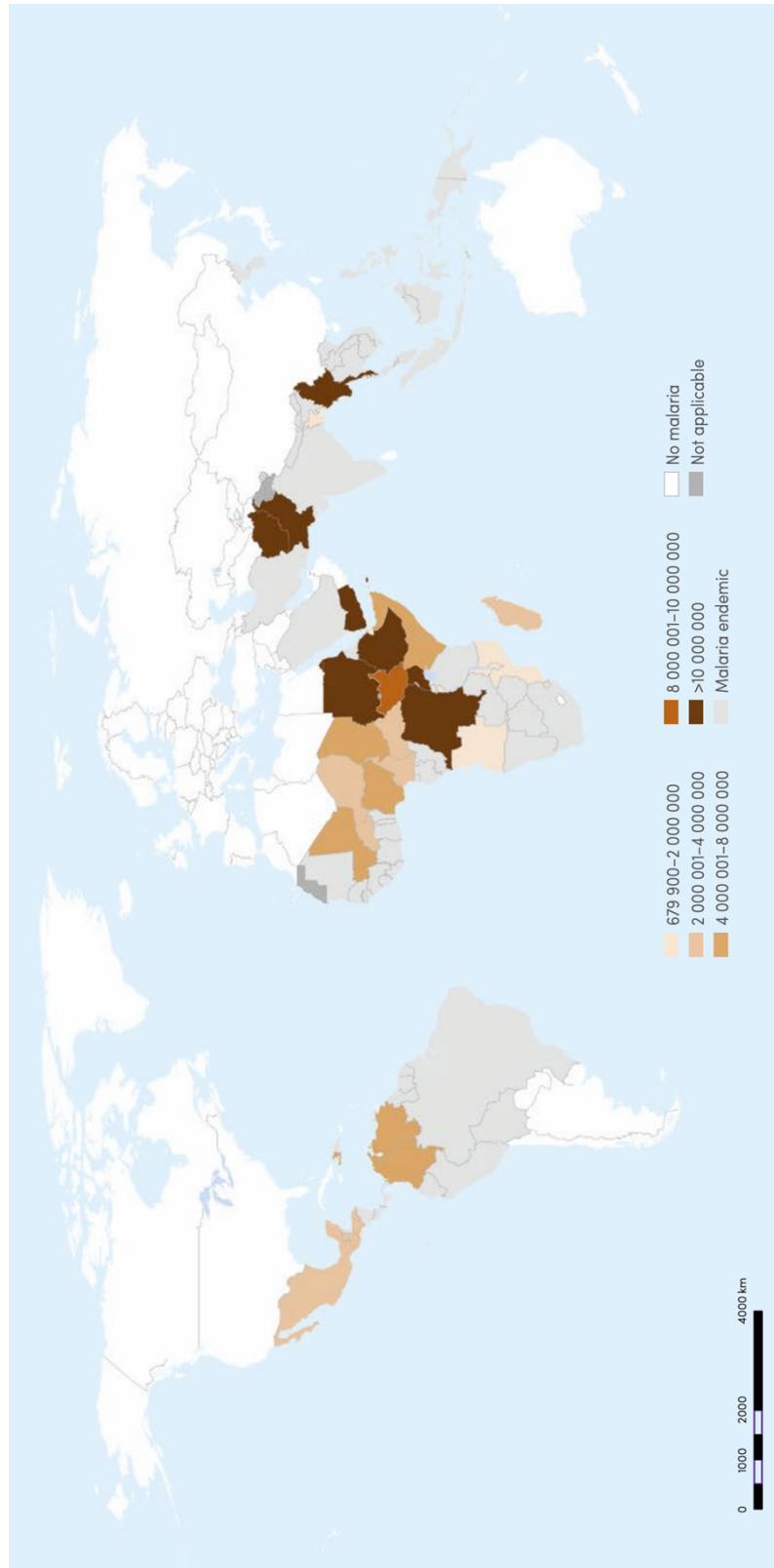


Figure 3.1 People in humanitarian need in malaria-endemic countries as of December 2021. Many malaria-endemic countries have been facing with health and humanitarian emergencies. In these regions, increases in malaria cases, what could be partly attributed to the COVID-19 pandemic. Image from¹⁹⁷.

Malaria is a blood infection caused by mosquito-borne parasites belonging to the genus *Plasmodium*. These parasites invade and replicate within the red blood cells of their vertebrate hosts, leading to the manifestation of the disease. Among the five *Plasmodium* species that infect humans, *Plasmodium falciparum* is responsible for the majority of morbidity and mortality associated with malaria^{198, 199}. This is due to the parasite's ability to sense changes in its environment and respond through a process called antigenic switching. Antigenic switching allows the parasite to evade destruction by the human immune response, contributing to the chronic nature and virulence of the disease²⁰⁰. However, the precise mechanisms that enable these parasites to undergo antigen switching are not yet fully understood.

A defining feature contributing to the pathogenicity of *P. falciparum* is its ability to express a series of cytoadherence proteins on the surface of the host's red blood cells (RBCs). Exported proteins of the malaria parasite interact with proteins of the erythrocyte membrane, inducing substantial changes in the morphology, physiology, and function of the host cell²⁰¹. Among these proteins, the primary antigenic and virulence determinant of *P. falciparum* is a variant surface protein called *P. falciparum* erythrocyte membrane protein 1 (PfEMP1). Different forms of PfEMP1 are encoded by a multicopy gene family called *var*, and switching between active genes enables the parasites in the infected RBCs to evade the antibody response of their human hosts²⁰²⁻²⁰⁴. Additionally, the merozoite surface protein 1 (MSP-1) is the most abundant protein on the surface of the erythrocyte-invading *Plasmodium* merozoite, which is the causative agent of malaria. MSP-1 plays a crucial role in merozoite formation, entry into and escape from erythrocytes, making it a promising candidate antigen for vaccine development²⁰⁵. Recent cryo-EM single-particle analysis (SPA) has provided structural insights into the possible mode of interaction between MSP-1 and erythrocytes, establishing a framework for future investigations into the role of MSP-1 in *Plasmodium* infectivity and antibody-mediated protection from malaria²⁰⁶. Further research is required to unravel the complexity of these processes, and understanding the molecular interactions of these key proteins could pave the way for the development of novel strategies to combat malaria and advance vaccine research.

3.1.2 Knob complex and its interactions with the erythrocyte membrane skeleton during *P. falciparum* infection

Red blood cells infected with the human malaria parasite *P. falciparum* acquire thousands of small protrusions that render their initially smooth surface bumpy²⁰⁷. These protrusions, known as knobs, play a pivotal role in the pathophysiology of *falciparum* malaria during the mature trophozoite and schizont stages²⁰⁸ (**Figure 3.2 A**). Knobs form a platform on which parasite-encoded adhesins, such as the immune-variant PfEMP1 antigens, are presented and anchored to the RBC membrane skeleton²⁰⁹. Consequently, parasitized erythrocytes become sticky and acquire cytoadhesive properties to vascular endothelial receptors, leading to sequestration within the microvasculature of various organs²¹⁰ (**Figure 3.2 B**). In this condition, the parasites induce an immune response and evade destruction in the spleen^{211, 212}, which, in turn, severe sequelae may occur, including impaired tissue perfusion, hypoxia, and local microvascular inflammation, followed by barrier dysfunction^{213, 214}. Knobs also play an important role in reorganizing and stiffening the cell envelope, leading to rounder shapes and reduced deformability of infected erythrocytes^{215, 216}. The combined effects of knob formation and cytoadhesion contribute to the pathogenicity of *P. falciparum*, making it a highly virulent and dangerous malaria parasite.

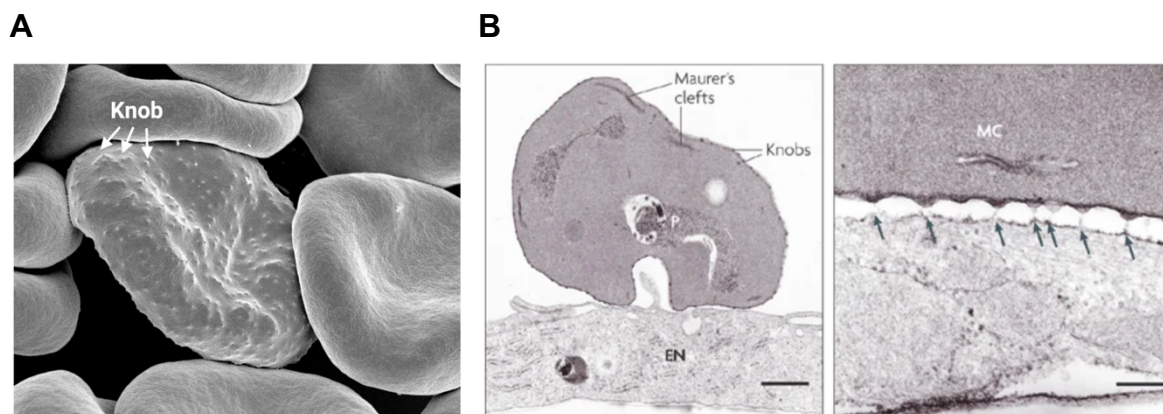


Figure 3.2 Electron micrographs of red blood cells infected with *Plasmodium falciparum*. (A) A scanning electron microscopy (SEM) image showed a knob-rich infected RBC surrounded by knobless uninfected RBCs. Credit: Rick Fairhurst and Jordan Zuppann, National Institute of Allergy and Infectious Diseases, National Institutes of Health. (B) Left: a transmission electron micrograph of a parasite-infected RBC adhering to the surface of a microvascular endothelial cell (EN). Scale bar: 1 μm . Right: details of the interface between an infected RBC and an endothelial cell, showing strands of electron-dense connecting material located at knobs (arrows). MC: Maurer's cleft. Scale bar: 100 nm. Image from^{201, 217}

Previous studies have suggested that knobs are supramolecular complexes composed of parasite-encoded factors and components of the erythrocyte membrane skeleton²⁰⁹. Cryo-electron tomography (cryo-ET) has revealed that the parasite utilizes actin from protofilaments to generate long actin filaments that connect the knobs with the Maurer's clefts. These actin filaments act as cables for the vesicular trafficking of PfEMP1 and other parasite factors to the surface of the infected RBCs^{218, 219}. A major building block of the knob complex is the knob-associated histidine-rich protein (KAHRP), a parasite-encoded protein that assembles into a ring-shaped structure essential for the formation of the virulence complex²²⁰. Parasite mutants lacking the KAHRP gene fail to form knobs in RBCs, leading to a loss of cytoadherence to the vascular system²²¹. KAHRP features several low-affinity interaction domains, allowing it to self-aggregate and bind to actin, ankyrin, spectrin, spectrin-actin band 4.1 complex, and the cytoplasmic domain of PfEMP1 antigens²²²⁻²²⁷. However, the spatial and temporal aspects of knob assembly are still debated. In particular, there are differing views on the specific locations where knobs form, whether at the actin junctional complex^{224, 228}, the ankyrin bridge²²², or in the mesh formed by spectrin filaments²²⁰.

Advances in research have provided insights into the structural organization of knobs, revealing a spiral-like scaffold beneath them by negative stain tomography¹⁴⁵ (**Figure 3.3 A to C**). Recent breakthroughs in super-resolution fluorescence microscopy and image processing techniques^{229, 230} have offered an exciting prospect for investigating the cytoskeletal organization of membrane-preserved erythrocytes at the nanometer scale²³¹. Utilizing this technology, a study has shown that the KAHRP initially interacts with various skeletal components, including ankyrin bridges. As the infection progresses, KAHRP undergoes relocalization to remodeled actin junctions, eventually associating with knob spirals in *P. falciparum*-infected erythrocytes²³². However, the molecular composition of the knob spiral remains unclear, and further investigations are required to understand the overall architecture of the knob complex and its interactions with membrane skeleton in RBCs (**Figure 3.3 D**)²³³.

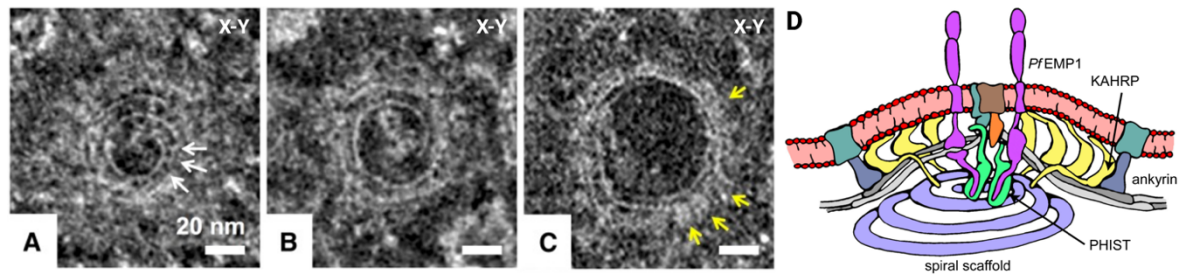


Figure 3.3 Spiral-like feature of knob complex and model of knob formation structure. (A to C) Sections taken at different heights through a knob in a negative-stained tomogram, showing a spiral-like structure. White arrows in (A) indicate examples of radiating connections between turns, while yellow arrows in (C) indicate diffuse coating material with a radiating pattern. Image from¹⁴⁵. (D) The proposed model illustrates the knob complex, characterized by high protein density resulting from KAHRP self-association and the formation of spiral assemblies. Image from²²².

3.1.3 Aim

Knob complex plays a crucial role in the pathophysiology of *P. falciparum* malaria by forming membrane protrusions in malaria-infected erythrocytes, resulting in the sequestration of parasitized erythrocytes in the microvasculature and leading to severe diseases.

Imaging the knob complex using *in situ* cryo-electron tomography (cryo-ET) in *P. falciparum*-infected human erythrocytes provides a unique opportunity to directly visualize the 3D structure of the knob complex at different stages of parasite development and to explore its association with the erythrocyte membrane skeleton.

Structure determination of the knob complex by subtomogram averaging (StA) can offer structural insights, guiding future work to uncover the molecular composition and the role of these native knobs in *Plasmodium* infection and immunity (Figure 3.4).

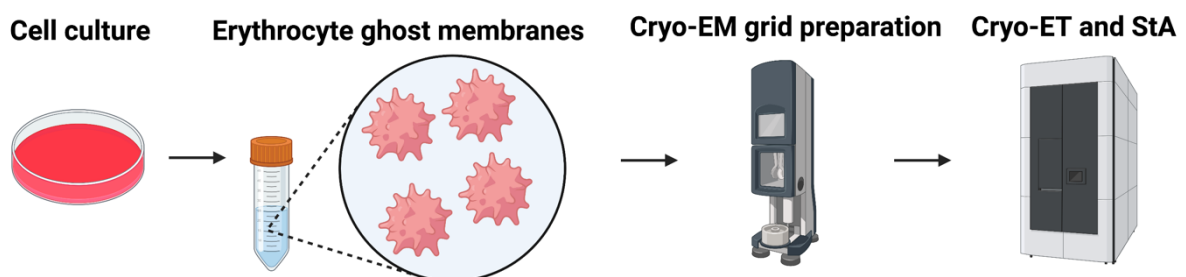


Figure 3.4 Graphic workflow of Chapter 3.

3.2 Materials and methods

3.2.1 Materials, instrumentation, and programs

3.2.1.1 Materials

DTT, Dithiothreitol (Thermo Fisher Scientific)

Fiducial gold 10 nm (Cell Microscopy Core, University Medical Center Utrecht)

GlutaMAX (Thermo Fisher Scientific)

Halt Protease Inhibitor cocktail (Thermo Fisher Scientific)

Heparin 25000 (Ratiopharm)

Magnesium chloride (Carl Roth)

PBS (gibco)

RPMI 1640 medium (gibco)

Sodium phosphate (Carl Roth)

Sorbitol (Carl Roth)

Whatman® No. 1 filter paper (Whatman)

3.2.1.2 Instrumentation

Avanti J-20 XP centrifuge (Beckman Coulter)

Glow discharge cleaning system, easiGlow™ (PELCO)

JA-20 Fixed-angle rotor (Beckman Coulter)

K2 Summit direct detection camera with Quantum energy filter (Gatan)

Titan Krios G1 cryo-TEM (Thermo Fisher Scientific)

VarioMACS™ Separator (Miltenyi Biotec)

Vitrobot Mark IV (Thermo Fisher Scientific)

3.2.1.3 Programs

Dynamo 1.1.532

Gctf 1.06

IMOD 4.11

MATLAB 2023

MotionCor2 1.6.3

SerialEM 4.0

The illustrations in this chapter were created with BioRender.com.

3.2.2 Methods

3.2.2.1 Parasite culture and erythrocyte ghost membrane preparation

Samples were provided from the group of Prof. Dr. rer. nat. Michael Lanzer at the Universitätsklinikum Heidelberg. Briefly, the *P. falciparum* clonal line FCR3 and the FCR3-derived clonal mutants were cultured as described²³⁴. Fresh HbAA erythrocytes (<10 days old after blood donation) were resuspended in RPMI 1640 medium supplemented with 5% GlutaMAX and 5% human serum in the following conditions: 4% hematocrit, <5% parasitemia, 37 °C temperature, 5% O₂, 3% CO₂, and 96% humidity.

To synchronize the cultures, schizont-infected erythrocytes were sterile purified using a strong magnet (VarioMACS™ Separator)²³⁵ and mixed with fresh erythrocytes to achieve high parasitemia. 5,000 heparin units per mL were added, and the cells were returned to culture for 4 hours²³⁶. After heparin treatment, cells were washed with pre-warmed supplemented RMPI 1640 medium and returned to culture for 2 hours to allow reinvasion of erythrocytes. Subsequently, cells were treated with 5% sorbitol to remove late parasite stages²³⁷. Cells were fed every 4 hours, and samples were collected at the indicated time points post-invasion.

Highly synchronized parasite cultures at the trophozoite stage were magnet purified, and membrane ghost were prepared by incubating the cells in lysis buffer (5 mM sodium phosphate pH 7.4, 2 mM MgCl₂, 1 mM DTT, and 1x Halt Protease Inhibitor cocktail) for 5 minutes on ice. After centrifugation at 17,000 × g for 15 minutes at 4 °C, the membranous upper layer was collected and washed several times with lysis buffer (**Appendix Figure C.1**).

3.2.2.2 Sample preparation, cryo-ET, and image processing of *P. falciparum*-infected human erythrocytes

The prepared erythrocyte ghost membranes were mixed with 10-nm gold fiducial markers in PBS buffer. A 3 μL aliquot of this mixture was applied to a glow-discharged holey carbon grid (Quantifoil Cu R2/2, 400 mesh), blotted with Whatman® No. 1 filter paper, and then plunge-frozen in liquid ethane. Cryo-ET imaging was performed on a Titan Krios microscope equipped with a Gatan Quantum energy filter and a Gatan K2 Summit direct detector operated by SerialEM software¹⁸⁰. A total of 43 tomographic series was acquired using a dose-symmetric scheme¹⁸¹, with tilt range ±60°, 3° angular increment and defoci between -5 and -6 μm. The acquisition magnification was 42,000 ×, resulting in a calibrated pixel size of 3.39 Å. The electron dose for every untilted image was increased to ~10 e⁻/Å², and tilt images were recorded

as 10-frame movies in counting mode at a dose rate of approximately $0.62 \text{ e}^-/\text{\AA}^2/\text{s}$, with a total dose per tomogram of $\sim 110 \text{ e}^-/\text{\AA}^2$ (**Appendix Table C.1**).

Motion correction of tilt-series movies was performed using MotionCor2¹⁸³, and tilt-series were aligned based on the gold fiducials using the IMOD package¹⁸⁴. Contrast transfer function (CTF) estimation was performed using defocus values measured by Gctf¹⁸⁶ for each projection. Tomograms were reconstructed from CTF-corrected and aligned stacks using weighted back projection in IMOD. Tomograms were further binned 2 and 4 times (referred to as bin2 and bin4 tomograms), resulting in pixel sizes of 6.78 and 13.56 Å, respectively.

3.2.2.3 StA of knobs

StA was performed using the Dynamo package²³⁸. To define initial subtomogram positions, the center of cubic voxels was manually picked on bin4 tomograms (489 particles), using the Dynamo Catalogue system¹⁸⁷. Initial alignment was performed manually on 90^3 -pixel subtomograms extracted from bin4 tomograms. The centers of the spirals and the direction of the central axis were defined using `dynamo_gallery` after which the roughly aligned particles were summed up low-pass-filtered to 60 Å. This volume was used as an initial reference. Multireference alignment and averaging were performed on bin2 particles in 180 voxel boxes, with the first step involving a 360° search around the vertical axis of the spiral. A soft-edged sphere alignment mask was applied throughout, and the full data set was aligned against the core of knobs, revealing prominent spiral-like structures under the lipid bilayer. Subsequent iterations of refinement were performed on subtomographs of 360 voxels extracted from unbinned tomograms, with constrained refinement of shifts and angular search on statistically independent odd and even data sets. A population of particles with the lowest cross-correlation (around 20%) was removed by imposing a cross-correlation threshold. The final converged averages were formed by 332 particles, and the resolution was determined using `dynamo_fsc`. Further alignments were performed using ellipsoid masks focused on two different regions of the spiral structure (middle and peripheral regions) to generate four maps. The subboxes were extracted at 40 positions around the second and third spiral turn of each particle using `dynamo_subboxing_table`. Symmetry was not applied for consecutive refinements.

3.3 Results

3.3.1 Cryo-ET of *P. falciparum*-infected human erythrocytes *in situ*

To gain deeper insights into the structural organization of knobs, cryo-ET was applied to image membrane ghosts prepared from infected erythrocytes, preserved through rapid freezing in vitreous ice (**Figure 3.5 A and Appendix Figure C.2 A**). The tomograms revealed the erythrocyte plasma membrane and knobs in top and side views (**Figure 3.5 B and Appendix Figure C.2 B**). A prominent feature observed was the spiral scaffold underlying the knobs (**Figure 3.5 C**), which is consistent with previous findings¹⁴⁵. Most of the spirals displayed at least 4-5 turns, occasionally reaching six or more (**Figure 3.5 D and Appendix Figure C.2 C**), with average basal diameters ranging between 55 and 64 nm. Smaller spirals with diameters of 27-34 nm, corresponding to one or two turns, were also observed (**Figure 3.5 E**). These smaller spirals might represent intermediate or premature structures²²⁰. In addition, several crown-like densities were apparent in tomograms, decorating at the flexible periphery of knobs; however, the number of densities per knob spiral varied (**Figure 3.5 F**).

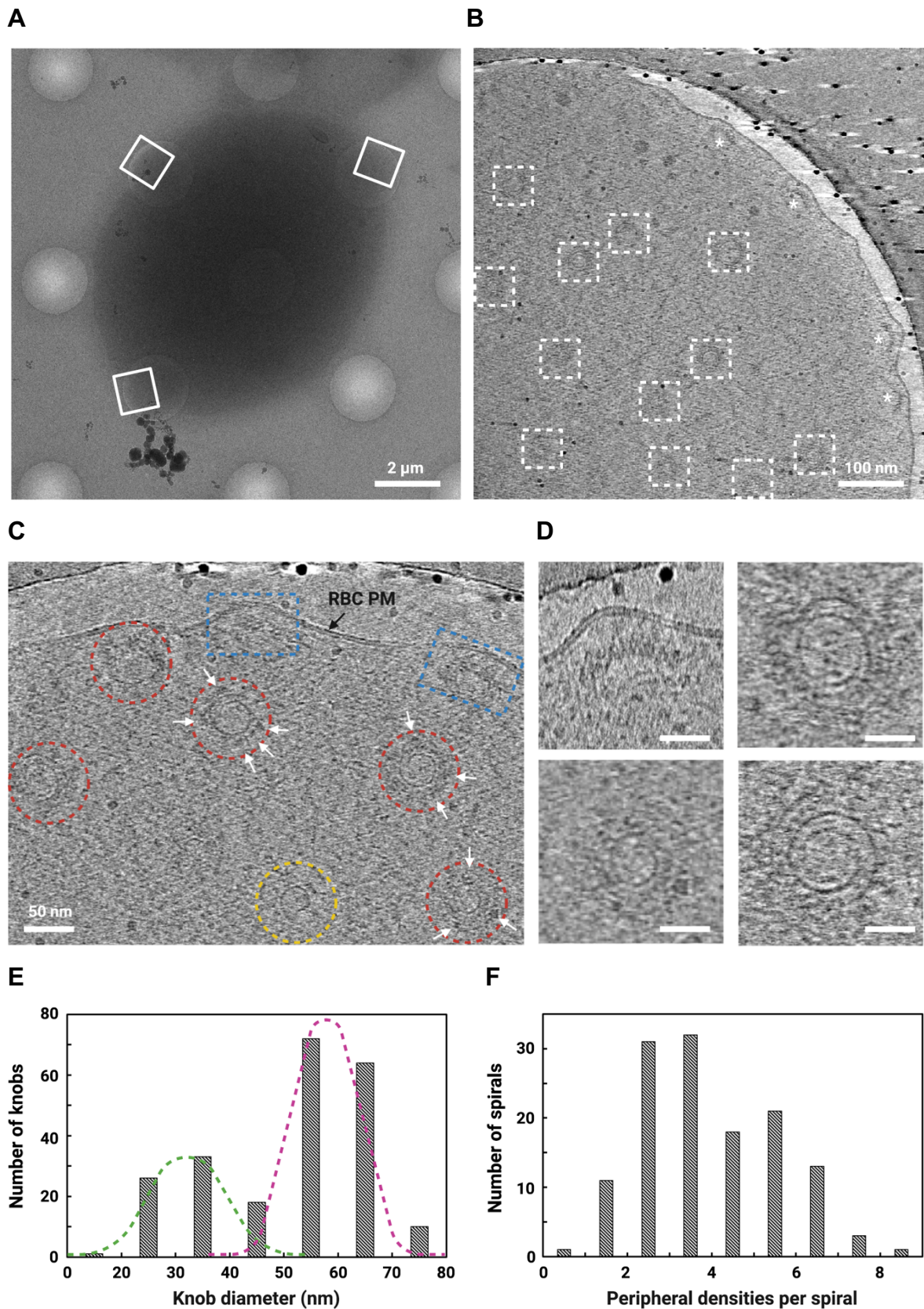


Figure 3.5 Cryo-ET of knob spirals. (A) Low magnification cryo-image of a membrane ghost prepared from a trophozoite-infected erythrocyte, showing the ghost deposited on a holey EM-grid. White squares indicate areas for automated data acquisition. (B) Knob spirals in top views

and side views are marked by white squares and asterisks, respectively. (C) A section through a tomogram showing knobs and the underlying spiral in top view (red circles) and side view (blue boxes). A presumably premature spiral is highlighted in a yellow circle. Arrows indicate peripheral densities. (D) Examples of top and side views of knob spirals showed different sizes of knobs. Scale bars: 20 nm. (E) Measurements of the radius for individual knobs. (F) Number of peripheral crown-like densities per spiral.

3.3.2 StA of knob spirals

A total of 489 subtomograms of knob spirals were manually picked, and the initial alignment was carried out manually using Dynamo. This volume served as an initial reference. After several rounds of classification to clean junk particles and gold fiducial markers using an ellipsoid mask (**Figure 3.6 A**), attempts to align the knob spirals using a soft-edged mask covering the entire knobs were unsuccessful. The resulting average showed only a donut-like shape without revealing any details of the knob spirals (**Appendix Figure C.3 A**). Notably, despite knob spirals displaying varying sizes (indicating different turns) in the tomograms, the core of the knob spirals appeared to be less flexible and exhibited similar features suitable for alignment. Therefore, a small soft-edged sphere alignment mask was applied throughout, and the full data set, after the particle cleaning, was aligned only against the core of the knobs. This revealed prominent spiral-like structures underneath the lipid bilayer (**Figure 3.6 B and Appendix Figure C.3 B and C**). Subsequent refinements were performed on subtomographs extracted from unbinned tomograms, using a constrained refinement of shifts and angular search with a narrow mask (**Figure 3.6 C**), yielding a final resolution density map of 31.3 Å (332 particles in the final map) (**Figure 3.7 and Appendix Figure C.4**).

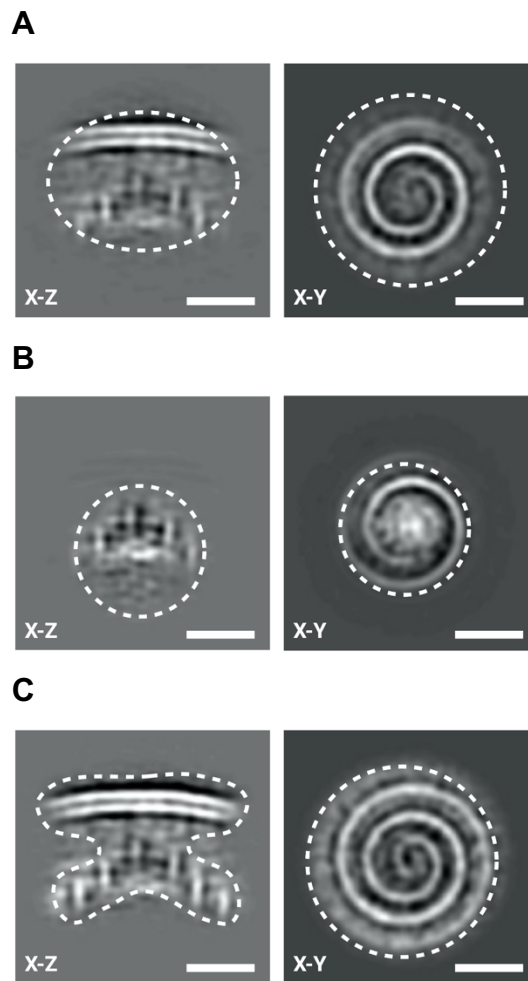


Figure 3.6 Masks used for the StA analysis of spirals. (A) A larger ellipsoid mask covering the whole knob was used for classification. (B) A small sphere mask was applied to the core region of spirals for particle alignment. (C) A dumbbell-like mask was used for the refinement and FSC determination. Scale bars: 20 nm.

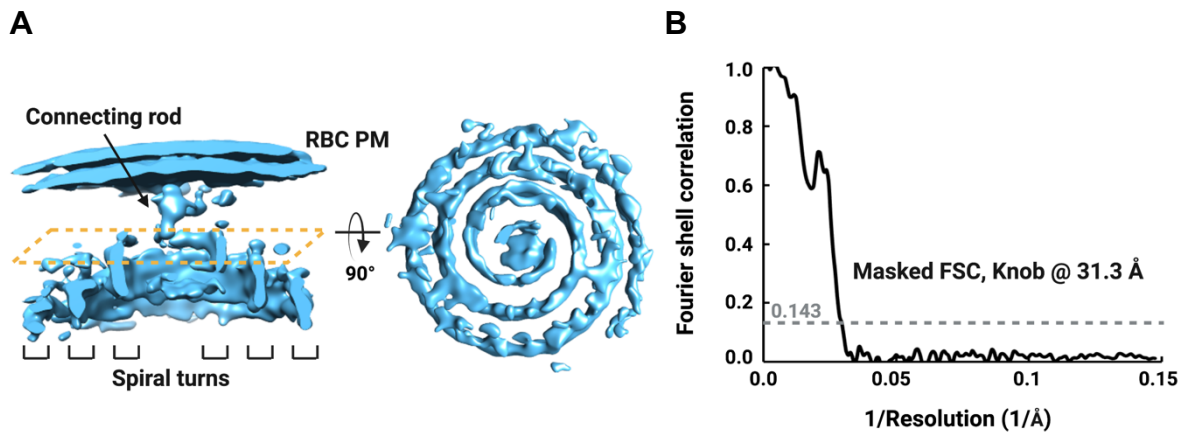


Figure 3.7 Structure of the knob complex. (A) Density map of the knob complex in cross-sectional view. The plasma membrane (PM) of the red blood cell, the connecting rod between the spiral and the plasma membrane, and the spiral turns are indicated (left). Top view of the knob spiral without the plasma membrane (right). (B) A Fourier shell correlation (FSC) curve indicated a resolution of the reconstruction of ~ 31 Å.

3.3.3 3D structure of the knob complex

The resulting map revealed a well-organized knob core with an underlying four-turn spiral attached to the erythrocyte membrane through a rod-like connector (**Figure 3.7, 3.8 A and B**). The spiral was ~ 32 nm in height and ~ 53 nm in basal diameter (between centers of mass), with a spacing of ~ 8 nm between each turn. The entire spiral blade was about 760 nm in length, 3.5 nm in width (limited by the resolution of 3 nm), and 8 nm in height. The spiral rose at an angle of $\sim 36^\circ$ and had a major rod-like structure at its tip that extended toward the inner leaflet of the erythrocyte plasma membrane, hypothesized to be composed of PfEMP1 proteins²³⁹. There were multiple less-ordered, stick-like densities between the erythrocyte plasma membrane and the spiral, potentially serving as linkers between the spiral and the plasma membrane. Although some spirals exhibited five or more turns, the additional turns could not be resolved in the map due to the less-ordered nature of the peripheral regions, resulting in their averaging out.

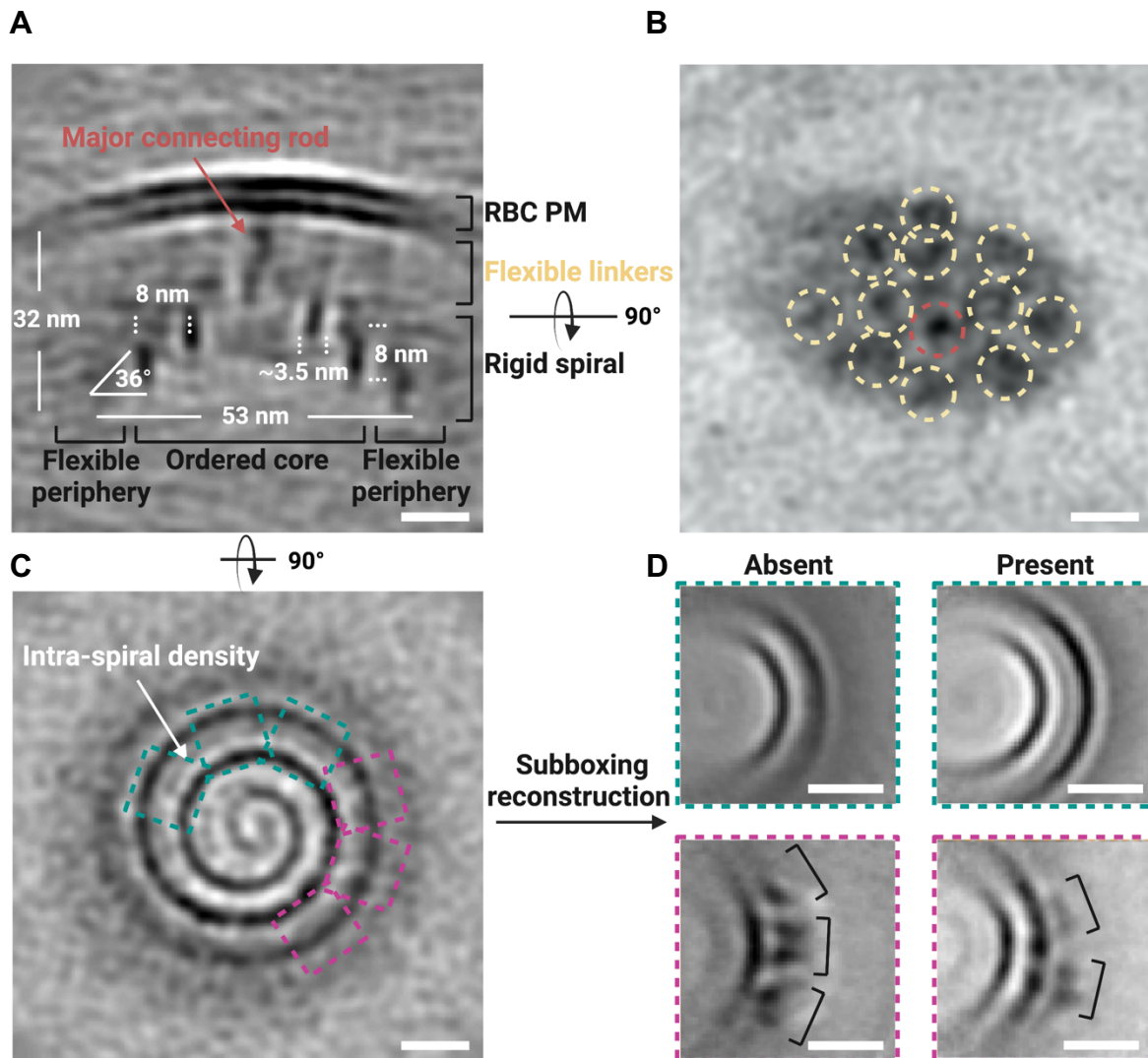


Figure 3.8 Structural analysis of the knob complex. (A) Slice through the average map of the knob with dimensions indicated. Scale bar: 10 nm. (B) Top view of a slice of RBC plasma membrane, showing a major connecting rod density (red) and several flexible linkers (yellow). Scale bar: 10 nm. (C and D) Averaged tomogram of the knob spiral in top view, highlighting intra-spiral densities between the second and third turn in some but not all spirals (green box), and peripheral crown-like densities at the outer turn, which are indicated by brackets (magenta box). Scale bar: 10 nm.

Next, local classification of the densities of the spiral turns was performed using the subboxing functionality of Dynamo. This involved radially extracting 40 smaller parts from each subtomogram, aligning and averaging them locally, rather than globally aligning the entire subtomogram of knobs. Two subboxing reconstructions at the radius of the second and the third turn of the spiral were averaged (**Figure 3.8 C**). Classification revealed the presence of intra-spiral densities between the second and third turn in some knob spirals, but not in all.

Additionally, crown-shaped densities were observed at the outer turn (**Figure 3.8 D**). This crown-like feature was also apparent in tomograms at the periphery of knobs, with the number per knob varying (**Figure 3.5 F**). The observed intra-spiral densities might correspond to associated proteins or protein complexes that contribute to the structural organization and stabilization of the knob complex. Further investigation is needed to identify and characterize these components and their role in knob formation and function.

3.4 Summary and discussion

The cell membrane of erythrocytes infected with the malaria parasite *P. falciparum* undergoes significant changes during the mature trophozoite and schizont stages, resulting in the formation of protrusions known as knobs on its surface. These knobs result in sequestration of parasitized erythrocytes in the microvasculature, leading to severe diseases. The structural organization of knob components, especially PfEMP1 on the RBC surface, is the main determinant for the cytoadhesive and rosetting capacity of the RBCs, enabling them to bind to various host receptors. It is also important for the variable antigenicity, which is crucial for immunoevasion. Another major constituent is the KAHRP, which is a central building block for knob spirals and is essential for the cytoadhesion of parasitized erythrocytes. KAHRP interacts with several membrane skeletal proteins of the host erythrocyte, including actin, ankyrin, spectrin, spectrin-actin band 4.1 complex, and PfEMP1.

This research has, for the first time, revealed the overall architecture of the knob complex in parasitized erythrocyte membrane ghosts using *in situ* cryo-ET and StA. The 31.3 Å map of the knob spiral corroborates previous observations¹⁴⁵, and it showed the presence of stick-like densities that seem to anchor the spiral to the lipid bilayer. Moreover, this study has uncovered additional features, including the intra-spiral densities between the second and third turn, which might stabilize the spiral. Crown-like extra densities were observed at the periphery of the spiral base, which might be involved in connecting the spiral with filamentous structures. The results further showed a high degree of variability between spirals with regard to the number of turns and the number of peripheral proteins, possibly reflecting different stages and/or functions of knob configuration²²⁰.

A recent comprehensive identification of the knob proteome has suggested that the knob complex includes KAHRP, PfEMP family, ankyrin, spectrin family, Band 3, Band 4.1, host Hsp70, elongation factor 1A, acyl-CoA synthetase, among others²⁴⁰. The structure of the knob complex obtained in this research provides a model to understand the organization of the core knob components and may reveal novel proteins as knob components in future studies, and possibly, it might reflect the processes involved in the parasite-induced reorganization and disassembly of the spectrin/actin network in human RBCs at the molecular level. The localization of KAHRP in the knob complex has been showed that KAHRP are decorated on the spiral blade based on the structure of the knob spiral obtained in this study²³². The reorganization of KAHRP might be mediated by the changing phosphorylation and/or acetylation pattern of KAHRP during the intraerythrocytic cycle^{241, 242}, thereby altering the affinity of the protein to components of the membrane skeleton. For further studies on the organization of the membrane skeleton in RBCs, the tomogram dataset in this project can be utilized to reveal the native structure of membrane skeleton in parasitized erythrocyte, which could be compared with cryo-EM structure of spectrin-actin junctional complex from healthy porcine erythrocytes²⁴³ or the organization of membrane skeleton in healthy mice²⁴⁴ and human erythrocytes²³¹.

The structural information obtained in this study provides an overall architecture of the knob complex, which can be established as a model to understand the interaction between core knob components and the erythrocyte membrane skeleton in the pathophysiology of malaria. This knowledge can be used in the development of improved vaccine design strategies or drug design approaches to destabilize the knob complex, which is a major virulence determinant in *P. falciparum* infections.

Chapter 4

Conclusions and future perspective

Recent experimental advancements in the field of membrane proteins have led to significant progress in their structural determination. Improved expression techniques, protein engineering strategies to enhance stability and reduce conformational heterogeneity, the use of small antibodies to stabilize protein conformations, and advancements in cryo-EM hardware and processing packages have contributed to an exponential increase in high-resolution cryo-EM structures. While other techniques such as X-ray crystallography, NMR, XFEL, and SAXS also offer a broad range of tools for studying membrane protein structure and function, cryo-EM stands out for its ability to determine the structure of membrane proteins and biological macromolecules with minimal specimen requirements and under crystal-free conditions. Moreover, cryo-EM is highly compatible with native membrane-reconstituted preparations, providing unprecedented opportunities to study membrane proteins in their more natural states.

The field of *in vitro* membrane protein structural biology has extensively utilized mild detergents, amphipols, or membrane mimetic systems like nanodiscs, salipro, and SMALPS. While these approaches have been valuable, they can not fully capture functionally important protein states that require an actual lipid bilayer environment. To address this, the use of liposomes or cell-derived vesicles, which can preserve physico-chemical environments relevant for membrane proteins, becomes essential for studying their structure, activity, and stability, especially when capturing transient or specific functional states. Additionally, determining membrane protein structures *in situ* is considered an ideal approach for understanding their functions and associated molecular networks in their cellular context. This approach does not require the purification of target molecules away from their native environment inside cells and tissues, which can provide valuable insights into their native interactions and activities. In this thesis, cryo-electron tomography (cryo-ET) and subtomogram averaging (StA) techniques have been applied to study membrane protein structures both *in vitro* and *in situ*. The prokaryotic NaChBac was reconstituted in liposome to study its structure in the resting state, allowing a closer representation of its native environment. On the other hand, the visualization of the membrane-associated knob complex in *Plasmodium*

falciparum-infected human erythrocytes was achieved, determining the structure with its native cellular context.

Chapter 2 presents a pioneering work in the field of cryo-ET/StA of VGSCs, utilizing liposomes to create an electrochemical gradient for studying the structure of voltage-gated sodium ion channels (VGSCs) under a physiological resting membrane potential. Prior to this study, VGSC structures had been determined in various conditions such as crystals, detergent micelles, or nanodiscs, but without the presence of a voltage difference across them. While previous research explored conformational changes of VGSCs through chemical cross-links, mutations, and toxins to capture or stabilize voltage-sensing domains (VSDs) in conformations resembling the resting state, the findings reported here are significant in demonstrating the importance of imaging the sodium ion channel in a lipid bilayer under physiological conditions, without physical restraints.

The success of proteoliposome reconstitution was confirmed by gradient ultracentrifugation and cryo-EM images. Reducing the rate of detergent removal improved the reconstitution efficiency, leading to higher protein copies per proteoliposome, as observed by cryo-ET. The fluorescence-based liposome flux assay supported the polarized proteoliposomes under the negative resting membrane potential (-100 mV) condition and confirmed their stability. While proteoliposomes have been extensively used for functional characterizations of membrane proteins, their successful application for structural elucidation of membrane proteins still remains limited. Identifying fully transmembrane proteins from proteoliposomes in electron micrographs, for further alignment and averaging, continues to be a challenging bottleneck. NaChBac is a small membrane protein without a significantly large soluble domain, and fused GFP allows identification of this 120-kDa mostly transmembrane protein in tomograms, and helps with the initial alignment, as tomograms contain the third dimension compared to 2D imaging in single-particle cryo-EM. Even with several optimizations such as particle extraction on small proteoliposomes (~50 nm in diameter) in thin ice regions and the use of a combination of classification algorithms (Dynamo and RELION-4.0), the obtained structure of NaChBac embedded in liposomes was only at a resolution of ~16 Å. While this domain-level resolution is higher than the average resolution of StA structures deposited to the Electron Microscopy Data Bank in 2022 (20 Å), the tetrameric NaChBac with mostly transmembrane residues is probably on the smaller side of the molecular weight and/or the size range that could be effectively approached using current technology. The map of NaChBac in liposomes is ~10%

wider than the protein structure in a nanodisc (EMD-21425). While the increased protein diameter might be a result of the applied membrane potential, a recent study on the Eag K_v channel showed that cryo-EM structures with and without the transmembrane potential were overall similar in size¹⁶¹. Therefore, it might be the case of NaChBac, the increased size of the channel is not solely a consequence of the applied potential but rather as a result of imaging the channel in a lipid bilayer without physical restraints.

Future improvements in electron detectors^{33, 41, 245} and phase plates⁵² hold the potential for obtaining higher quality data and consequently improved resolution of NaChBac or proteins of similar sizes in proteoliposomes. Further sample optimization to unify the size of proteoliposomes would reduce the structural heterogeneity and could lead to improved resolution. Increasing the number of particles can also improve the resolution, which can be achieved by processing more tomograms and picking more protein copies for StA. While the reconstruction of tomograms can be streamlined^{182, 185}, I did not manage to automate particle picking and had to pick them manually which was a very laborious process. Developments in machine learning and the potential applications for particle picking^{86, 246, 247} could streamline particle picking in the future. Obtaining higher-resolution structures will enable a deeper understanding of the factors influencing the conformations of sodium channels and their regulation by biophysical stimuli.

The success of the structural analysis here was benefited from the defined tetrameric shape of the channel. However, for even smaller proteins in membranes without large soluble domains or well-defined overall shapes, such as monomeric GPCRs without interaction partners, obtaining high-resolution structural information may be a challenging endeavor at the current level of technology. Perhaps in the future we will be able to obtain high-resolution structures of such targets with ongoing technological developments, and the approach and the knowledge gained in this study which can be widely applied to the cryo-EM analysis of other small membrane proteins, lays out a foundation and a processing pipeline for cryo-ET and StA of integral or peripheral membrane proteins whose functions are affected by transmembrane electrochemical gradients and/or membrane curvatures.

In chapter 3, cryo-ET and StA was employed to investigate the structure of the membrane-associated knob complex in *Plasmodium falciparum*-infected human erythrocyte membrane ghosts. Malaria is one of the deadliest infectious diseases, and the infected RBCs develop knob-

like protrusions on their membranes, leading to a sticky surface that allows them to attach to blood vessel walls through cytoadhesion. This attachment promotes the binding and accumulation of other RBCs, enabling the parasites to evade destruction in the spleen and induce an immune response. Previous studies have suggested that knobs are supramolecular structures composed of parasite-encoded factors, such as PfEMP1 and KAHRP, and the erythrocyte membrane skeleton, as revealed by proteomic analysis. While a spiral-like feature of the knob complex was observed by negative stain tomography, a native structure of the knob complex and the connections between the knob complex and the erythrocyte membrane are still lack. Chapter 3 presents the first cryo-EM structure of the knob complex *in situ* for the visualization of its scaffold and dynamics, providing insights into the connections between the knob complex and the erythrocyte membrane.

The ~ 31 Å map of the knob complex showed a spiral scaffold with stick-like structures on top, suggesting their role in anchoring the spiral to the lipid bilayer, enabling a further investigation into the interaction between the core knob complex and the erythrocyte membrane skeleton in the pathophysiology of malaria. Additionally, this study uncovered intra-spiral densities between the second and third turn, likely contributing to the stabilization of the spiral organization, and crown-like extra densities at the periphery of the spiral base, potentially involving in connections to membrane filamentous components. The results also showed a significant variability between different spirals in terms of the number of turns and peripheral proteins, possibly indicating various stages or functions of knob configuration. Future work could focus on imaging erythrocytes at different stages of infection using *in situ* cryo-ET/StA, and this might unveil the dynamic changes in the organization of the knob complex as the infection progresses, providing insights into the mechanisms underlying malaria pathophysiology and potentially guiding the development of targeted therapeutic interventions. In principle, through the utilization of parallel data collection and streamlined data processing, it could be possible to obtain higher-resolution structure of the knob complex. Improving the throughput and the number of particles by a factor of 10 might be achievable, potentially leading to a structure with a resolution of 15-20 Å. While it would be an improvement over the current structure, the potential new functional insights remain unclear. In order to unambiguously identify the building blocks of the complex and their interactions, a resolution in the range of 7-9 Å would be required. Achieving this would demand a significantly larger dataset to be acquired and processed.

The obtained structure of the knob complex can provide a model for understanding the organization of the core knob components, such as KAHRP and PfEMP1. The localization of KAHRP in the knob spiral has been identified based on the structure from this research. Similarly, the localization of PfEMP1, assumed to be the stick-like densities on top of knob spiral, can be further confirmed using the same approach. Future studies involving parasites with different parasite-encoded KAHRP mutants might show their different affinity for self-aggregation or binding to membrane skeleton proteins, such as actin, ankyrin, and spectrin, and possibly, it might reflect the processes of the parasite-induced reorganization and disassembly of the spectrin/actin network in human RBCs at the molecular level.

Sickle cell disease (SCD) is caused by a gene mutation that alters hemoglobin in RBCs. People with SCD show lower susceptibility to malaria compared to those with normal hemoglobin. During infection, individuals with SCD have 50 to 90 percent fewer parasites in their blood and clear the parasites faster than those with normal hemoglobin^{248, 249}. The misshapen hemoglobin in SCD affects the parasite's ability to complete its life cycle. The parasite triggers sickling of SCD hemoglobin, leading to the clearance of infected RBCs by the immune system before the parasite can infect other RBCs^{250, 251}. Thus, the approach used in this study, including the preparation of erythrocyte membrane ghosts, cryo-specimen preparation, and the application of cryo-ET/StA techniques, it can be applied to studying the organization of the membrane skeleton in parasitized sickle cells. Such research could be compared to the cryo-EM structure of the membrane skeleton from parasitized normal RBCs, and may potentially uncover novel proteins that interact with the knob complex.

In summary, this work presents the first StA map of the 120-kDa NaChBac embedded in liposomes under a resting membrane potential, and the first cryo-EM structure of the supramolecular knob complex in *P. falciparum*-infected human erythrocyte. This thesis opens up several promising lines for future studies of membrane proteins *in vitro* and *in situ*, where other membrane proteins can be studied in physiologically relevant environments. Already with the present generation of cryo-EM hardware and software, this thesis represents pioneering research in the field of membrane protein structural biology.

Appendix

A. Detailed overview of the experimental conditions

A.1 Protein sequence (full-length *Bacillus halodurans* NaChBac, NP_242367)

1 mkmearqkqn sftskmqkiv nhrafftvi alilfnaliv gietypriya dhkwlfyrid
61 lvllwiftie iamrflasn ksaffrsw n wfdflivaag hifagaqfvt vlrlrvlr
121 lraivvpsl rrlvdalvmt ipalgnlil msiffyifav igtmlfqhvs peyfgnlqls
181 lltlfqvvtl eswasgvmrp ifaevpwwsl yfvsfvligt fiifnlfigv ivnnvekael
241 tdneedgead glkqeisalr kdvaelsll kqsk

A.2 Growth media

Luria-Bertani (LB): Bought from BD (Per liter: 10 g bacto-tryptone, 5 g yeast extract, 10 g NaCl) for DH5 α cells; supplemented with 1% glucose (w/v) for BL21 cells.

LB Agar: Bought from BD (Per liter: 10 g bacto-tryptone, 5 g yeast extract, 10 g NaCl, 15 g agar) for DH5 α cells; supplemented with 1% glucose (w/v) for BL21 cells.

SOC medium: Per liter: 20 g bacto-tryptone, 5 g yeast extract, 0.5 g NaCl, 2.5 mM KCl, 10 mM MgCl₂, 20 mM glucose, adjusted to pH 7.0.

2 \times YT: Per liter: 16 g peptone, 10 g yeast extract, 5 g NaCl, adjusted to pH 7.0.

TB medium: Per 900 mL, 12 g peptone, 24 g yeast extract, 4 mL glycerol, to which is added 100 mL 0.17 M KH₂PO₄, 0.72 M K₂HPO₄ (sterilised separately from rest of the medium).

A.3 Transforming *E. coli*

A 50 μ L aliquot of DH5 α (for site-directed mutagenesis) or BL21(DE3) (for expression) competent cells (Novagen), was incubated on ice with ~250 ng of plasmid DNA stock for 30 min. Cells were heat shocked (90 s at 42 $^{\circ}$ C) and placed on ice for 2 minutes. 500 μ L of SOC medium was added and the cells were subsequently incubated at 37 $^{\circ}$ C for 1 h. The culture was then plated onto LB agar plates supplemented with 100 μ g/mL ampicillin (Sigma-Aldrich), and 1% glucose (w/v) for the BL21 cells, and incubated overnight at 37 $^{\circ}$ C.

A.4 NaChBac purification

Protease inhibitors: Leupeptin, pepstatin A, aprotinin, at a final concentration of respectively 2 $\mu\text{g}/\text{mL}$, 2 $\mu\text{g}/\text{mL}$, and 3 $\mu\text{g}/\text{mL}$.

Resuspension buffer: 25 mM Tris, pH 8.5, 300 mM NaCl, protease inhibitors.

Extraction buffer: 25 mM Tris, pH 8.5, 300 mM NaCl, 20 mM imidazole, 1% (wt/vol) DDM.

Wash buffer 1: 25 mM Tris, pH 8.5, 300 mM NaCl, 20 mM imidazole, 0.1% DDM.

Wash buffer 2: 25 mM Tris, pH 8.5, 300 mM NaCl, 50 mM imidazole, 0.1% DDM.

Wash buffer 3: 25 mM Tris, pH 8.5, 300 mM NaCl, 80 mM imidazole, 0.1% DDM.

Elution: 25 mM Tris, pH 8.5, 300 mM NaCl, 250 mM imidazole, 0.1% DDM.

SEC buffer: 25 mM Tris, pH 8.5, 150 mM KCl, and 0.1% DDM.

A.5 SDS-PAGE

2 \times Sample buffer: 200 mM Tris-HCl (pH 8.8), 20% glycerol (v/v), 5 mM EDTA, 0.02% bromophenol blue (w/v). To a 700 μL aliquot, 200 μL 20% SDS (w/v) and 100 μL 0.5 M DTT is added before use.

Tris-Glycine SDS running buffer: 25 mM Tris pH 8.3, 192 mM Glycine, 0.1% SDS (w/v).

Coomassie Brilliant Blue staining solution: Coomassie Brilliant Blue R250 (0.25% w/v), methanol (45% v/v), MilliQ H₂O (45% v/v), glacial acetic acid (10% v/v).

Coomassie destain solution: Methanol (45% v/v), MilliQ H₂O (45% v/v), glacial acetic acid (10% v/v).

Proteins were using a pre-cast Tris-Glycine (12%, or 4-12%) (Invitrogen), using Tris-Glycine running buffer (150 V, 60 min). Protein samples were mixed 1:1 with 2 \times sample buffer, and denatured at ~ 100 °C for 3-5 minutes. For Coomassie staining, gels were incubated for 1 h Coomassie Brilliant Blue staining solution, and destained overnight with destaining solution.

B. NaChBac in liposomes

Table B.1 Data processing statistics

	NaChBac in liposomes
EMDB code	EMD-17163
EMPIAR code	EMPIAR-11576
Data collection and processing	
Microscope	Titan Krios G2
Magnification	81,000 ×
Voltage (kV), Cs	300 kV, 2.7 mm
Total electron dose ($e^-/\text{Å}^2$)	~130
Defocus range (μm)	-2.5 to -3.5
Camera	Gatan K3 + BioQuantum image filter
Pixel size (Å)	1.393
Number of tomograms	98
Symmetry imposed	C1
Initial particles	~86,000
Final particles	3,116
Refinement method	Independent half-set
Map resolution (Å)	16.3
FSC threshold	0.143

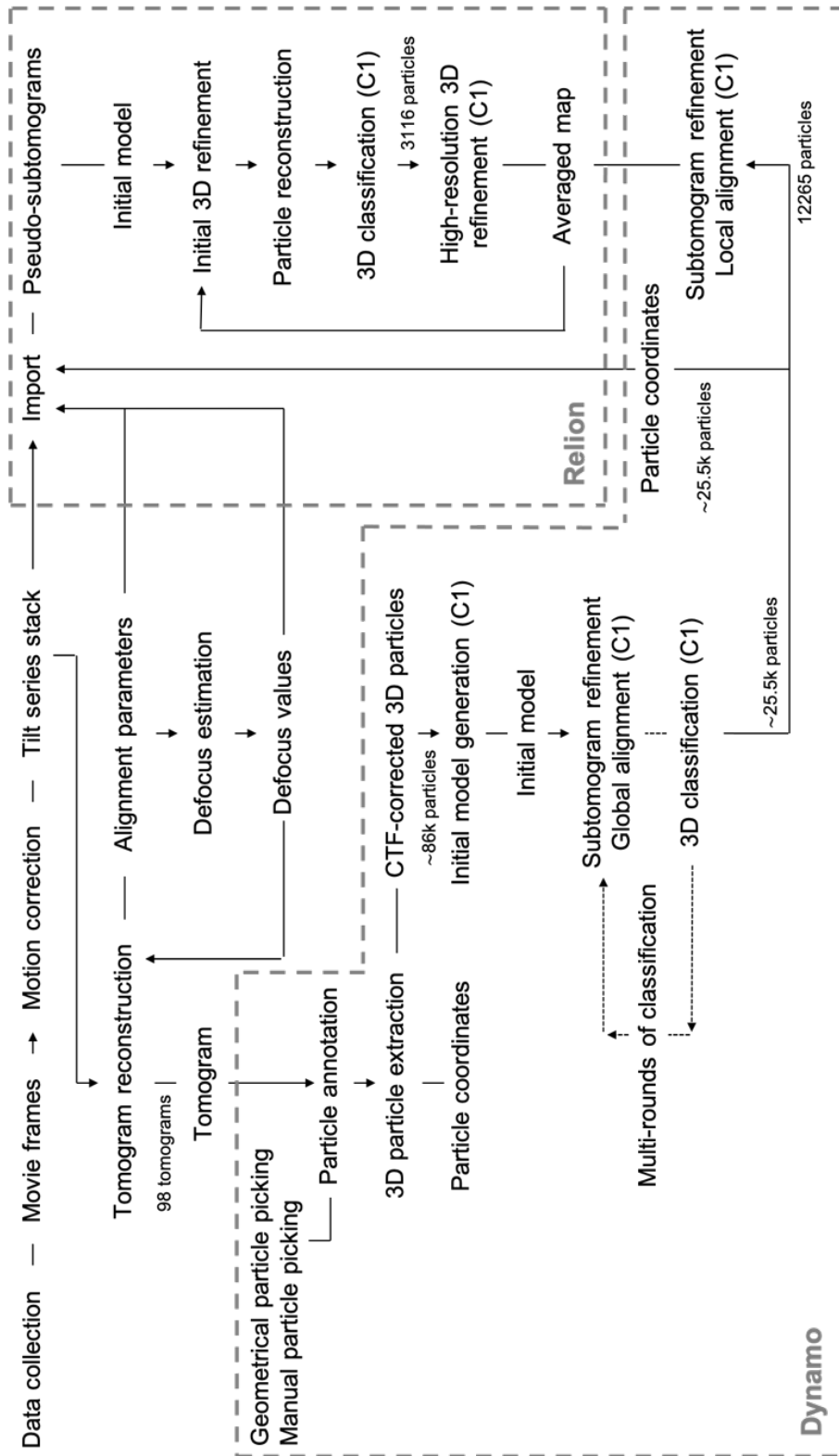


Figure B.1 Processing pipeline for tomogram reconstruction and subtomogram averaging.

Tilt series stack alignment, tomographic reconstruction, particle annotation, 3D classification, and subtomogram averaging were shown in the workflow.

C. Knob complex

Table C.1 Data processing statistics

	Knob complex
EMDB code	EMD-13192
Data collection and processing	
Microscope	Titan Krios G1
Magnification	42,000 ×
Voltage (kV), Cs	300 kV, 2.7 mm
Total electron dose ($e^-/\text{Å}^2$)	~110
Defocus range (μm)	-5 to -6
Camera	Gatan K2 + Quantum energy filter
Pixel size (Å)	3.39
Number of tomograms	55
Symmetry imposed	C1
Initial particles	489
Final particles	332
Refinement method	Independent half-set
Map resolution (Å)	31.3
FSC threshold	0.143

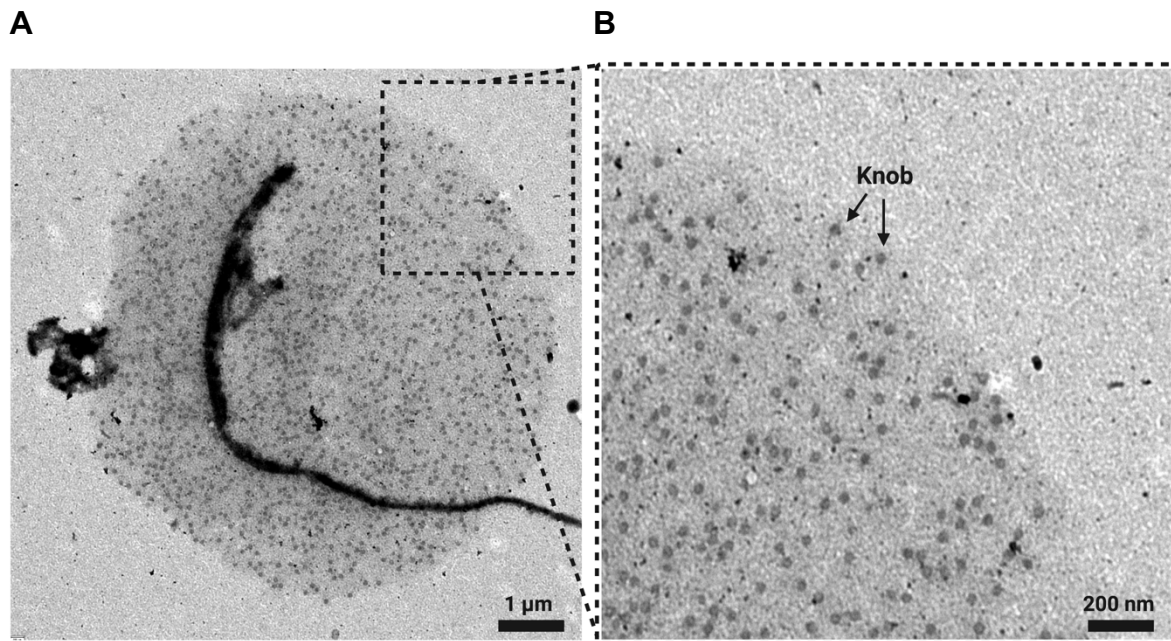


Figure C.1 Negative-staining image of erythrocyte ghost membrane. (A) An image of *P. falciparum*-infected erythrocyte ghost membrane. (B) A detailed view of the knob-rich erythrocyte ghost membrane. Images were provided by Dr. Cecilia Sanchez from the group of Prof. Dr. rer. nat. Michael Lanzer at Universitätsklinikum Heidelberg.

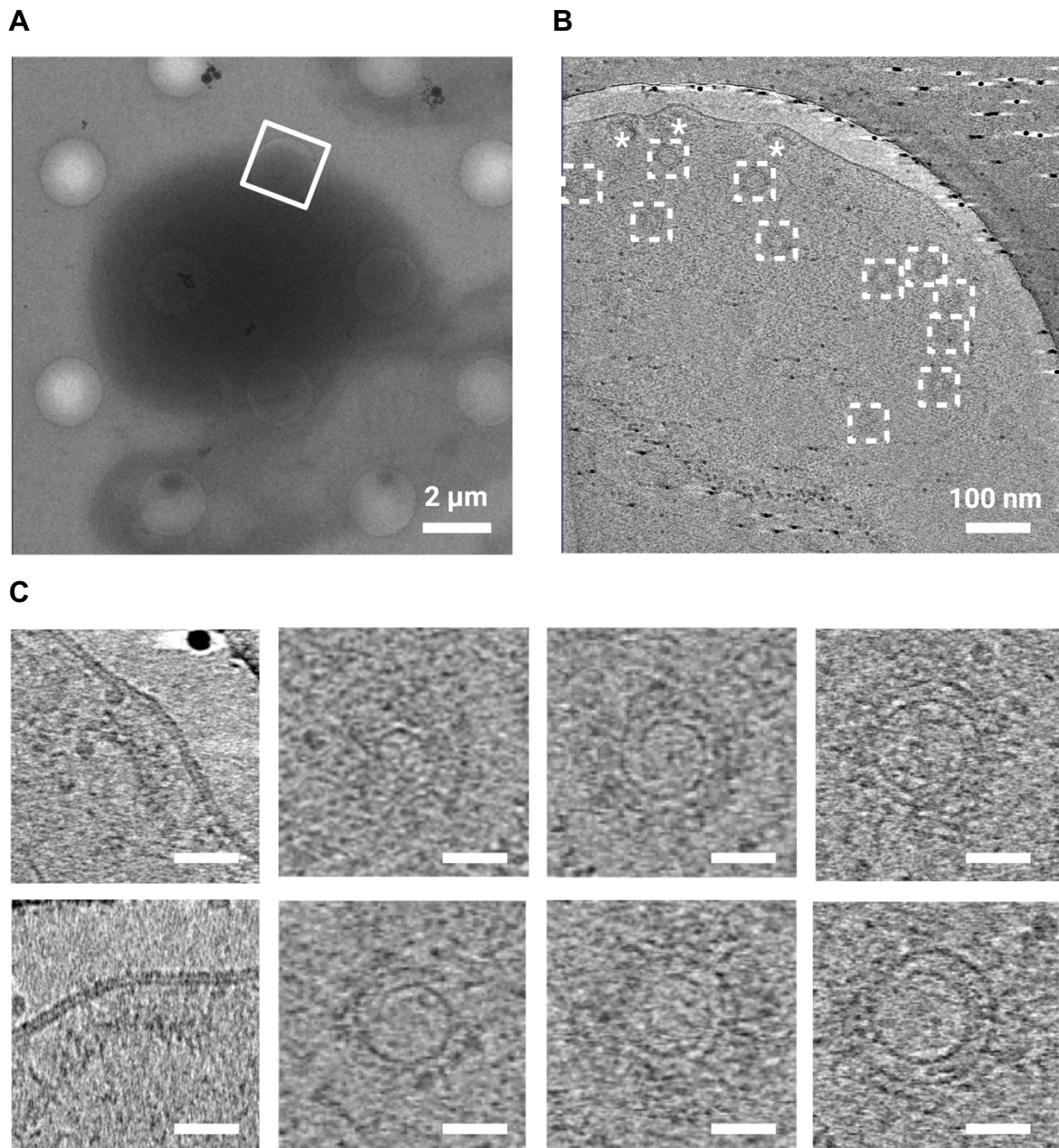


Figure C.2 Visualization of knob spirals in tomograms. (A) Low magnification cryo-image of a membrane ghost prepared from a trophozoite-infected erythrocyte. White square indicates an area for tilt-series acquisition. (B) A section through a tomogram showing knobs in top views (white squares) and side views (white asterisks). (C) The size of knobs varies. Scale bars: 20 nm.

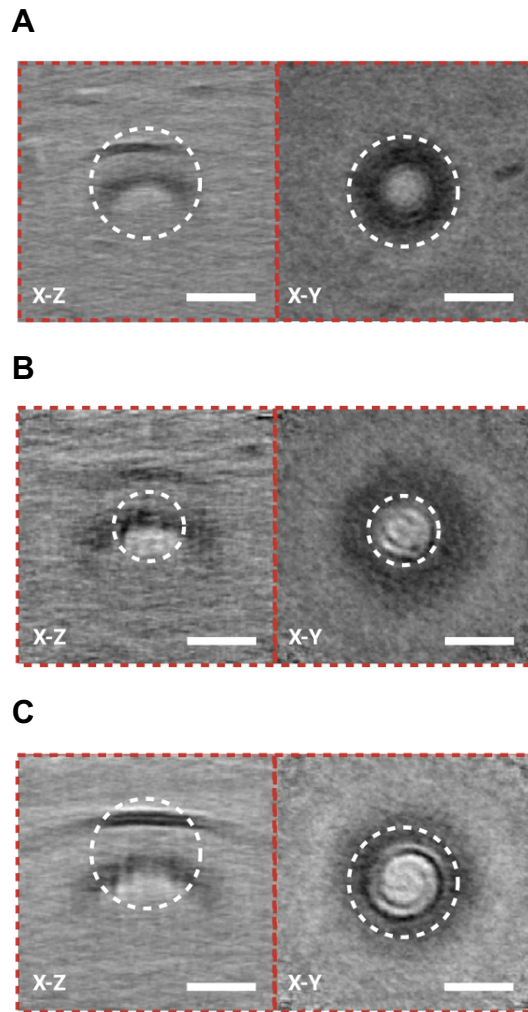
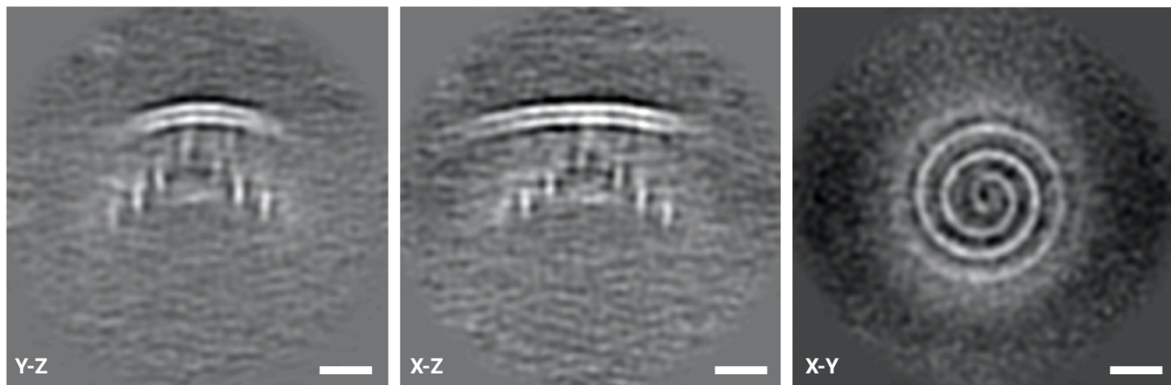


Figure C.3 Masks used for spiral alignment. (A) A large soft-edged sphere mask was applied to the entire knobs, resulting in a donut-like averaging result without features of knob spirals. (B) A smaller soft-edged sphere alignment mask was applied, and the particles were aligned against the core of knobs, revealing prominent spiral-like features under the lipid bilayer. (C) Refinements with a larger mask showed more detailed features of spirals. Scale bars: 20 nm.

A



B

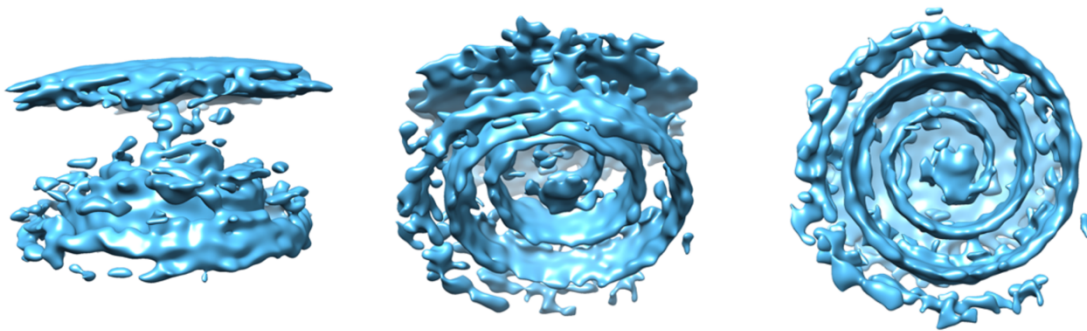


Figure C.4 StA and reconstruction of the knob complex. (A) StA map filtered to a resolution of 31 Å, scale bars: 20 nm. (B) Volume-rendered representation of the spiral and associated plasma membrane. Side, skew, and bottom views of the knob complex are shown.

References

1. Watson, H., Biological membranes. *Essays Biochem* **2015**, *59*, 43-69.
2. Sundelacruz, S.; Levin, M.; Kaplan, D. L., Role of membrane potential in the regulation of cell proliferation and differentiation. *Stem Cell Rev Rep* **2009**, *5* (3), 231-46.
3. Reiner, A.; Levitz, J., Glutamatergic Signaling in the Central Nervous System: Ionotropic and Metabotropic Receptors in Concert. *Neuron* **2018**, *98* (6), 1080-1098.
4. Hoyer, D.; Clarke, D. E.; Fozard, J. R.; Hartig, P. R.; Martin, G. R.; Mylecharane, E. J.; Saxena, P. R.; Humphrey, P. P., International Union of Pharmacology classification of receptors for 5-hydroxytryptamine (Serotonin). *Pharmacol Rev* **1994**, *46* (2), 157-203.
5. Herbst, R. S., Review of epidermal growth factor receptor biology. *Int J Radiat Oncol Biol Phys* **2004**, *59* (2 Suppl), 21-6.
6. Agre, P., The aquaporin water channels. *Proc Am Thorac Soc* **2006**, *3* (1), 5-13.
7. Skou, J. C.; Esmann, M., The Na,K-ATPase. *Journal of Bioenergetics and Biomembranes* **1992**, *24* (3), 249-261.
8. Yoshida, M.; Muneyuki, E.; Hisabori, T., ATP synthase — a marvellous rotary engine of the cell. *Nature Reviews Molecular Cell Biology* **2001**, *2* (9), 669-677.
9. Almén, M. S.; Nordström, K. J.; Fredriksson, R.; Schiöth, H. B., Mapping the human membrane proteome: a majority of the human membrane proteins can be classified according to function and evolutionary origin. *BMC Biology* **2009**, *7* (1), 50.
10. Overington, J. P.; Al-Lazikani, B.; Hopkins, A. L., How many drug targets are there? *Nat Rev Drug Discov* **2006**, *5* (12), 993-996.
11. Yildirim, M. A.; Goh, K. I.; Cusick, M. E.; Barabasi, A. L.; Vidal, M., Drug-target network. *Nat Biotechnol* **2007**, *25* (10), 1119-26.
12. Rask-Andersen, M.; Almen, M. S.; Schioth, H. B., Trends in the exploitation of novel drug targets. *Nat Rev Drug Discov* **2011**, *10* (8), 579-90.
13. Gulezian, E.; Crivello, C.; Bednenko, J.; Zafra, C.; Zhang, Y.; Colussi, P.; Hussain, S., Membrane protein production and formulation for drug discovery. *Trends Pharmacol Sci* **2021**, *42* (8), 657-674.
14. Cheng, Y., Single-Particle Cryo-EM at Crystallographic Resolution. *Cell* **2015**, *161* (3), 450-457.
15. Nogales, E.; Scheres, S. H., Cryo-EM: A Unique Tool for the Visualization of Macromolecular Complexity. *Mol Cell* **2015**, *58* (4), 677-89.

16. Robinson, C. V.; Sali, A.; Baumeister, W., The molecular sociology of the cell. *Nature* **2007**, *450* (7172), 973-82.
17. Briggs, J. A., Structural biology in situ--the potential of subtomogram averaging. *Curr Opin Struct Biol* **2013**, *23* (2), 261-7.
18. Fernandez-Leiro, R.; Scheres, S. H. W., Unravelling biological macromolecules with cryo-electron microscopy. *Nature* **2016**, *537* (7620), 339-346.
19. De Rosier, D. J.; Klug, A., Reconstruction of Three Dimensional Structures from Electron Micrographs. *Nature* **1968**, *217* (5124), 130-134.
20. Millonig, G.; Marinozzi, V., Fixation and embedding in electron microscopy. *Advances in optical and electron microscopy* **1968**, *2*, 251-341.
21. Dubochet, J.; Lepault, J.; Freeman, R.; Berriman, J. A.; Homo, J.-C., Electron microscopy of frozen water and aqueous solutions. *Journal of Microscopy* **1982**, *128* (3), 219-237.
22. Dubochet, J.; Adrian, M.; Chang, J. J.; Homo, J. C.; Lepault, J.; McDowell, A. W.; Schultz, P., Cryo-electron microscopy of vitrified specimens. *Q Rev Biophys* **1988**, *21* (2), 129-228.
23. Radermacher, M.; Wagenknecht, T.; Verschoor, A.; Frank, J., Three-dimensional reconstruction from a single-exposure, random conical tilt series applied to the 50S ribosomal subunit of Escherichia coli. *J Microsc* **1987**, *146* (Pt 2), 113-36.
24. Frank, J.; Radermacher, M.; Penczek, P.; Zhu, J.; Li, Y.; Ladjadj, M.; Leith, A., SPIDER and WEB: processing and visualization of images in 3D electron microscopy and related fields. *J Struct Biol* **1996**, *116* (1), 190-9.
25. Frank, J.; Goldfarb, W.; Eisenberg, D.; Baker, T. S., Reconstruction of glutamine synthetase using computer averaging. *Ultramicroscopy* **1978**, *3* (3), 283-90.
26. Henderson, R.; Unwin, P. N. T., Three-dimensional model of purple membrane obtained by electron microscopy. *Nature* **1975**, *257* (5521), 28-32.
27. Henderson, R.; Baldwin, J. M.; Ceska, T. A.; Zemlin, F.; Beckmann, E.; Downing, K. H., Model for the structure of bacteriorhodopsin based on high-resolution electron cryo-microscopy. *Journal of Molecular Biology* **1990**, *213* (4), 899-929.
28. Method of the Year 2015. *Nature Methods* **2016**, *13* (1), 1-1.
29. Fernandez-Leiro, R.; Scheres, S. H., Unravelling biological macromolecules with cryo-electron microscopy. *Nature* **2016**, *537* (7620), 339-46.
30. Noble, A. J.; Dandey, V. P.; Wei, H.; Brasch, J.; Chase, J.; Acharya, P.; Tan, Y. Z.; Zhang, Z.; Kim, L. Y.; Scapin, G.; Rapp, M.; Eng, E. T.; Rice, W. J.; Cheng, A.; Negro,

- C. J.; Shapiro, L.; Kwong, P. D.; Jeruzalmi, D.; des Georges, A.; Potter, C. S.; Carragher, B., Routine single particle CryoEM sample and grid characterization by tomography. *Elife* **2018**, *7*.
31. Cheng, Y.; Grigorieff, N.; Penczek, P. A.; Walz, T., A primer to single-particle cryo-electron microscopy. *Cell* **2015**, *161* (3), 438-449.
32. Kuhlbrandt, W., Biochemistry. The resolution revolution. *Science* **2014**, *343* (6178), 1443-4.
33. Ruskin, R. S.; Yu, Z.; Grigorieff, N., Quantitative characterization of electron detectors for transmission electron microscopy. *J Struct Biol* **2013**, *184* (3), 385-93.
34. McMullan, G.; Faruqi, A. R.; Clare, D.; Henderson, R., Comparison of optimal performance at 300keV of three direct electron detectors for use in low dose electron microscopy. *Ultramicroscopy* **2014**, *147*, 156-63.
35. Li, X.; Mooney, P.; Zheng, S.; Booth, C. R.; Braunfeld, M. B.; Gubbens, S.; Agard, D. A.; Cheng, Y., Electron counting and beam-induced motion correction enable near-atomic-resolution single-particle cryo-EM. *Nat Methods* **2013**, *10* (6), 584-90.
36. McMullan, G.; Chen, S.; Henderson, R.; Faruqi, A. R., Detective quantum efficiency of electron area detectors in electron microscopy. *Ultramicroscopy* **2009**, *109* (9), 1126-43.
37. Brilot, A. F.; Chen, J. Z.; Cheng, A.; Pan, J.; Harrison, S. C.; Potter, C. S.; Carragher, B.; Henderson, R.; Grigorieff, N., Beam-induced motion of vitrified specimen on holey carbon film. *J Struct Biol* **2012**, *177* (3), 630-7.
38. Scheres, S. H., A Bayesian view on cryo-EM structure determination. *J Mol Biol* **2012**, *415* (2), 406-18.
39. Scheres, S. H., RELION: implementation of a Bayesian approach to cryo-EM structure determination. *J Struct Biol* **2012**, *180* (3), 519-30.
40. Nogales, E., The development of cryo-EM into a mainstream structural biology technique. *Nat Methods* **2016**, *13* (1), 24-7.
41. Nakane, T.; Kotecha, A.; Sente, A.; McMullan, G.; Masiulis, S.; Brown, P.; Grigoras, I. T.; Malinauskaite, L.; Malinauskas, T.; Miehl, J.; Uchanski, T.; Yu, L.; Karia, D.; Pechnikova, E. V.; de Jong, E.; Keizer, J.; Bischoff, M.; McCormack, J.; Tiemeijer, P.; Hardwick, S. W.; Chirgadze, D. Y.; Murshudov, G.; Aricescu, A. R.; Scheres, S. H. W., Single-particle cryo-EM at atomic resolution. *Nature* **2020**, *587* (7832), 152-156.
42. Yip, K. M.; Fischer, N.; Paknia, E.; Chari, A.; Stark, H., Atomic-resolution protein structure determination by cryo-EM. *Nature* **2020**, *587* (7832), 157-161.

43. Wu, M.; Lander, G. C., How low can we go? Structure determination of small biological complexes using single-particle cryo-EM. *Curr Opin Struct Biol* **2020**, *64*, 9-16.
44. Merk, A.; Bartesaghi, A.; Banerjee, S.; Falconieri, V.; Rao, P.; Davis, M. I.; Pragani, R.; Boxer, M. B.; Earl, L. A.; Milne, J. L. S.; Subramaniam, S., Breaking Cryo-EM Resolution Barriers to Facilitate Drug Discovery. *Cell* **2016**, *165* (7), 1698-1707.
45. Zhang, K.; Li, S.; Kappel, K.; Pintilie, G.; Su, Z.; Mou, T. C.; Schmid, M. F.; Das, R.; Chiu, W., Cryo-EM structure of a 40 kDa SAM-IV riboswitch RNA at 3.7 Å resolution. *Nat Commun* **2019**, *10* (1), 5511.
46. Henderson, R., The potential and limitations of neutrons, electrons and X-rays for atomic resolution microscopy of unstained biological molecules. *Q Rev Biophys* **1995**, *28* (2), 171-93.
47. Harrison, P. J.; Vecerkova, T.; Clare, D. K.; Quigley, A., A review of the approaches used to solve sub-100 kDa membrane proteins by cryo-electron microscopy. *J Struct Biol* **2023**, *215* (2), 107959.
48. Rubinstein, J. L.; Guo, H.; Ripstein, Z. A.; Haydaroglu, A.; Au, A.; Yip, C. M.; Di Trani, J. M.; Benlekbir, S.; Kwok, T., Shake-it-off: a simple ultrasonic cryo-EM specimen-preparation device. *Acta Crystallogr D Struct Biol* **2019**, *75* (Pt 12), 1063-1070.
49. Razinkov, I.; Dandey, V.; Wei, H.; Zhang, Z.; Melnekoff, D.; Rice, W. J.; Wigge, C.; Potter, C. S.; Carragher, B., A new method for vitrifying samples for cryoEM. *J Struct Biol* **2016**, *195* (2), 190-198.
50. Dandey, V. P.; Wei, H.; Zhang, Z.; Tan, Y. Z.; Acharya, P.; Eng, E. T.; Rice, W. J.; Kahn, P. A.; Potter, C. S.; Carragher, B., Spotiton: New features and applications. *J Struct Biol* **2018**, *202* (2), 161-169.
51. Ravelli, R. B. G.; Nijpels, F. J. T.; Henderikx, R. J. M.; Weissenberger, G.; Thewessem, S.; Gijssbers, A.; Beulen, B.; Lopez-Iglesias, C.; Peters, P. J., Cryo-EM structures from sub-nl volumes using pin-printing and jet vitrification. *Nat Commun* **2020**, *11* (1), 2563.
52. Schwartz, O.; Axelrod, J. J.; Campbell, S. L.; Turnbaugh, C.; Glaeser, R. M.; Muller, H., Laser phase plate for transmission electron microscopy. *Nat Methods* **2019**, *16* (10), 1016-1020.
53. Zhong, E. D.; Bepler, T.; Berger, B.; Davis, J. H., CryoDRGN: reconstruction of heterogeneous cryo-EM structures using neural networks. *Nat Methods* **2021**, *18* (2), 176-185.
54. Kinman, L. F.; Powell, B. M.; Zhong, E. D.; Berger, B.; Davis, J. H., Uncovering structural ensembles from single-particle cryo-EM data using cryoDRGN. *Nat Protoc* **2023**, *18* (2), 319-339.

55. Turk, M.; Baumeister, W., The promise and the challenges of cryo-electron tomography. *FEBS Lett* **2020**, *594* (20), 3243-3261.
56. Chen, M.; Bell, J. M.; Shi, X.; Sun, S. Y.; Wang, Z.; Ludtke, S. J., A complete data processing workflow for cryo-ET and subtomogram averaging. *Nat Methods* **2019**, *16* (11), 1161-1168.
57. Jensen, G. J.; Briegel, A., How electron cryotomography is opening a new window onto prokaryotic ultrastructure. *Curr Opin Struct Biol* **2007**, *17* (2), 260-7.
58. Bauerlein, F. J. B.; Baumeister, W., Towards Visual Proteomics at High Resolution. *J Mol Biol* **2021**, *433* (20), 167187.
59. Berger, C.; Premaraj, N.; Ravelli, R. B. G.; Knoop, K.; Lopez-Iglesias, C.; Peters, P. J., Cryo-electron tomography on focused ion beam lamellae transforms structural cell biology. *Nat Methods* **2023**, *20* (4), 499-511.
60. Kukulski, W.; Schorb, M.; Welsch, S.; Picco, A.; Kaksonen, M.; Briggs, J. A., Correlated fluorescence and 3D electron microscopy with high sensitivity and spatial precision. *J Cell Biol* **2011**, *192* (1), 111-9.
61. Harapin, J.; Bormel, M.; Sapra, K. T.; Brunner, D.; Kaech, A.; Medalia, O., Structural analysis of multicellular organisms with cryo-electron tomography. *Nat Methods* **2015**, *12* (7), 634-6.
62. Mahamid, J.; Schampers, R.; Persoon, H.; Hyman, A. A.; Baumeister, W.; Plitzko, J. M., A focused ion beam milling and lift-out approach for site-specific preparation of frozen-hydrated lamellas from multicellular organisms. *J Struct Biol* **2015**, *192* (2), 262-9.
63. Marko, M.; Hsieh, C.; Schalek, R.; Frank, J.; Mannella, C., Focused-ion-beam thinning of frozen-hydrated biological specimens for cryo-electron microscopy. *Nat Methods* **2007**, *4* (3), 215-7.
64. Schaffer, M.; Pfeffer, S.; Mahamid, J.; Kleindiek, S.; Laugks, T.; Albert, S.; Engel, B. D.; Rummel, A.; Smith, A. J.; Baumeister, W.; Plitzko, J. M., A cryo-FIB lift-out technique enables molecular-resolution cryo-ET within native *Caenorhabditis elegans* tissue. *Nat Methods* **2019**, *16* (8), 757-762.
65. Arnold, J.; Mahamid, J.; Lucic, V.; de Marco, A.; Fernandez, J. J.; Laugks, T.; Mayer, T.; Hyman, A. A.; Baumeister, W.; Plitzko, J. M., Site-Specific Cryo-focused Ion Beam Sample Preparation Guided by 3D Correlative Microscopy. *Biophys J* **2016**, *110* (4), 860-9.

66. Wagner, F. R.; Watanabe, R.; Schampers, R.; Singh, D.; Persoon, H.; Schaffer, M.; Fruhstorfer, P.; Plitzko, J.; Villa, E., Preparing samples from whole cells using focused-ion-beam milling for cryo-electron tomography. *Nat Protoc* **2020**, *15* (6), 2041-2070.
67. Toro-Nahuelpan, M.; Zagoriy, I.; Senger, F.; Blanchoin, L.; Thery, M.; Mahamid, J., Tailoring cryo-electron microscopy grids by photo-micropatterning for in-cell structural studies. *Nat Methods* **2020**, *17* (1), 50-54.
68. Allegretti, M.; Zimmerli, C. E.; Rantos, V.; Wilfling, F.; Ronchi, P.; Fung, H. K. H.; Lee, C. W.; Hagen, W.; Turonova, B.; Karius, K.; Bormel, M.; Zhang, X.; Muller, C. W.; Schwab, Y.; Mahamid, J.; Pfander, B.; Kosinski, J.; Beck, M., In-cell architecture of the nuclear pore and snapshots of its turnover. *Nature* **2020**, *586* (7831), 796-800.
69. Zila, V.; Margiotta, E.; Turonova, B.; Muller, T. G.; Zimmerli, C. E.; Mattei, S.; Allegretti, M.; Borner, K.; Rada, J.; Muller, B.; Lusic, M.; Krausslich, H. G.; Beck, M., Cone-shaped HIV-1 capsids are transported through intact nuclear pores. *Cell* **2021**, *184* (4), 1032-1046 e18.
70. Zimmerli, C. E.; Allegretti, M.; Rantos, V.; Goetz, S. K.; Obarska-Kosinska, A.; Zagoriy, I.; Halavatyi, A.; Hummer, G.; Mahamid, J.; Kosinski, J.; Beck, M., Nuclear pores dilate and constrict in cellulose. *Science* **2021**, *374* (6573), eabd9776.
71. Mahamid, J.; Pfeffer, S.; Schaffer, M.; Villa, E.; Danev, R.; Cuellar, L. K.; Forster, F.; Hyman, A. A.; Plitzko, J. M.; Baumeister, W., Visualizing the molecular sociology at the HeLa cell nuclear periphery. *Science* **2016**, *351* (6276), 969-72.
72. Xue, L.; Lenz, S.; Zimmermann-Kogadeeva, M.; Tegunov, D.; Cramer, P.; Bork, P.; Rappilber, J.; Mahamid, J., Visualizing translation dynamics at atomic detail inside a bacterial cell. *Nature* **2022**, *610* (7930), 205-211.
73. Watanabe, R.; Buschauer, R.; Bohning, J.; Audagnotto, M.; Lasker, K.; Lu, T. W.; Boassa, D.; Taylor, S.; Villa, E., The In Situ Structure of Parkinson's Disease-Linked LRRK2. *Cell* **2020**, *182* (6), 1508-1518 e16.
74. Turonova, B.; Sikora, M.; Schurmann, C.; Hagen, W. J. H.; Welsch, S.; Blanc, F. E. C.; von Bulow, S.; Gecht, M.; Bagola, K.; Horner, C.; van Zandbergen, G.; Landry, J.; de Azevedo, N. T. D.; Mosalaganti, S.; Schwarz, A.; Covino, R.; Muhlebach, M. D.; Hummer, G.; Krijnse Locker, J.; Beck, M., In situ structural analysis of SARS-CoV-2 spike reveals flexibility mediated by three hinges. *Science* **2020**, *370* (6513), 203-208.
75. Wu, G. H.; Smith-Geater, C.; Galaz-Montoya, J. G.; Gu, Y.; Gupte, S. R.; Aviner, R.; Mitchell, P. G.; Hsu, J.; Miramontes, R.; Wang, K. Q.; Geller, N. R.; Hou, C.; Danita, C.; Joubert, L. M.; Schmid, M. F.; Yeung, S.; Frydman, J.; Mobley, W.; Wu, C.; Thompson,

- L. M.; Chiu, W., CryoET reveals organelle phenotypes in huntington disease patient iPSC-derived and mouse primary neurons. *Nat Commun* **2023**, *14* (1), 692.
76. Bharat, T. A. M.; Russo, C. J.; Lowe, J.; Passmore, L. A.; Scheres, S. H. W., Advances in Single-Particle Electron Cryomicroscopy Structure Determination applied to Sub-tomogram Averaging. *Structure* **2015**, *23* (9), 1743-1753.
77. Schur, F. K.; Hagen, W. J.; Rumlova, M.; Ruml, T.; Muller, B.; Krausslich, H. G.; Briggs, J. A., Structure of the immature HIV-1 capsid in intact virus particles at 8.8 Å resolution. *Nature* **2015**, *517* (7535), 505-8.
78. Schur, F. K.; Obr, M.; Hagen, W. J.; Wan, W.; Jakobi, A. J.; Kirkpatrick, J. M.; Sachse, C.; Krausslich, H. G.; Briggs, J. A., An atomic model of HIV-1 capsid-SP1 reveals structures regulating assembly and maturation. *Science* **2016**, *353* (6298), 506-8.
79. Turonova, B.; Schur, F. K. M.; Wan, W.; Briggs, J. A. G., Efficient 3D-CTF correction for cryo-electron tomography using NovaCTF improves subtomogram averaging resolution to 3.4Å. *J Struct Biol* **2017**, *199* (3), 187-195.
80. Tegunov, D.; Cramer, P., Real-time cryo-electron microscopy data preprocessing with Warp. *Nat Methods* **2019**, *16* (11), 1146-1152.
81. Tegunov, D.; Xue, L.; Dienemann, C.; Cramer, P.; Mahamid, J., Multi-particle cryo-EM refinement with M visualizes ribosome-antibiotic complex at 3.5 Å in cells. *Nat Methods* **2021**, *18* (2), 186-193.
82. Baumeister, W., Cryo-electron tomography: A long journey to the inner space of cells. *Cell* **2022**, *185* (15), 2649-2652.
83. Li, S.; Wang, Z.; Jia, X.; Niu, T.; Zhang, J.; Yin, G.; Zhang, X.; Zhu, Y.; Ji, G.; Sun, F., ELI trifocal microscope: a precise system to prepare target cryo-lamellae for in situ cryo-ET study. *Nat Methods* **2023**, *20* (2), 276-283.
84. Li, W.; Lu, J.; Xiao, K.; Zhou, M.; Li, Y.; Zhang, X.; Li, Z.; Gu, L.; Xu, X.; Guo, Q.; Xu, T.; Ji, W., Integrated multimodality microscope for accurate and efficient target-guided cryo-lamellae preparation. *Nat Methods* **2023**, *20* (2), 268-275.
85. Bouvette, J.; Liu, H. F.; Du, X.; Zhou, Y.; Sikkema, A. P.; da Fonseca Rezende, E. M. J.; Klemm, B. P.; Huang, R.; Schaaper, R. M.; Borgnia, M. J.; Bartesaghi, A., Beam image-shift accelerated data acquisition for near-atomic resolution single-particle cryo-electron tomography. *Nat Commun* **2021**, *12* (1), 1957.
86. de Teresa-Trueba, I.; Goetz, S. K.; Mattausch, A.; Stojanovska, F.; Zimmerli, C. E.; Toro-Nahuelpan, M.; Cheng, D. W. C.; Tollervey, F.; Pape, C.; Beck, M.; Diz-Munoz, A.;

- Kreshuk, A.; Mahamid, J.; Zaugg, J. B., Convolutional networks for supervised mining of molecular patterns within cellular context. *Nat Methods* **2023**, *20* (2), 284-294.
87. Moebel, E.; Martinez-Sanchez, A.; Lamm, L.; Righetto, R. D.; Wietrzynski, W.; Albert, S.; Lariviere, D.; Fourmentin, E.; Pfeffer, S.; Ortiz, J.; Baumeister, W.; Peng, T.; Engel, B. D.; Kervrann, C., Deep learning improves macromolecule identification in 3D cellular cryo-electron tomograms. *Nat Methods* **2021**, *18* (11), 1386-1394.
88. Liu, Y. T.; Zhang, H.; Wang, H.; Tao, C. L.; Bi, G. Q.; Zhou, Z. H., Isotropic reconstruction for electron tomography with deep learning. *Nat Commun* **2022**, *13* (1), 6482.
89. von Heijne, G., Membrane-protein topology. *Nat Rev Mol Cell Biol* **2006**, *7* (12), 909-18.
90. Abrahams, J. P.; Leslie, A. G.; Lutter, R.; Walker, J. E., Structure at 2.8 Å resolution of F1-ATPase from bovine heart mitochondria. *Nature* **1994**, *370* (6491), 621-8.
91. Doyle, D. A.; Morais Cabral, J.; Pfuetzner, R. A.; Kuo, A.; Gulbis, J. M.; Cohen, S. L.; Chait, B. T.; MacKinnon, R., The structure of the potassium channel: molecular basis of K⁺ conduction and selectivity. *Science* **1998**, *280* (5360), 69-77.
92. Landau, E. M.; Rosenbusch, J. P., Lipidic cubic phases: a novel concept for the crystallization of membrane proteins. *Proc Natl Acad Sci U S A* **1996**, *93* (25), 14532-5.
93. Pebay-Peyroula, E.; Rummel, G.; Rosenbusch, J. P.; Landau, E. M., X-ray structure of bacteriorhodopsin at 2.5 Å from microcrystals grown in lipidic cubic phases. *Science* **1997**, *277* (5332), 1676-81.
94. Cherezov, V.; Rosenbaum, D. M.; Hanson, M. A.; Rasmussen, S. G.; Thian, F. S.; Kobilka, T. S.; Choi, H. J.; Kuhn, P.; Weis, W. I.; Kobilka, B. K.; Stevens, R. C., High-resolution crystal structure of an engineered human beta2-adrenergic G protein-coupled receptor. *Science* **2007**, *318* (5854), 1258-65.
95. Arora, A.; Abildgaard, F.; Bushweller, J. H.; Tamm, L. K., Structure of outer membrane protein A transmembrane domain by NMR spectroscopy. *Nat Struct Biol* **2001**, *8* (4), 334-8.
96. Gautier, A.; Mott, H. R.; Bostock, M. J.; Kirkpatrick, J. P.; Nietlispach, D., Structure determination of the seven-helix transmembrane receptor sensory rhodopsin II by solution NMR spectroscopy. *Nat Struct Mol Biol* **2010**, *17* (6), 768-74.
97. Jaremko, L.; Jaremko, M.; Giller, K.; Becker, S.; Zweckstetter, M., Structure of the mitochondrial translocator protein in complex with a diagnostic ligand. *Science* **2014**, *343* (6177), 1363-6.

98. Shahid, S. A.; Bardiaux, B.; Franks, W. T.; Krabben, L.; Habeck, M.; van Rossum, B. J.; Linke, D., Membrane-protein structure determination by solid-state NMR spectroscopy of microcrystals. *Nat Methods* **2012**, *9* (12), 1212-7.
99. Wang, S.; Munro, R. A.; Shi, L.; Kawamura, I.; Okitsu, T.; Wada, A.; Kim, S. Y.; Jung, K. H.; Brown, L. S.; Ladizhansky, V., Solid-state NMR spectroscopy structure determination of a lipid-embedded heptahelical membrane protein. *Nat Methods* **2013**, *10* (10), 1007-12.
100. Liang, B.; Tamm, L. K., NMR as a tool to investigate the structure, dynamics and function of membrane proteins. *Nat Struct Mol Biol* **2016**, *23* (6), 468-74.
101. Yeh, V.; Goode, A.; Bonev, B. B., Membrane Protein Structure Determination and Characterisation by Solution and Solid-State NMR. *Biology (Basel)* **2020**, *9* (11).
102. Chapman, H. N.; Fromme, P.; Barty, A.; White, T. A.; Kirian, R. A.; Aquila, A.; Hunter, M. S.; Schulz, J.; DePonte, D. P.; Weierstall, U.; Doak, R. B.; Maia, F. R.; Martin, A. V.; Schlichting, I.; Lomb, L.; Coppola, N.; Shoeman, R. L.; Epp, S. W.; Hartmann, R.; Rolles, D.; Rudenko, A.; Foucar, L.; Kimmel, N.; Weidenspointner, G.; Holl, P.; Liang, M.; Barthelmess, M.; Caleman, C.; Boutet, S.; Bogan, M. J.; Krzywinski, J.; Bostedt, C.; Bajt, S.; Gumprecht, L.; Rudek, B.; Erk, B.; Schmidt, C.; Homke, A.; Reich, C.; Pietschner, D.; Struder, L.; Hauser, G.; Gorke, H.; Ullrich, J.; Herrmann, S.; Schaller, G.; Schopper, F.; Soltau, H.; Kuhnelt, K. U.; Messerschmidt, M.; Bozek, J. D.; Hau-Riege, S. P.; Frank, M.; Hampton, C. Y.; Sierra, R. G.; Starodub, D.; Williams, G. J.; Hajdu, J.; Timneanu, N.; Seibert, M. M.; Andreasson, J.; Rocker, A.; Jonsson, O.; Svenda, M.; Stern, S.; Nass, K.; Andritschke, R.; Schroter, C. D.; Krasniqi, F.; Bott, M.; Schmidt, K. E.; Wang, X.; Grotjohann, I.; Holton, J. M.; Barends, T. R.; Neutze, R.; Marchesini, S.; Fromme, R.; Schorb, S.; Rupp, D.; Adolph, M.; Gorkhover, T.; Andersson, I.; Hirsemann, H.; Potdevin, G.; Graafsma, H.; Nilsson, B.; Spence, J. C., Femtosecond X-ray protein nanocrystallography. *Nature* **2011**, *470* (7332), 73-7.
103. Boutet, S.; Lomb, L.; Williams, G. J.; Barends, T. R.; Aquila, A.; Doak, R. B.; Weierstall, U.; DePonte, D. P.; Steinbrener, J.; Shoeman, R. L.; Messerschmidt, M.; Barty, A.; White, T. A.; Kassemeyer, S.; Kirian, R. A.; Seibert, M. M.; Montanez, P. A.; Kenney, C.; Herbst, R.; Hart, P.; Pines, J.; Haller, G.; Gruner, S. M.; Philipp, H. T.; Tate, M. W.; Hromalik, M.; Koerner, L. J.; van Bakel, N.; Morse, J.; Ghonsalves, W.; Arnlund, D.; Bogan, M. J.; Caleman, C.; Fromme, R.; Hampton, C. Y.; Hunter, M. S.; Johansson, L. C.; Katona, G.; Kupitz, C.; Liang, M.; Martin, A. V.; Nass, K.; Redecke, L.; Stellato, F.; Timneanu, N.; Wang, D.; Zatsepin, N. A.; Schafer, D.; Defever, J.; Neutze, R.; Fromme, P.; Spence,

J. C.; Chapman, H. N.; Schlichting, I., High-resolution protein structure determination by serial femtosecond crystallography. *Science* **2012**, *337* (6092), 362-4.

104. Neutze, R.; Wouts, R.; van der Spoel, D.; Weckert, E.; Hajdu, J., Potential for biomolecular imaging with femtosecond X-ray pulses. *Nature* **2000**, *406* (6797), 752-7.

105. Gisriel, C.; Coe, J.; Letrun, R.; Yefanov, O. M.; Luna-Chavez, C.; Stander, N. E.; Lisova, S.; Mariani, V.; Kuhn, M.; Aplin, S.; Grant, T. D.; Dorner, K.; Sato, T.; Echelmeier, A.; Cruz Villarreal, J.; Hunter, M. S.; Wiedorn, M. O.; Knoska, J.; Mazalova, V.; Roy-Chowdhury, S.; Yang, J. H.; Jones, A.; Bean, R.; Bielecki, J.; Kim, Y.; Mills, G.; Weinhausen, B.; Meza, J. D.; Al-Qudami, N.; Bajt, S.; Brehm, G.; Botha, S.; Boukhelef, D.; Brockhauser, S.; Bruce, B. D.; Coleman, M. A.; Danilevski, C.; Discianno, E.; Dobson, Z.; Fangohr, H.; Martin-Garcia, J. M.; Gevorgov, Y.; Hauf, S.; Hosseinizadeh, A.; Januschek, F.; Ketawala, G. K.; Kupitz, C.; Maia, L.; Manetti, M.; Messerschmidt, M.; Michelat, T.; Mondal, J.; Ourmazd, A.; Previtali, G.; Sarrou, I.; Schon, S.; Schwander, P.; Shelby, M. L.; Silenzi, A.; Sztuk-Dambietz, J.; Szuba, J.; Turcato, M.; White, T. A.; Wrona, K.; Xu, C.; Abdellatif, M. H.; Zook, J. D.; Spence, J. C. H.; Chapman, H. N.; Barty, A.; Kirian, R. A.; Frank, M.; Ros, A.; Schmidt, M.; Fromme, R.; Mancuso, A. P.; Fromme, P.; Zatsepin, N. A., Membrane protein megahertz crystallography at the European XFEL. *Nat Commun* **2019**, *10* (1), 5021.

106. Molodenskiy, D. S.; Mertens, H. D. T.; Svergun, D. I., An automated data processing and analysis pipeline for transmembrane proteins in detergent solutions. *Sci Rep* **2020**, *10* (1), 8081.

107. Thangaratnarajah, C.; Rheinberger, J.; Paulino, C., Cryo-EM studies of membrane proteins at 200 keV. *Curr Opin Struct Biol* **2022**, *76*, 102440.

108. Kuhlbrandt, W.; Wang, D. N.; Fujiyoshi, Y., Atomic model of plant light-harvesting complex by electron crystallography. *Nature* **1994**, *367* (6464), 614-21.

109. Walz, T.; Hirai, T.; Murata, K.; Heymann, J. B.; Mitsuoka, K.; Fujiyoshi, Y.; Smith, B. L.; Agre, P.; Engel, A., The three-dimensional structure of aquaporin-1. *Nature* **1997**, *387* (6633), 624-7.

110. Hebert, H.; Schmidt-Krey, I.; Morgenstern, R.; Murata, K.; Hirai, T.; Mitsuoka, K.; Fujiyoshi, Y., The 3.0 Å projection structure of microsomal glutathione transferase as determined by electron crystallography of p 21212 two-dimensional crystals. *J Mol Biol* **1997**, *271* (5), 751-8.

111. Miyazawa, A.; Fujiyoshi, Y.; Stowell, M.; Unwin, N., Nicotinic acetylcholine receptor at 4.6 Å resolution: transverse tunnels in the channel wall. *J Mol Biol* **1999**, *288* (4), 765-86.

112. Miyazawa, A.; Fujiyoshi, Y.; Unwin, N., Structure and gating mechanism of the acetylcholine receptor pore. *Nature* **2003**, *423* (6943), 949-55.
113. Unwin, N., Refined structure of the nicotinic acetylcholine receptor at 4Å resolution. *J Mol Biol* **2005**, *346* (4), 967-89.
114. Seddon, A. M.; Curnow, P.; Booth, P. J., Membrane proteins, lipids and detergents: not just a soap opera. *Biochim Biophys Acta* **2004**, *1666* (1-2), 105-17.
115. Gewering, T.; Januliene, D.; Ries, A. B.; Moeller, A., Know your detergents: A case study on detergent background in negative stain electron microscopy. *J Struct Biol* **2018**, *203* (3), 242-246.
116. Tribet, C.; Audebert, R.; Popot, J. L., Amphipols: polymers that keep membrane proteins soluble in aqueous solutions. *Proc Natl Acad Sci U S A* **1996**, *93* (26), 15047-50.
117. Gorzelle, B. M.; Hoffman, A. K.; Keyes, M. H.; Gray, D. N.; Ray, D. G.; Sanders, C. R., Amphipols can support the activity of a membrane enzyme. *J Am Chem Soc* **2002**, *124* (39), 11594-5.
118. Ritchie, T. K.; Grinkova, Y. V.; Bayburt, T. H.; Denisov, I. G.; Zolnerciks, J. K.; Atkins, W. M.; Sligar, S. G., Chapter 11 - Reconstitution of membrane proteins in phospholipid bilayer nanodiscs. *Methods Enzymol* **2009**, *464*, 211-31.
119. Frauenfeld, J.; Loving, R.; Armache, J. P.; Sonnen, A. F.; Guettou, F.; Moberg, P.; Zhu, L.; Jegerschold, C.; Flayhan, A.; Briggs, J. A.; Garoff, H.; Low, C.; Cheng, Y.; Nordlund, P., A saposin-lipoprotein nanoparticle system for membrane proteins. *Nat Methods* **2016**, *13* (4), 345-51.
120. Knowles, T. J.; Finka, R.; Smith, C.; Lin, Y. P.; Dafforn, T.; Overduin, M., Membrane proteins solubilized intact in lipid containing nanoparticles bounded by styrene maleic acid copolymer. *J Am Chem Soc* **2009**, *131* (22), 7484-5.
121. Denisov, I. G.; Sligar, S. G., Nanodiscs for structural and functional studies of membrane proteins. *Nat Struct Mol Biol* **2016**, *23* (6), 481-6.
122. Flayhan, A.; Mertens, H. D. T.; Ural-Blimke, Y.; Martinez Molledo, M.; Svergun, D. I.; Low, C., Saposin Lipid Nanoparticles: A Highly Versatile and Modular Tool for Membrane Protein Research. *Structure* **2018**, *26* (2), 345-355 e5.
123. Dorr, J. M.; Scheidelaar, S.; Koorengevel, M. C.; Dominguez, J. J.; Schafer, M.; van Walree, C. A.; Killian, J. A., The styrene-maleic acid copolymer: a versatile tool in membrane research. *Eur Biophys J* **2016**, *45* (1), 3-21.
124. Gao, Y.; Cao, E.; Julius, D.; Cheng, Y., TRPV1 structures in nanodiscs reveal mechanisms of ligand and lipid action. *Nature* **2016**, *534* (7607), 347-51.

125. Cao, E.; Liao, M.; Cheng, Y.; Julius, D., TRPV1 structures in distinct conformations reveal activation mechanisms. *Nature* **2013**, *504* (7478), 113-8.
126. Liao, M.; Cao, E.; Julius, D.; Cheng, Y., Structure of the TRPV1 ion channel determined by electron cryo-microscopy. *Nature* **2013**, *504* (7478), 107-12.
127. Zhou, H. X.; Cross, T. A., Influences of membrane mimetic environments on membrane protein structures. *Annu Rev Biophys* **2013**, *42*, 361-92.
128. Rigaud, J. L.; Levy, D., Reconstitution of membrane proteins into liposomes. *Methods Enzymol* **2003**, *372*, 65-86.
129. Sejwal, K.; Chami, M.; Baumgartner, P.; Kowal, J.; Müller, S. A.; Stahlberg, H., Proteoliposomes – a system to study membrane proteins under buffer gradients by cryo-EM. *Nanotechnology Reviews* **2017**, *6* (1), 57-74.
130. Bai, X. C.; Yan, Z.; Wu, J.; Li, Z.; Yan, N., The Central domain of RyR1 is the transducer for long-range allosteric gating of channel opening. *Cell Res* **2016**, *26* (9), 995-1006.
131. Wei, R.; Wang, X.; Zhang, Y.; Mukherjee, S.; Zhang, L.; Chen, Q.; Huang, X.; Jing, S.; Liu, C.; Li, S.; Wang, G.; Xu, Y.; Zhu, S.; Williams, A. J.; Sun, F.; Yin, C. C., Structural insights into Ca(2+)-activated long-range allosteric channel gating of RyR1. *Cell Res* **2016**, *26* (9), 977-94.
132. des Georges, A.; Clarke, O. B.; Zalk, R.; Yuan, Q.; Condon, K. J.; Grassucci, R. A.; Hendrickson, W. A.; Marks, A. R.; Frank, J., Structural Basis for Gating and Activation of RyR1. *Cell* **2016**, *167* (1), 145-157 e17.
133. Zalk, R.; Clarke, O. B.; des Georges, A.; Grassucci, R. A.; Reiken, S.; Mancina, F.; Hendrickson, W. A.; Frank, J.; Marks, A. R., Structure of a mammalian ryanodine receptor. *Nature* **2015**, *517* (7532), 44-9.
134. Efremov, R. G.; Leitner, A.; Aebersold, R.; Raunser, S., Architecture and conformational switch mechanism of the ryanodine receptor. *Nature* **2015**, *517* (7532), 39-43.
135. Melville, Z.; Kim, K.; Clarke, O. B.; Marks, A. R., High-resolution structure of the membrane-embedded skeletal muscle ryanodine receptor. *Structure* **2022**, *30* (1), 172-180 e3.
136. Tao, X.; Zhao, C.; MacKinnon, R., Membrane protein isolation and structure determination in cell-derived membrane vesicles. *Proc Natl Acad Sci U S A* **2023**, *120* (18), e2302325120.
137. Strack, R., Structures in situ. *Nat Methods* **2020**, *17* (1), 21.
138. Muhleip, A. W.; Dewar, C. E.; Schnauffer, A.; Kuhlbrandt, W.; Davies, K. M., In situ structure of trypanosomal ATP synthase dimer reveals a unique arrangement of catalytic subunits. *Proc Natl Acad Sci U S A* **2017**, *114* (5), 992-997.

139. Davies, K. M.; Blum, T. B.; Kuhlbrandt, W., Conserved in situ arrangement of complex I and III(2) in mitochondrial respiratory chain supercomplexes of mammals, yeast, and plants. *Proc Natl Acad Sci U S A* **2018**, *115* (12), 3024-3029.
140. Rapisarda, C.; Cherrak, Y.; Kooger, R.; Schmidt, V.; Pellarin, R.; Logger, L.; Cascales, E.; Pilhofer, M.; Durand, E.; Fronzes, R., In situ and high-resolution cryo-EM structure of a bacterial type VI secretion system membrane complex. *EMBO J* **2019**, *38* (10).
141. Floris, D.; Kuhlbrandt, W., Molecular landscape of etioplast inner membranes in higher plants. *Nat Plants* **2021**, *7* (4), 514-523.
142. Chen, W.; Kudryashev, M., Structure of RyR1 in native membranes. *EMBO Rep* **2020**, *21* (5), e49891.
143. Sanchez, R. M.; Zhang, Y.; Chen, W.; Dietrich, L.; Kudryashev, M., Subnanometer-resolution structure determination in situ by hybrid subtomogram averaging - single particle cryo-EM. *Nat Commun* **2020**, *11* (1), 3709.
144. Gao, S.; Valinsky, W. C.; On, N. C.; Houlihan, P. R.; Qu, Q.; Liu, L.; Pan, X.; Clapham, D. E.; Yan, N., Employing NaChBac for cryo-EM analysis of toxin action on voltage-gated Na(+) channels in nanodisc. *Proc Natl Acad Sci U S A* **2020**, *117* (25), 14187-14193.
145. Watermeyer, J. M.; Hale, V. L.; Hackett, F.; Clare, D. K.; Cutts, E. E.; Vakonakis, I.; Fleck, R. A.; Blackman, M. J.; Saibil, H. R., A spiral scaffold underlies cytoadherent knobs in Plasmodium falciparum-infected erythrocytes. *Blood* **2016**, *127* (3), 343-51.
146. Bezanilla, F., How membrane proteins sense voltage. *Nat Rev Mol Cell Biol* **2008**, *9* (4), 323-32.
147. Hodgkin, A. L.; Huxley, A. F., Action Potentials Recorded from Inside a Nerve Fibre. *Nature* **1939**, *144* (3651), 710-711.
148. Hodgkin, A. L.; Huxley, A. F., Resting and action potentials in single nerve fibres. *J Physiol* **1945**, *104* (2), 176-95.
149. Yarov-Yarovoy, V.; DeCaen, P. G.; Westenbroek, R. E.; Pan, C. Y.; Scheuer, T.; Baker, D.; Catterall, W. A., Structural basis for gating charge movement in the voltage sensor of a sodium channel. *Proc Natl Acad Sci U S A* **2012**, *109* (2), E93-102.
150. Lenaeus, M. J.; Gamal El-Din, T. M.; Ing, C.; Ramanadane, K.; Pomes, R.; Zheng, N.; Catterall, W. A., Structures of closed and open states of a voltage-gated sodium channel. *Proc Natl Acad Sci U S A* **2017**, *114* (15), E3051-E3060.
151. Catterall, W. A.; Wisedchaisri, G.; Zheng, N., The conformational cycle of a prototypical voltage-gated sodium channel. *Nat Chem Biol* **2020**, *16* (12), 1314-1320.

152. Charalambous, K.; Wallace, B. A., NaChBac: the long lost sodium channel ancestor. *Biochemistry* **2011**, *50* (32), 6742-52.
153. McCusker, E. C.; Bagnieris, C.; Naylor, C. E.; Cole, A. R.; D'Avanzo, N.; Nichols, C. G.; Wallace, B. A., Structure of a bacterial voltage-gated sodium channel pore reveals mechanisms of opening and closing. *Nat Commun* **2012**, *3*, 1102.
154. Sula, A.; Booker, J.; Ng, L. C.; Naylor, C. E.; DeCaen, P. G.; Wallace, B. A., The complete structure of an activated open sodium channel. *Nat Commun* **2017**, *8*, 14205.
155. Payandeh, J.; Scheuer, T.; Zheng, N.; Catterall, W. A., The crystal structure of a voltage-gated sodium channel. *Nature* **2011**, *475* (7356), 353-8.
156. Yan, Z.; Zhou, Q.; Wang, L.; Wu, J.; Zhao, Y.; Huang, G.; Peng, W.; Shen, H.; Lei, J.; Yan, N., Structure of the Na(v)1.4- β 1 Complex from Electric Eel. *Cell* **2017**, *170* (3), 470-482.e11.
157. Pan, X.; Li, Z.; Zhou, Q.; Shen, H.; Wu, K.; Huang, X.; Chen, J.; Zhang, J.; Zhu, X.; Lei, J.; Xiong, W.; Gong, H.; Xiao, B.; Yan, N., Structure of the human voltage-gated sodium channel Na(v)1.4 in complex with β 1. *Science* **2018**, *362* (6412).
158. Shen, H.; Zhou, Q.; Pan, X.; Li, Z.; Wu, J.; Yan, N., Structure of a eukaryotic voltage-gated sodium channel at near-atomic resolution. *Science* **2017**, *355* (6328).
159. Wisedchaisri, G.; Tonggu, L.; McCord, E.; Gamal El-Din, T. M.; Wang, L.; Zheng, N.; Catterall, W. A., Resting-State Structure and Gating Mechanism of a Voltage-Gated Sodium Channel. *Cell* **2019**, *178* (4), 993-1003 e12.
160. Wisedchaisri, G.; Tonggu, L.; Gamal El-Din, T. M.; McCord, E.; Zheng, N.; Catterall, W. A., Structural Basis for High-Affinity Trapping of the Na(V)1.7 Channel in Its Resting State by Tarantula Toxin. *Mol Cell* **2021**, *81* (1), 38-48 e4.
161. Mandala, V. S.; MacKinnon, R., Voltage-sensor movements in the Eag Kv channel under an applied electric field. *Proc Natl Acad Sci U S A* **2022**, *119* (46), e2214151119.
162. Mandala, V. S.; MacKinnon, R., The membrane electric field regulates the PIP(2)-binding site to gate the KCNQ1 channel. *Proc Natl Acad Sci U S A* **2023**, *120* (21), e2301985120.
163. Geertsma, E. R.; Nik Mahmood, N. A.; Schuurman-Wolters, G. K.; Poolman, B., Membrane reconstitution of ABC transporters and assays of translocator function. *Nat Protoc* **2008**, *3* (2), 256-66.
164. Chanda, B.; Mathew, M. K., Functional reconstitution of bacterially expressed human potassium channels in proteoliposomes: membrane potential measurements with JC-1 to assay ion channel activity. *Biochim Biophys Acta* **1999**, *1416* (1-2), 92-100.

165. Smiley, S. T.; Reers, M.; Mottola-Hartshorn, C.; Lin, M.; Chen, A.; Smith, T. W.; Steele, G. D., Jr.; Chen, L. B., Intracellular heterogeneity in mitochondrial membrane potentials revealed by a J-aggregate-forming lipophilic cation JC-1. *Proc Natl Acad Sci U S A* **1991**, *88* (9), 3671-5.
166. Reers, M.; Smith, T. W.; Chen, L. B., J-aggregate formation of a carbocyanine as a quantitative fluorescent indicator of membrane potential. *Biochemistry* **1991**, *30* (18), 4480-6.
167. Rose, L.; Jenkins, A. T., The effect of the ionophore valinomycin on biomimetic solid supported lipid DPPTE/EPC membranes. *Bioelectrochemistry* **2007**, *70* (2), 387-93.
168. Wang, L.; Sigworth, F. J., Structure of the BK potassium channel in a lipid membrane from electron cryomicroscopy. *Nature* **2009**, *461* (7261), 292-5.
169. Tonggu, L.; Wang, L., Structure of the Human BK Ion Channel in Lipid Environment. *Membranes (Basel)* **2022**, *12* (8).
170. Yao, X.; Fan, X.; Yan, N., Cryo-EM analysis of a membrane protein embedded in the liposome. *Proc Natl Acad Sci U S A* **2020**, *117* (31), 18497-18503.
171. Yang, X.; Lin, C.; Chen, X.; Li, S.; Li, X.; Xiao, B., Structure deformation and curvature sensing of PIEZO1 in lipid membranes. *Nature* **2022**, *604* (7905), 377-383.
172. Eibauer, M.; Hoffmann, C.; Plitzko, J. M.; Baumeister, W.; Nickell, S.; Engelhardt, H., Unraveling the structure of membrane proteins in situ by transfer function corrected cryo-electron tomography. *J Struct Biol* **2012**, *180* (3), 488-96.
173. Kudryashev, M.; Castano-Diez, D.; Deluz, C.; Hassaine, G.; Grasso, L.; Graf-Meyer, A.; Vogel, H.; Stahlberg, H., The Structure of the Mouse Serotonin 5-HT₃ Receptor in Lipid Vesicles. *Structure* **2016**, *24* (1), 165-170.
174. Rigaud, J. L.; Levy, D.; Mosser, G.; Lambert, O., Detergent removal by non-polar polystyrene beads. *European Biophysics Journal* **1998**, *27* (4), 305-319.
175. Coombs, D. H.; Watts, N. R., Generating sucrose gradients in three minutes by tilted tube rotation. *Anal Biochem* **1985**, *148* (1), 254-9.
176. Russo, C. J.; Passmore, L. A., Electron microscopy: Ultrastable gold substrates for electron cryomicroscopy. *Science* **2014**, *346* (6215), 1377-80.
177. Russo, C. J.; Passmore, L. A., Ultrastable gold substrates: Properties of a support for high-resolution electron cryomicroscopy of biological specimens. *J Struct Biol* **2016**, *193* (1), 33-44.
178. Punjani, A.; Rubinstein, J. L.; Fleet, D. J.; Brubaker, M. A., cryoSPARC: algorithms for rapid unsupervised cryo-EM structure determination. *Nat Methods* **2017**, *14* (3), 290-296.

179. Bepler, T.; Morin, A.; Rapp, M.; Brasch, J.; Shapiro, L.; Noble, A. J.; Berger, B., Positive-unlabeled convolutional neural networks for particle picking in cryo-electron micrographs. *Nat Methods* **2019**, *16* (11), 1153-1160.
180. Schorb, M.; Haberbosch, I.; Hagen, W. J. H.; Schwab, Y.; Mastronarde, D. N., Software tools for automated transmission electron microscopy. *Nat Methods* **2019**, *16* (6), 471-477.
181. Hagen, W. J. H.; Wan, W.; Briggs, J. A. G., Implementation of a cryo-electron tomography tilt-scheme optimized for high resolution subtomogram averaging. *J Struct Biol* **2017**, *197* (2), 191-198.
182. Balyschew, N.; Yushkevich, A.; Mikirtumov, V.; Sanchez, R.; Sprink, T.; Kudryashev, M., *Streamlined Structure Determination by Cryo-Electron Tomography and Subtomogram Averaging using TomoBEAR*. 2023.
183. Zheng, S. Q.; Palovcak, E.; Armache, J. P.; Verba, K. A.; Cheng, Y.; Agard, D. A., MotionCor2: anisotropic correction of beam-induced motion for improved cryo-electron microscopy. *Nat Methods* **2017**, *14* (4), 331-332.
184. Kremer, J. R.; Mastronarde, D. N.; McIntosh, J. R., Computer visualization of three-dimensional image data using IMOD. *J Struct Biol* **1996**, *116* (1), 71-6.
185. Mastronarde, D. N.; Held, S. R., Automated tilt series alignment and tomographic reconstruction in IMOD. *J Struct Biol* **2017**, *197* (2), 102-113.
186. Zhang, K., Gctf: Real-time CTF determination and correction. *J Struct Biol* **2016**, *193* (1), 1-12.
187. Castano-Diez, D.; Kudryashev, M.; Stahlberg, H., Dynamo Catalogue: Geometrical tools and data management for particle picking in subtomogram averaging of cryo-electron tomograms. *J Struct Biol* **2017**, *197* (2), 135-144.
188. Zivanov, J.; Oton, J.; Ke, Z.; von Kugelgen, A.; Pyle, E.; Qu, K.; Morado, D.; Castano-Diez, D.; Zanetti, G.; Bharat, T. A. M.; Briggs, J. A. G.; Scheres, S. H. W., A Bayesian approach to single-particle electron cryo-tomography in RELION-4.0. *Elife* **2022**, *11*.
189. Snijder, J.; Borst, A. J.; Dosey, A.; Walls, A. C.; Burrell, A.; Reddy, V. S.; Kollman, J. M.; Veessler, D., Vitrification after multiple rounds of sample application and blotting improves particle density on cryo-electron microscopy grids. *J Struct Biol* **2017**, *198* (1), 38-42.
190. Tonggu, L.; Wang, L., Cryo-EM sample preparation method for extremely low concentration liposomes. *Ultramicroscopy* **2020**, *208*, 112849.

191. Xu, H.; Li, T.; Rohou, A.; Arthur, C. P.; Tzakoniati, F.; Wong, E.; Estevez, A.; Kugel, C.; Franke, Y.; Chen, J.; Ciferri, C.; Hackos, D. H.; Koth, C. M.; Payandeh, J., Structural Basis of Nav1.7 Inhibition by a Gating-Modifier Spider Toxin. *Cell* **2019**, *176* (4), 702-715.e14.
192. Wu, S.; Avila-Sakar, A.; Kim, J.; Booth, D. S.; Greenberg, C. H.; Rossi, A.; Liao, M.; Li, X.; Alian, A.; Griner, S. L.; Juge, N.; Yu, Y.; Mergel, C. M.; Chaparro-Riggers, J.; Strop, P.; Tampe, R.; Edwards, R. H.; Stroud, R. M.; Craik, C. S.; Cheng, Y., Fabs enable single particle cryoEM studies of small proteins. *Structure* **2012**, *20* (4), 582-92.
193. Wu, X.; Rapoport, T. A., Cryo-EM structure determination of small proteins by nanobody-binding scaffolds (Legobodies). *Proc Natl Acad Sci U S A* **2021**, *118* (41).
194. Schachter, I.; Allolio, C.; Khelashvili, G.; Harries, D., Confinement in Nanodiscs Anisotropically Modifies Lipid Bilayer Elastic Properties. *J Phys Chem B* **2020**, *124* (33), 7166-7175.
195. Dalal, V.; Arcario, M.; Petroff, J.; Dietzen, N.; Rau, M.; Fitzpatrick, J.; Brannigan, G.; Cheng, W., Lipid nanodisc scaffold and size alters the structure of a pentameric ligand-gated ion channel. bioRxiv: 2022.
196. Jensen, M. O.; Jogini, V.; Borhani, D. W.; Leffler, A. E.; Dror, R. O.; Shaw, D. E., Mechanism of voltage gating in potassium channels. *Science* **2012**, *336* (6078), 229-33.
197. Organization, W. H., *World malaria report 2022*. World Health Organization: 2022.
198. Greenwood, B. M.; Bojang, K.; Whitty, C. J.; Targett, G. A., Malaria. *Lancet* **2005**, *365* (9469), 1487-98.
199. Snow, R. W.; Guerra, C. A.; Noor, A. M.; Myint, H. Y.; Hay, S. I., The global distribution of clinical episodes of Plasmodium falciparum malaria. *Nature* **2005**, *434* (7030), 214-7.
200. Schneider, V. M.; Visone, J. E.; Harris, C. T.; Florini, F.; Hadjimichael, E.; Zhang, X.; Gross, M. R.; Rhee, K. Y.; Ben Mamoun, C.; Kafsack, B. F. C.; Deitsch, K. W., The human malaria parasite Plasmodium falciparum can sense environmental changes and respond by antigenic switching. *Proc Natl Acad Sci U S A* **2023**, *120* (17), e2302152120.
201. Maier, A. G.; Cooke, B. M.; Cowman, A. F.; Tilley, L., Malaria parasite proteins that remodel the host erythrocyte. *Nat Rev Microbiol* **2009**, *7* (5), 341-54.
202. Su, X. Z.; Heatwole, V. M.; Wertheimer, S. P.; Guinet, F.; Herrfeldt, J. A.; Peterson, D. S.; Ravetch, J. A.; Wellems, T. E., The large diverse gene family var encodes proteins involved in cytoadherence and antigenic variation of Plasmodium falciparum-infected erythrocytes. *Cell* **1995**, *82* (1), 89-100.

203. Baruch, D. I.; Pasloske, B. L.; Singh, H. B.; Bi, X.; Ma, X. C.; Feldman, M.; Taraschi, T. F.; Howard, R. J., Cloning the P. falciparum gene encoding PfEMP1, a malarial variant antigen and adherence receptor on the surface of parasitized human erythrocytes. *Cell* **1995**, *82* (1), 77-87.
204. Smith, J. D.; Chitnis, C. E.; Craig, A. G.; Roberts, D. J.; Hudson-Taylor, D. E.; Peterson, D. S.; Pinches, R.; Newbold, C. I.; Miller, L. H., Switches in expression of Plasmodium falciparum var genes correlate with changes in antigenic and cytoadherent phenotypes of infected erythrocytes. *Cell* **1995**, *82* (1), 101-110.
205. Blank, A.; Furle, K.; Jaschke, A.; Mikus, G.; Lehmann, M.; Husing, J.; Heiss, K.; Giese, T.; Carter, D.; Bohnlein, E.; Lanzer, M.; Haefeli, W. E.; Bujard, H., Immunization with full-length Plasmodium falciparum merozoite surface protein 1 is safe and elicits functional cytophilic antibodies in a randomized first-in-human trial. *NPJ Vaccines* **2020**, *5* (1), 10.
206. Dijkman, P. M.; Marzluf, T.; Zhang, Y.; Chang, S. S.; Helm, D.; Lanzer, M.; Bujard, H.; Kudryashev, M., Structure of the merozoite surface protein 1 from Plasmodium falciparum. *Sci Adv* **2021**, *7* (23).
207. Gruenberg, J.; Allred, D. R.; Sherman, I. W., Scanning electron microscope-analysis of the protrusions (knobs) present on the surface of Plasmodium falciparum-infected erythrocytes. *J Cell Biol* **1983**, *97* (3), 795-802.
208. Kirchgatter, K.; Del Portillo, H. A., Clinical and molecular aspects of severe malaria. *An Acad Bras Cienc* **2005**, *77* (3), 455-75.
209. Warncke, J. D.; Beck, H. P., Host Cytoskeleton Remodeling throughout the Blood Stages of Plasmodium falciparum. *Microbiol Mol Biol Rev* **2019**, *83* (4).
210. Boddey, J. A.; Cowman, A. F., Plasmodium nesting: remaking the erythrocyte from the inside out. *Annu Rev Microbiol* **2013**, *67*, 243-69.
211. David, P. H.; Hommel, M.; Miller, L. H.; Udeinya, I. J.; Oligino, L. D., Parasite sequestration in Plasmodium falciparum malaria: spleen and antibody modulation of cytoadherence of infected erythrocytes. *Proc Natl Acad Sci U S A* **1983**, *80* (16), 5075-9.
212. Berendt, A. R.; Ferguson, D. J.; Newbold, C. I., Sequestration in Plasmodium falciparum malaria: sticky cells and sticky problems. *Parasitol Today* **1990**, *6* (8), 247-54.
213. Lee, W. C.; Russell, B.; Renia, L., Sticking for a Cause: The Falciparum Malaria Parasites Cytoadherence Paradigm. *Front Immunol* **2019**, *10*, 1444.

214. Smith, J. D.; Rowe, J. A.; Higgins, M. K.; Lavstsen, T., Malaria's deadly grip: cytoadhesion of Plasmodium falciparum-infected erythrocytes. *Cell Microbiol* **2013**, *15* (12), 1976-83.
215. Frohlich, B.; Jager, J.; Lansche, C.; Sanchez, C. P.; Cyrklaff, M.; Buchholz, B.; Soubeiga, S. T.; Simpoire, J.; Ito, H.; Schwarz, U. S.; Lanzer, M.; Tanaka, M., Hemoglobin S and C affect biomechanical membrane properties of P. falciparum-infected erythrocytes. *Commun Biol* **2019**, *2*, 311.
216. Zhang, Y.; Huang, C.; Kim, S.; Golkaram, M.; Dixon, M. W.; Tilley, L.; Li, J.; Zhang, S.; Suresh, S., Multiple stiffening effects of nanoscale knobs on human red blood cells infected with Plasmodium falciparum malaria parasite. *Proc Natl Acad Sci U S A* **2015**, *112* (19), 6068-73.
217. Horrocks, P.; Pinches, R. A.; Chakravorty, S. J.; Papakrivov, J.; Christodoulou, Z.; Kyes, S. A.; Urban, B. C.; Ferguson, D. J.; Newbold, C. I., PfEMP1 expression is reduced on the surface of knobless Plasmodium falciparum infected erythrocytes. *J Cell Sci* **2005**, *118* (Pt 11), 2507-18.
218. Cyrklaff, M.; Sanchez, C. P.; Kilian, N.; Bisseye, C.; Simpoire, J.; Frischknecht, F.; Lanzer, M., Hemoglobins S and C interfere with actin remodeling in Plasmodium falciparum-infected erythrocytes. *Science* **2011**, *334* (6060), 1283-6.
219. Cyrklaff, M.; Srismith, S.; Nyboer, B.; Burda, K.; Hoffmann, A.; Lasitschka, F.; Adjalley, S.; Bisseye, C.; Simpoire, J.; Mueller, A. K.; Sanchez, C. P.; Frischknecht, F.; Lanzer, M., Oxidative insult can induce malaria-protective trait of sickle and fetal erythrocytes. *Nat Commun* **2016**, *7*, 13401.
220. Looker, O.; Blanch, A. J.; Liu, B.; Nunez-Iglesias, J.; McMillan, P. J.; Tilley, L.; Dixon, M. W. A., The knob protein KAHRP assembles into a ring-shaped structure that underpins virulence complex assembly. *PLoS Pathog* **2019**, *15* (5), e1007761.
221. Crabb, B. S.; Cooke, B. M.; Reeder, J. C.; Waller, R. F.; Caruana, S. R.; Davern, K. M.; Wickham, M. E.; Brown, G. V.; Coppel, R. L.; Cowman, A. F., Targeted gene disruption shows that knobs enable malaria-infected red cells to cytoadhere under physiological shear stress. *Cell* **1997**, *89* (2), 287-96.
222. Cutts, E. E.; Laasch, N.; Reiter, D. M.; Trenker, R.; Slater, L. M.; Stansfeld, P. J.; Vakonakis, I., Structural analysis of P. falciparum KAHRP and PfEMP1 complexes with host erythrocyte spectrin suggests a model for cytoadherent knob protrusions. *PLoS Pathog* **2017**, *13* (8), e1006552.

223. Kilejian, A.; Rashid, M. A.; Aikawa, M.; Aji, T.; Yang, Y. F., Selective association of a fragment of the knob protein with spectrin, actin and the red cell membrane. *Mol Biochem Parasitol* **1991**, *44* (2), 175-81.
224. Oh, S. S.; Voigt, S.; Fisher, D.; Yi, S. J.; LeRoy, P. J.; Derick, L. H.; Liu, S.; Chishti, A. H., Plasmodium falciparum erythrocyte membrane protein 1 is anchored to the actin-spectrin junction and knob-associated histidine-rich protein in the erythrocyte skeleton. *Mol Biochem Parasitol* **2000**, *108* (2), 237-47.
225. Pei, X.; An, X.; Guo, X.; Tarnawski, M.; Coppel, R.; Mohandas, N., Structural and functional studies of interaction between Plasmodium falciparum knob-associated histidine-rich protein (KAHRP) and erythrocyte spectrin. *J Biol Chem* **2005**, *280* (35), 31166-71.
226. Waller, K. L.; Cooke, B. M.; Nunomura, W.; Mohandas, N.; Coppel, R. L., Mapping the binding domains involved in the interaction between the Plasmodium falciparum knob-associated histidine-rich protein (KAHRP) and the cytoadherence ligand P. falciparum erythrocyte membrane protein 1 (PfEMP1). *J Biol Chem* **1999**, *274* (34), 23808-13.
227. Weng, H.; Guo, X.; Papoin, J.; Wang, J.; Coppel, R.; Mohandas, N.; An, X., Interaction of Plasmodium falciparum knob-associated histidine-rich protein (KAHRP) with erythrocyte ankyrin R is required for its attachment to the erythrocyte membrane. *Biochim Biophys Acta* **2014**, *1838* (1 Pt B), 185-92.
228. Oh, S. S.; Chishti, A. H.; Palek, J.; Liu, S. C., Erythrocyte membrane alterations in Plasmodium falciparum malaria sequestration. *Curr Opin Hematol* **1997**, *4* (2), 148-54.
229. Hell, S. W.; Wichmann, J., Breaking the diffraction resolution limit by stimulated emission: stimulated-emission-depletion fluorescence microscopy. *Opt Lett* **1994**, *19* (11), 780-2.
230. Schnitzbauer, J.; Wang, Y.; Zhao, S.; Bakalar, M.; Nuwal, T.; Chen, B.; Huang, B., Correlation analysis framework for localization-based superresolution microscopy. *Proc Natl Acad Sci U S A* **2018**, *115* (13), 3219-3224.
231. Pan, L.; Yan, R.; Li, W.; Xu, K., Super-Resolution Microscopy Reveals the Native Ultrastructure of the Erythrocyte Cytoskeleton. *Cell Rep* **2018**, *22* (5), 1151-1158.
232. Sanchez, C. P.; Patra, P.; Chang, S. S.; Karathanasis, C.; Hanebutte, L.; Kilian, N.; Cyrklaff, M.; Heilemann, M.; Schwarz, U. S.; Kudryashev, M.; Lanzer, M., KAHRP dynamically relocates to remodeled actin junctions and associates with knob spirals in Plasmodium falciparum-infected erythrocytes. *Mol Microbiol* **2022**, *117* (2), 274-292.

233. Helms, G.; Dasanna, A. K.; Schwarz, U. S.; Lanzer, M., Modeling cytoadhesion of Plasmodium falciparum-infected erythrocytes and leukocytes-common principles and distinctive features. *FEBS Lett* **2016**, *590* (13), 1955-71.
234. Trager, W.; Jensen, J. B., Human malaria parasites in continuous culture. *Science* **1976**, *193* (4254), 673-5.
235. Staalsoe, T.; Giha, H. A.; Dodoo, D.; Theander, T. G.; Hviid, L., Detection of antibodies to variant antigens on Plasmodium falciparum-infected erythrocytes by flow cytometry. *Cytometry* **1999**, *35* (4), 329-36.
236. Boyle, M. J.; Wilson, D. W.; Richards, J. S.; Riglar, D. T.; Tetteh, K. K.; Conway, D. J.; Ralph, S. A.; Baum, J.; Beeson, J. G., Isolation of viable Plasmodium falciparum merozoites to define erythrocyte invasion events and advance vaccine and drug development. *Proc Natl Acad Sci U S A* **2010**, *107* (32), 14378-83.
237. Lambros, C.; Vanderberg, J. P., Synchronization of Plasmodium falciparum erythrocytic stages in culture. *J Parasitol* **1979**, *65* (3), 418-20.
238. Castano-Diez, D.; Kudryashev, M.; Arbeit, M.; Stahlberg, H., Dynamo: a flexible, user-friendly development tool for subtomogram averaging of cryo-EM data in high-performance computing environments. *J Struct Biol* **2012**, *178* (2), 139-51.
239. Sanchez, C. P.; Karathanasis, C.; Sanchez, R.; Cyrklaff, M.; Jager, J.; Buchholz, B.; Schwarz, U. S.; Heilemann, M.; Lanzer, M., Single-molecule imaging and quantification of the immune-variant adhesin VAR2CSA on knobs of Plasmodium falciparum-infected erythrocytes. *Commun Biol* **2019**, *2*, 172.
240. Alampalli, S. V.; Grover, M.; Chandran, S.; Tatu, U.; Acharya, P., Proteome and Structural Organization of the Knob Complex on the Surface of the Plasmodium Infected Red Blood Cell. *Proteomics Clin Appl* **2018**, *12* (4), e1600177.
241. Cobbold, S. A.; Santos, J. M.; Ochoa, A.; Perlman, D. H.; Llinas, M., Proteome-wide analysis reveals widespread lysine acetylation of major protein complexes in the malaria parasite. *Sci Rep* **2016**, *6*, 19722.
242. Pease, B. N.; Huttlin, E. L.; Jedrychowski, M. P.; Talevich, E.; Harmon, J.; Dillman, T.; Kannan, N.; Doerig, C.; Chakrabarti, R.; Gygi, S. P.; Chakrabarti, D., Global analysis of protein expression and phosphorylation of three stages of Plasmodium falciparum intraerythrocytic development. *J Proteome Res* **2013**, *12* (9), 4028-45.
243. Li, N.; Chen, S.; Xu, K.; He, M. T.; Dong, M. Q.; Zhang, Q. C.; Gao, N., Structural basis of membrane skeleton organization in red blood cells. *Cell* **2023**, *186* (9), 1912-1929 e18.

244. Nans, A.; Mohandas, N.; Stokes, D. L., Native ultrastructure of the red cell cytoskeleton by cryo-electron tomography. *Biophys J* **2011**, *101* (10), 2341-50.
245. Wu, S.; Armache, J. P.; Cheng, Y., Single-particle cryo-EM data acquisition by using direct electron detection camera. *Microscopy (Oxf)* **2016**, *65* (1), 35-41.
246. Rice, G.; Wagner, T.; Stabrin, M.; Raunser, S., TomoTwin: Generalized 3D Localization of Macromolecules in Cryo-electron Tomograms with Structural Data Mining. bioRxiv: 2022.
247. Zeng, X.; Kahng, A.; Xue, L.; Mahamid, J.; Chang, Y. W.; Xu, M., High-throughput cryo-ET structural pattern mining by unsupervised deep iterative subtomogram clustering. *Proc Natl Acad Sci U S A* **2023**, *120* (15), e2213149120.
248. Harp, K. O.; Botchway, F.; Dei-Adomakoh, Y.; Wilson, M. D.; Hood, J. L.; Adjei, A. A.; Stiles, J. K.; Driss, A., Hemoglobin Genotypes Modulate Inflammatory Response to Plasmodium Infection. *Front Immunol* **2020**, *11*, 593546.
249. Uyoga, S.; Macharia, A. W.; Ndila, C. M.; Nyutu, G.; Shebe, M.; Awuondo, K. O.; Mturi, N.; Peshu, N.; Tsofa, B.; Scott, J. A. G.; Maitland, K.; Williams, T. N., The indirect health effects of malaria estimated from health advantages of the sickle cell trait. *Nat Commun* **2019**, *10* (1), 856.
250. Archer, N. M.; Petersen, N.; Clark, M. A.; Buckee, C. O.; Childs, L. M.; Duraisingh, M. T., Resistance to Plasmodium falciparum in sickle cell trait erythrocytes is driven by oxygen-dependent growth inhibition. *Proc Natl Acad Sci U S A* **2018**, *115* (28), 7350-7355.
251. Wadman, M., Sickle-cell mystery solved. *Nature* **2011**.



Publiziert unter der Creative Commons-Lizenz Namensnennung (CC BY) 4.0 International.
Published under a Creative Commons Attribution (CC BY) 4.0 International License.
<https://creativecommons.org/licenses/by/4.0/>